Inferring brain network dynamics of MEG and EEG in healthy aging and Alzheimer's disease

SungJun Cho

Hertford College

University of Oxford

A thesis submitted for the degree of

Master of Science by Research

Trinity 2023

Acknowledgements

Embarking upon an academic journey, which whisked me across the continent and nestled me into the welcoming environments of the University of Oxford and Hertford College, has been nothing short of a splendid adventure. Enveloped by rich traditions and surrounded by esteemed intellects, the past year has presented the generous sharing of knowledge and camaraderie that the wonderful individuals of Oxford unreservedly offered. My time here has been not only cordial but also remarkably memorable, all culminating in the completion of this thesis.

Heartfelt gratitude goes to my supervisors, Mark Woolrich, Mats van Es, and Chetan Gohil, whose generous support and advice were pivotal throughout my studies. Without their help none of this would have been possible. Mark, as my mentor, consistently propelled me towards clear, precise, and rigorous scientific practices, fostering my growth as a scientist. Mats provided invaluable guidance, helping me maintain a broad perspective and consider the overarching narrative of my research. Chet fortified the mathematical and technical aspects of my project and was always available when I had questions and curiosities. I envision a future of continued collaboration and enduring friendships with them all.

I sincerely appreciate the Analysis group and my colleagues at OHBA, with particular mentions to Andrew, Rukuang, Evan, and Hongyu, for their constructive discussions which enriched my research and data analysis. I am especially indebted to Andrew for his support and invaluable guidance in navigating through challenges. To my friends, from Chicago, Seoul, and Oxford, your encouragement and steadfast support have been a beacon that made the English winter more than just bearable.

With immense love, I express my deepest thanks to my parents, Sungyun and Joo Ryung; my sister, Yunyi; and my grandparents, Hae Ryong, Sun Nam, Nam Seung, and Young Ja. Your unwavering love and belief have been my anchors, infusing my life and the science I pursue with profound meaning.

Reflecting on my Oxford experience, having sauntered through the very halls that once nurtured the greatest minds of human history, has been utterly enchanting. It is with my sincere hope that my work, even in its smallest facets, contributes a fragment of knowledge to humankind and perhaps, plays a modest role in alleviating the sufferings of those afflicted by the maladies explored in this research.

Abstract

Alzheimer's disease (AD) has long been encumbered by a lack of clinically effective biomarkers, which has impeded its early-stage detection and relegated diagnostic practices to symptom-based observations. Amidst the ongoing quest to discover novel biomarkers with enhanced clinical utility, this thesis aims to elucidate the prospect of static and dynamic changes in brain network features, derived from electroencephalography (EEG) and magnetoencephalography (MEG), to explicate the earliest changes in the brain caused by AD.

The first component of the thesis contrasts MEG and EEG in capturing age-related effects within the healthy aging datasets and validates the methodologies initially designed for MEG for their application to EEG. We demonstrate that while both modalities reveal analogous age effects in static power spectra and narrow-band power, MEG exhibits higher sensitivity to age effects in various brain network features within source space. The adopted analysis techniques successfully replicated previously documented healthy aging effects, substantiating their credibility in inferring transient resting-state network (RSN) dynamics from M/EEG data.

Leveraging the findings above, the second component of the thesis focuses on identifying modality-specific biomarkers for mild cognitive impairment (MCI) and early-stage AD from resting-state M/EEG. The reproducibility of known biomarkers — evident in static RSN features and the posterior default mode network — is confirmed in our dataset. Furthermore, we show that the dynamic effects of MCI and early-stage AD in the wide-band power and temporal dynamics of RSNs can be recognized as potential AD biomarkers. These results are among the first to demonstrate the statistically significant effects of prodromal AD in resting-state M/EEG.

Together, our findings provide a concrete case that M/EEG-derived static and dynamic RSN features can potentially be reliable and clinically meaningful biomarkers. This research propels the field towards refining early detection mechanisms for AD, laying a foundation for ensuing research to build upon, and steering future diagnostic practices towards enhanced efficacy.

Contents

List of Figures

List of Tables

List of Abbreviations

AD . . . . . Alzheimer's Disease

AEC . . . . . Amplitude envelope correlation

A-T-N . . . . . Amyloid-tau-neurodegeneration

BEM . . . . . Boundary Element Model

BET . . . . . Brain Extraction Tool

BOLD . . . . . Blood oxygenation level dependent

Cam-CAN . . Cambridge Centre for Ageing and Neuroscience

COPE . . . . . Contrast of parameter estimates

CSF . . . . . Cerebral spinal fluid

DBS . . . . . Deep brain stimulation

DMN . . . . . Default mode network

DyNeMo . . . Dynamic Network Modes

DSM-5 . . . . Diagnostic and Statistical Manual of Mental Disorders, Fifth Edition

ECG . . . . . Electrocardiogram

EEG . . . . . Electroencephalography

FC . . . . . Functional connectivity

G-ESD . . . . Generalized-extreme studentized deviate

GLM . . . . . General Linear Model

GMM . . . . . Gaussian Mixture Model

GPU . . . . . Graphics processing unit

HMM . . . . . Hidden Markov Model

ICA . . . . . Independent Component Analysis

ICP . . . . . Iterative closest point

IIR . . . . . Infinite impulse response

KL . . . . . Kullback-Leibler

LEMON . . . Leipzing Study for Mind-Body-Emotion Interactions

LFP . . . . . Local field potential

LL . . . . . Log-likelihood

L/RPA . . . . Left / right pre-auricular points

LSTM . . . . . Long Short-Term Memory

MCI . . . . . Mild cognitive impairment

MEG . . . . . Magnetoencephalography

MPRAGE . . Magnetization-Prepared RApid Gradient Echos

MP2RAGE . . Magnetization-Prepared 2 RApid Acquisition Gradient Echos

MRI . . . . . Magnetic resonance imaging

NfL . . . . . Neurofilament light chain

NTAD . . . . . New Therapeutics in Alzheimer's Disease

V/HEOG . . . Vertical / horizontal electrooculogram

OHBA . . . . . Oxford Centre for Human Brain Activity

OSL . . . . . OHBA Software Library

PCA . . . . . Principal component analysis

PET . . . . . Positron emission tomography

PLI . . . . . Phase lag index

PSD . . . . . Power spectral density

PTSD . . . . . Post-traumatic stress disorder

RNN . . . . . Recurrent neural network

RSN . . . . . Resting state network

SWC . . . . . Sliding window correlation

TDE . . . . . Time-delay embedded / embedding

VB . . . . . Variational Bayesian

1 Introduction

Contents

1.1 Motivation

1.1.1 Challenges in Modern Neuropsychiatry

In the absence of a definitive nosology and etiology, psychiatry is arguably the most unstructured discipline among the medical sciences. Many of the mental disorders demonstrate transdiagnostic characteristics and a high degree of comorbidity [1–3], further complicated by the lack of well-articulated pathophysiological mechanisms [4] and an inherent heterogeneity in disease manifestations [5]. This predicament can be ascribed, in part, to the current diagnostic approach for neuropsychiatric[1]

[1]The ongoing discourse suggests that the demarcation between neurological diseases and psychiatric disorders is contingent upon whether their underpinnings can be sufficiently elucidated using a biological framework. In alignment with the materialistic movement advocating for

disorders, which is largely grounded in subjective symptomatology [5, 6]. For many years, the process of diagnosing these disorders relied heavily on self-reported symptoms, with practitioners categorizing patients based on symptom descriptions outlined in standard diagnostic resources such as the Diagnostic and Statistical Manual of Mental Disorders (DSM-5) [2, 7].

Over the last decade, there has been a marked shift in the diagnostic paradigm and treatment procedures within the field of psychiatry. This evolution emphasizes the underlying pathophysiological mechanisms that drive mental disorders, mirroring the larger medical community's departure from a symptom-based approach to a more objective, biology-oriented framework. Such endeavor cultivated a new field called biological psychiatry, dedicated to unraveling the biological dysfunctions of the nervous system that result in cognitive abnormalities. The primary aim of this movement has been to find pathogenic and pathophysiological mechanisms that distinctly categorize patients into diagnostic cohorts, subsequently guiding them toward tailored therapeutic strategies [5]. Computational neuropsychiatry has bolstered this effort by employing data-driven methodologies to classify subtypes of disorders and constructing explanatory models that link neuropsychiatric dysfunctions to their causative structures [3, 8]. These perspectives have reframed mental disorders as conditions rooted in biological anomalies that induce computational malfunctions in the neural information processing system.

In line with this effort, biomarkers have emerged as an invaluable tool for accurate diagnosis, guidance on treatment strategies, and assessment of therapeutic efficacy [9, 10]. Despite the burgeoning research in biomarker identification, the translation of these biomarkers into clinical practice has been hampered by their low clinical utility [1, 6, 10]. The literature suggests four principal reasons for this discrepancy [4–6]:

- **Absence of a gold standard definition.** Specific disorders lack a unique, universally accepted definition, primarily due to their classification based on symptoms rather than pathological mechanisms.

biological psychiatry, this paper will adopt the unified term **neuropsychiatry**, thereby obviating any subjective boundaries that segregate anomalies of the nervous system.

- **Insufficient statistical power.** Notwithstanding a plethora of statistically significant findings, the classification of patients into pertinent diagnostic cohorts remains minimally differentiating, partly due to small sample sizes in studies leading to underpowered statistical analyses.

- **Uncertainty in large effect size.** Large effect sizes are generally derived from (extreme) comparisons of patients and healthy controls, with identified effects only partially replicated due to subject variability and variability in using different methods, scanners, and experiment paradigms. This introduces uncertainty regarding the stability of the effects.

- **Heterogeneity in disease onset and development.** Given the diversity in symptom combinations and phenotypes, as well as changes in biological indicators at different stages of disease progression, disorders such as post-traumatic stress disorder (PTSD) [11, 12] and Alzheimer's disease (AD) [13, 14] exhibit a wide range of symptom permutations and multifactorial developments.

Hence, the statistical significance of a biomarker does not automatically render it clinically meaningful. The reduced power and reproducibility of many biomarkers impede the identification of not only symptomatic diseases but also prodromal and preclinical stages of these disorders.

Modern neuropsychiatry thus calls for biomarkers capable of discerning clinically meaningful differences among relevant clinical populations. Achieving this would necessitate conducting longitudinal studies, employing standardized measures and protocols reproducible across multiple studies, and using a data-driven approach to minimize systematic bias and preclude transdiagnostic tendencies [2, 4–6]. The ultimate goal would be to fulfill a mechanism-based nosology that reflects the true etiology, which can be used to categorize subclasses of diseases and relate them to predict accurate treatment responses [15].

1.1.2 Objectives

AD is a notable example where the absence of clinically meaningful biomarkers hinders early-stage detection at the individual subject level. Current diagnosis of AD relies heavily on detecting cognitive decline, at which point the disease may have already caused irreversible cognitive decline or brain damage. Recent advances in biomarker studies based on the amyloid-tau-neurodegeneration (A-T-N) framework have related AD to neuroimaging, cerebral spinal fluid (CSF), neurofilament light chain (NfL), blood plasma proteins, and genetic risk factors [16, 17]. However, these biomarkers have yet to exhibit high clinical efficacy, relegating their use to auxiliary roles in symptom-based diagnosis [18, 19]. Thus, there is an ongoing quest for finding more efficacious biomarkers with improved clinical utility.

One promising avenue for such a biomarker lies in the investigation of functional resting state networks (RSNs) using neuroimaging data. Electroencephalography (EEG) and magnetoencephalography (MEG) have shown a particular promise in this regard. The objective of this report, therefore, is to elucidate **the potential of M/EEG-derived static and dynamic changes in brain network features** to provide insights into the prodromal phase of AD. By doing so, it aims to lay a groundwork for evaluating M/EEG biomarkers for clinical utility and for further probing their capability in addressing the aforementioned limitations prevalent in biomarker research.

In the following sections, we will provide a brief overview of each component of our objective: 1) electrophysiological modalities, 2) RSNs, and 3) static and dynamic changes in functional brain networks. We begin by outlining the advantages of M/EEG, their similarities and differences, and their complementary potential. We then delineate the concept of RSNs and their functional significance to explicate why they may serve as effective biomarkers. Lastly, we discuss the quantification of static and dynamic characteristics of RSNs, the importance of incorporating dynamic changes to static observations, and the foundations of the dynamic techniques we will employ. We will conclude by outlining the structure of this thesis.

1.2 Complementary Potentials and Benefits of EEG and MEG

Prevailing neuroimaging modalities such as magnetic resonance imaging (MRI) and positron emission tomography (PET) provide indirect measurements of neuronal activities by quantifying metabolic reactions across diverse cell types. MRI is commonly used to assess structural atrophies and functional changes marked by hemodynamic brain activities [20], and PET estimates functional lesions by using radiotracers or ligands that bind to proteins and synapses [17]. Although their emphasis on metabolic changes yields exquisite spatial resolution, their temporal resolution is in turn often compromised.

To counterbalance these limitations, EEG and MEG offer a viable alternative, leveraging their high temporal resolution and direct measurement of electrophysiological signals to illuminate synaptic integrity and neuronal communications [20, 21]. The robustness of M/EEG is primarily attributed to their sensitivity to a common source type – synchronous post-synaptic currents in aligned pyramidal cells[2] [21]. The columnar orientation of these neurons, mainly situated in the cortex, engenders a net dipole current that contributes significantly to the total neural oscillations detected by these modalities[3].

However, it is crucial to acknowledge the inherent differences between EEG and MEG, many of which are derived from their unique measurement properties and sensitivity characteristics. MEG quantifies changes in magnetic flux outside the head, while EEG measures electric potential differences at the scalp. This extracranial recording intrinsically introduces noise and leads to a diminished spatial resolution [21]. Furthermore, the magnetic and electric fields, being orthogonal to each other, dictate that MEG sensors detect tangential components of the current sources while EEG sensors capture both tangential and radial components. The ability of MEG to

[2]Although other neurons like stellate cells contribute to the overall currents, the layer V and II/III pyramidal cells are known to be the major contributors to M/EEG signals [22]. The burst discharge by pyramidal cells is estimated to be detectable when there is a synchronous activation of approximately 10,000-50,000 cells [22].

[3]This physiological conformation of the source results in M/EEG being more sensitive to currents located in the cortical regions at a shorter distance than other subcortical areas.

detect only tangential dipoles suggests its comparatively lower sensitivity to depth relative to EEG. In addition, MEG is also known to be less sensitive to subcortical source signals, as evidenced by the signal-to-noise ratio (SNR) of MEG declining at a faster pace than that of EEG as the depth of the source increases [23–25].

A pivotal difference is also observed in their sensitivity characteristics: MEG mainly detect primary currents, whereas EEG display higher sensitivity to secondary currents[4] [26]. Consequently, EEG is subjected to a volume conduction problem, in which the conductivity of varied tissue types needs to be considered for source reconstruction [24]. Therefore, accurate head orientation and conductivity measures become essential for EEG source reconstruction, adding intricacy to the forward-inverse problem and further compromising the SNR [21].

The contrasting spatial sensitivity characteristics of MEG and EEG, however, denote the potential presence of distinct yet complementary information within each modality [25]. Specifically, complementary properties of M/EEG data have already been demonstrated in multiple studies [27–29], and solving the inverse problem based on combined M/EEG has shown a considerable potential [30, 31]. To this extent, understanding the differential representation of neural information in EEG and MEG and exploring their complementary roles are of paramount importance. Integrating these modalities with other neuroimaging techniques (e.g., fMRI [25, 32]) may further enhance currently available spatiotemporal resolution, promoting a comprehensive multimodal approach in neuroimaging.

1.3 Resting State Networks and their Functional Significance

1.3.1 A Brief History of RSNs

The notion that the resting brain is characterized by states of structured and synchronous activity as opposed to stochastic activities has now achieved substantial

[4]Primary currents are the electrical currents that flow through the pyramidal neurons, mainly across their apical dendrites and the soma. On the other hand, secondary currents, or volume currents, are the currents that are generated when the primary currents propagate through the extracellular space, skull, and scalp.

academic consensus. The existence of RSNs within the brain was first discovered in the late 20th century, when Biswal et al. (1995) first recognized the correlated patterns of fMRI blood-oxygen-level-dependent (BOLD) signals during the resting phases of a finger-tapping task, denoting these patterns as an indication of functional connectivity [33]. Building upon this work, Shulman et al. (1997) used PET imaging to demonstrate that specific brain regions display higher activation levels during the resting state than during visual processing or cognitive language tasks [34]. These landmark studies catalyzed our understanding of the resting brain, underscoring the conception that the brain, even during periods of rest, partakes in continuous neuronal communication, typified by distinctive spatiotemporal patterns.

Successive examinations of RSNs have further elucidated their attributes and properties. PET imaging techniques revealed that there exists a fundamental baseline state, known as the default mode network (DMN), that is particularly prevalent in the resting brain [35]. This particular state occurred when individuals direct their attention towards internal cognitive processes, such as self-awareness and memory retrieval [36, 37]. Moreover, it became evident that resting-state activity is not exclusive to a singular network. Independent component analysis (ICA) of fMRI data uncovered roughly 8-10 RSNs that consistently emerge across multiple imaging sessions and subjects, demonstrating independent synchronizations of coactive brain regions [38–40][5]. It was thereby confirmed that the human brain incorporates a broad spectrum of functional networks during rest, indicative of baseline activity that can be consistently observed across different subjects.

However, the description of RSNs as representing baseline activities does not imply their lack of functional relevance or significance. Given the capacity of the resting brain to organize into networks of functional activity, RSNs have shown to represent both sensorimotor functions [32, 41, 42] and cognitive processes such as attention and executive control [43–46]. Notably, these RSNs embody the heterogenous patterns of coordinated brain function detected during a range of cognitive tasks in fMRI [47]. Studies on various neuropsychiatric disorders have also

[5]Spatial ICA was implemented in [38, 39], and temporal ICA was employed in [40].

consistently illustrated that RSNs have functional relevance to numerous conditions, including AD [48, 49], major depressive disorder [50, 51], and schizophrenia [52, 53], across multiple imaging modalities[6].

1.3.2 Electrophysiological Contributions to RSNs

The initial identification of RSNs in fMRI and PET has been independently confirmed through EEG and MEG. Notably, Brookes et al. (2011) performed a temporal ICA on the amplitude envelopes of MEG oscillations, without any prior assumptions about the spatial patterns of the networks. The resultant RSNs resembled those previous identified by fMRI [54], underscoring the existence of these networks across different imaging modalities.

Employing M/EEG for RSN analysis offers several advantages over other neuroimaging techniques. First, since the data comprise electrophysiological signals, it is feasible to explore distinct oscillatory frequencies linked to each network. Empirical evidence suggests that various neural processes can be discretized into unique states of global synchronous fluctuations, each associated with a specific frequency range [54–56]. This stands in contrast to BOLD signals, which are defined by relatively lower temporal frequencies.

Secondly, the superior temporal resolution of M/EEG data enables a detailed examination of the dynamic behaviours of these networks, including the activation and deactivation sequences of RSNs. Previous studies demonstrate that M/EEG-derived RSNs activate on a considerably more rapid timescale (approximately 100-200 ms) than RSNs detected from fMRI [57, 58]. This rapid activation pattern of RSNs could successfully explain brain network dynamics underlying various tasks and resting-state cognitive processes [59, 60].

Furthermore, RSNs themselves offer pragmatic advantages. As the data collection occurs during the rest, the experimental constraints and parameters are minimal. This reduction in turn eliminates the need for additional assumptions in interpreting results and simplifies the comparison of observations across modalities

[6]For the use of MEG and EEG, refer to [49] and [51], respectively. For the use of fMRI, see [48, 50, 52]. [53] utilized both fMRI and MEG.

and studies. RSNs also allow for a more diverse participant pool. For instance, a participant with a neurological condition affecting one's mobility or task performance would merely need to stay still during the data collection. This relaxed requirement hints at the potential of RSNs as biomarkers with considerable clinical utility, as they are amenable to testing on virtually any individual, irrespective of mental or physical limitations.

Therefore, the functional significance of RSNs, corroborated thus far, coupled with added benefits provided by M/EEG, underscores the potential of electrophysiological brain network features as powerful tools to discern differences in latent neural information pertaining to healthy aging and neurodegeneration generated by AD.

1.4 Quantification of Static and Dynamic Changes in Functional RSNs

1.4.1 Limitation of Static Observations and Necessity of Dynamic Methodology

Neural oscillations, distinguished by their rhythmic spectral patterns, have traditionally been studied by analyzing electrophysiological recordings that are averaged over time, trials, and/or space. This approach has formed the foundation of our understanding of neural activity in the human brain and the role canonical frequency bands play in interpreting these oscillations. Nevertheless, this conventional view, which tends to reveal oscillations as having sustained increase in power, has been contested by recent research. Contemporary studies suggest that *sustained* increases in oscillatory power may simply be a result of averaging over times, trials, and/or space when there is temporal variability in the timing of much shorter lived transient spectral events [61–65]. Therefore, it is posited that a more holistic evaluation involving the temporal, spatial, and spectral domains is needed to elucidate the functional relevance of these underlying transient spectral events in health and disease [66]. For example, acknowledging, and avoiding, the limitations of crude temporal averaging (i.e., static analysis) are vital for investigating how information travels across brain regions and multiplexes across frequencies at specific time points.

Dynamic analyses of transient events have gained prominence in two research areas that emphasize the limitations of static observations: RSNs and neural oscillatory bursts. As discussed earlier, M/EEG has heralded new opportunities in exploring the temporal dynamics of RSNs. Electrophysiological data has revealed the existence of rapid and transient brain network states, and several studies have linked the dynamics of RSNs to human cognition and disease. For instance, replay bursts in humans have been found to align with the activation of the default mode and parietal alpha networks [67], and this coupling between replay and DMN was weakened in schizophrenia [68]. Furthermore, functional network abnormalities in AD have also been associated with short-timescale changes in network activity, where DMN and dorsal attention network activated in shorter durations (150 ms) compared to healthy controls [49].

In burst studies, the neural oscillations have been analyzed within specific frequency bands and even specific brain regions, using various methods such as animal local field potentials (LFPs) or invasive and noninvasive human recordings. These studies focused on bursts, which are high-amplitude neural events that momentarily surface in the neural oscillations. There is a growing consensus that these transient neural bursts may be a crucial temporal signature guiding cognition and behavior. Across species, single-trial level oscillatory bursts have been consistently observed and hypothesized to underpin sensory, motor, and cognitive systems[7], including motor impairments in Parkinson's disease (deep brain stimulation (DBS) electrodes) [69], the influence of anxiety on reward-dependent motor learning (EEG) [70], perception and attention (LFP, MEG) [71], and working memory (LFP) [72].

All of these studies provide compelling evidence that dynamic observations offer valuable insights into the variations in cognitive states of both healthy individuals and those with disorders, a perspective unattainable through static analyses. As the following chapters of this thesis will demonstrate, dynamic methodologies can enrich

[7]See [63] for more information about the papers studying the role of bursts in sensorimotor processing, cognition, and behaviors.

the results drawn from the static methods, sometimes adding novel information that unveils only with sufficient temporal granularity.

1.4.2 Dynamic Modelling of Electrophysiological Data

Having established the significance of a dynamic methodology, this paper now proceeds to review two dynamic models: the Hidden Markov Model (HMM) and Dynamic Network Modes (DyNeMo). These models provide a framework to describe the spatiotemporal distribution of power and functional connectivity within RSNs. As these models form the core of our analysis, we shall succinctly discuss their foundations. It should be noted, however, that the primary focus of this paper is the application of these dynamic models to electrophysiological data, rather than a comprehensive overview of their mathematical formulations or technical details. Hence, we confine our discussion to the fundamental concepts of these models, particularly how they infer the periods of transient network activations. For further information about their hyperparameters and implementation, readers are referred to Chapters 2 and 3.

Until now, a prominent approach in the field has been the sliding window correlation (SWC) method [73–76]. This methodology infers the dynamic properties of the data by applying the traditional static methods to temporally windowed data segments. However, its necessity to divide the data into short, uniform segments and pre-specify the temporal resolution enforces artificial time scales on the networks [77]. Our interpretation of the dynamics, therefore, is dependent on the selection of a time-window length. Although this window must be sufficiently long for robust estimation of a large-scale functional connectivity, long windows may underestimate transient changes, while short windows introduce more noises [77, 78]. Evaluation of MEG functional connectivity additionally revealed that fixed sliding window approaches often detect modulations of connectivity only if the underlying dynamics is slow or moderate [79].

Temporal ICA [40] offers another approach, identifying components from a dataset based on their temporal independence. This assumption of temporal

independence indicates that the method primarily considers how signals change over time while ignoring their spatial features, leading to a suboptimal performance for cases in which multiple spatially distinct networks interact at the same (or other) moment. The lack of probabilistic interpretation and the temporal resolution fixed to a sampling rate further limit this method.

To address the constraints of existing methodologies, the HMM and DyNeMo were conceived[8]. These models alleviate the need to predetermine the window length. Instead, they facilitate the probabilistic representation of various RSN occurrences at specific time points, encapsulating rich spectral data including information pertaining to power and phase. This makes them a potent tool for characterizing spectrally defined networks in electrophysiological data.

HMM

The HMM is a generative model that delineates data as a sequence of recurring functional brain networks called *states*. By design, it is bounded by two mathematical constraints. First, the model is first-order Markovian such that the prediction of a current state is exclusively contingent upon its immediate predecessor. Secondly, the states are mutually exclusive, meaning that only one state can be active at each time point. The architecture of the HMM consists of two components: the hidden state (i.e., latent variables) and an observation model (i.e., observed variables). The former is governed by a transition probability matrix, and the latter describes the data generation process given the hidden states. Hence, the model parameters of the HMM are the hidden state at each time point, the transition probability matrix, and the observation model parameters (e.g., state means and covariances).

These parameters are inferred through the variational Bayesian (VB) inference [80, 81], as no analytical solution is available for them. The variational method reframes the inference process as an optimization task, wherein the objective is to minimize the variational free energy. Moreover, using Bayesian inference enables the model to learn the uncertainty in parameter estimates as probabilistic distributions

[8]The introduction to these models and the tutorials on how to implement them can be found at https://osl-dynamics.readthedocs.io/en/latest/index.html.

of each individual parameter. To scale the learning process to large datasets, the stochastic version of the VB method adapted from [60, 82] is used. Following this methodology, the HMM outputs a time course of posterior probabilities, often referred to as *gamma*, signifying the probability of a state activation at each time step. The extraction of maximum a posteriori probabilities across all states allows for the generation of a Viterbi path, which is the most probable (mutually exclusive) state at every step.

One advantage of the HMM lies in the flexible selection of the observation model, capable of adopting varying forms to suit different data modalities and features. Hence, depending on the chosen observation model, the HMM can take various forms: the amplitude envelope HMM (AE-HMM) [57], multivariate autoregressive HMM[9] (HMM-MAR) [78], and time-delay embedded HMM (TDE-HMM) [60]. As we are interested in examining periods of distinct spectral patterns, the current study utilizes the TDE-HMM, which characterizes spectrally resolved networks based on the power spectral density (PSD) and phase-locking information. In this model, the wide-band source signals are time-delay embedded to encode spectral information. Its observation model is a multivariate normal (Gaussian) distribution. Each state then has their own observed parameters of means and covariances that can capture spectral information at each time point. An example use of this description is to derive PSD from an HMM state's auto-covariance matrix, following the Wiener-Khinchin theorem [59]. The TDE-HMM thus can effectively capture state-wise power spectra and phase locking, i.e., patterns of linear synchronization in oscillatory activity of temporally resolved RSNs [60].

[9]The HMM-MAR is the model that describes each state with distinct auto-regressive (AR) coefficients. Like the auto-covariance, the AR coefficients are mathematically related to the power spectrum of the data. Therefore, this model can also be employed to investigate spectrally specific state dynamics. However, the TDE-HMM is preferred for three main reasons. (1) A previous study has reported that the TDE-HMM performs typically more robustly, especially if the time courses are shorter [59]. (2) The HMM-MAR is known to work optimally with a limited number of brain regions, thereby inadequate for the whole-brain analysis [60]. (3) The HMM-MAR requires large number of parameters, making it more prone to overfitting and consuming more computational resources [60].

DyNeMo

DyNeMo is a generative model that represents data as a time-varying mixture of spatially distributed functional brain networks known as *modes* [58]. This model mitigates two shortcomings of the HMM. First, DyNeMo treats data as a linear combination of modes, which, unlike states in the HMM, can co-exist at a specific time point. This enables the model to account for cases in which multiple modes are equally probable, reducing the potential errors in inferred network metrics that could result from the mutual exclusivity of HMM states as shown in [83].

Secondly, DyNeMo employs a Long Short-Term Memory (LSTM) recurrent neural network (RNN) [84] to capture long-range temporal dependencies among hidden states, moving beyond the confines of the first-order Markovian system. The LSTM serves a role analogous to the transition probability matrix in the HMM, dictating the temporal evolution of mode mixtures. The model parameters of DyNeMo consist of the latent variables (i.e., the logits of LSTMs) and observation model parameters (e.g., mode means and covariances). Like the TDE-HMM, DyNeMo incorporates a time-delay embedding of data to encode spectral characteristics of the source signals into the observed parameters. By adopting the aforementioned methodology, DyNeMo generates a time series of mode mixing coefficients[10], which by convention is typically referred to as the *alpha* parameter, or the alpha time course, signifying the probability of mode activations at each time step.

The parameters of DyNeMo are inferred using VB inference. In contrast to the classical VB approach of the HMM, DyNeMo uses a particular inference method called amortized variational inference, borrowed from the variational auto-encoder [85]. This process involves training an inference network – constructed using an LSTM structure – to predict the posterior distribution of the model parameters (i.e., logits)[11]. The amortized variational inference enables DyNeMo to accommodate

[10]The mode mixing coefficients are subject to a sum-to-one constraint [58], connoting that the aggregate probability of each mode's activation converges to unity.

[11]Expanding upon this, the variational posterior distributions of the model parameters are sampled using the reparameterization trick [85]. This capacity to estimate the variational free energy by Monte Carlo sampling allows parameters to be inferred for virtually any generative model and therefore facilitates the use of a generative model with highly nonlinear transformations

large datasets and has several benefits over the classical VB inference [58]. For instance, the update rules derived by the classical VB inference limits the choice of generative models that can be used and requires the variational posterior to be conjugate distributions. The classical approach also necessitates each variable to have an individual variational distribution and trains the parameters of each variational distribution separately, consuming greater amount of computational memory.

Nonetheless, DyNeMo is not without its limitations [58]. Having a form of neural network, it demands a larger number of hyperparameters for data modeling, making its architecture considerably bigger and thus increasing model training time. Furthermore, the trainable parameters of LSTM layers and an observation model requires appropriate initialization. Hence, the inference of a model becomes more sensitive to how the parameters are initialized and may ultimately lead to higher variability between runs.

On a final note, the similarities between the HMM and DyNeMo should be mentioned. Both the HMM and DyNeMo seek to delineate dynamic changes in the spectral patterns of RSNs, as indicated by the congruence in their objective functions – namely, the minimization of variational free energy. In doing so, they adhere to a single-dynamic approach, predicated on the assumption that both the means and variances of generated data fluctuate in relation to a single, shared time course (i.e., gammas and alphas) [83]. Both models also operate under an unsupervised learning paradigm, where temporal segmentation does not rely on task timings or pre-existing information about network structures.

Simultaneously, these models exhibit shared limitations. Some states or modes can end up fitting to particular artefacts in the data. While this is beneficial for denoising, it does mean that there will be less states/modes to describe the neuronal dynamics. This relates to an additional challenge inherent in their design, which stipulates a fixed number of states or modes. Thus, determining an optimal number of RSNs that might yield meaningful granularity is left to the discretion of the user.

[58]. This cannot be achieved with the classical VB inference employed in the HMM.

In conclusion, when interpreting the inferences drawn from these models and their subsequent post hoc analyses, it is essential to recognize their underlying assumptions and limitations. Nevertheless, despite such constraints, the HMM and DyNeMo are the two state-of-the-art models that can effectively articulate the dynamic behaviors of spectrally resolved whole-brain networks.

1.5 Structure of the Thesis

The primary aim of this study is to determine whether static and dynamic features of functional RSNs can discern AD in its incipient stages and evaluate their potential viability as clinically effective biomarkers for detecting the earliest changes in brain induced by AD. This thesis hypothesizes that significant differences between healthy aging and early-stage AD will be manifested in the electrophysiological signals. The following chapters fulfill the aim and test this hypothesis through a two-step process exploring healthy aging and neurodegeneration.

Chapter 2 sets on the study of healthy aging. An exploratory analysis is conducted on openly available datasets to compare how MEG and EEG represent distinct neural information and perform in capturing age-related effects in the healthy population. In addition, this chapter serves to validate the robustness of the employed methodologies and preliminarily examine brain networks of healthy controls before investigating the clinical dataset.

Chapter 3 delineates the main study of neurodegeneration. It focuses on finding modality-specific biomarkers for AD and gauging their predictive efficacy in identifying patients in their prodromal phases from the New Therapeutics in Alzheimer's Disease Longitudinal Cohort (NTAD) dataset. Here, the analysis pipeline validated in Chapter 2 is applied to compare healthy controls with patients exhibiting amyloid-positive mild cognitive impairments (MCI) or early-stage AD.

Finally, Chapter 4 draws conclusion from the preceding chapters and discusses future directions that the field can pursue.

2

Comparison of EEG and MEG in Detecting the Effects of Healthy Aging

Contents

2.1 Introduction

The impact of aging on resting-state brain activity has been extensively investigated in M/EEG studies. Some of these findings, which were consistently replicated across multiple studies, include: (1) a decline in alpha band activity in the occipital and parietal cortices with age, (2) a global shift[1] in the alpha peak frequency, and (3) an increase in beta band activity in the sensorimotor, frontal, and temporal

[1] In previous literature such as [86], the alpha peak frequency is usually averaged over the data channels before being compared across age groups. Hence, the shift in peak frequency here is described as "global". Further investigations seem necessary to measure the variability in such shift across the brain regions and to answer whether some areas demonstrate a stronger shift than others.

regions with age [86–90][2]. Recent MEG studies examining resting-state functional connectivity have additionally revealed increased variability of delta phase synchrony with age in the DMN [91] while observing no significant age-related differences in the alpha and beta frequency ranges [92]. Existing literature thus demonstrates that resting-state M/EEG can effectively capture and represent age-related effects in the healthy population.

It should be noted, however, that the primary objective of this chapter is to conduct exploratory research that investigates the electrophysiological nature of M/EEG and validate the methodologies employed. The focus is not to delve into the physiological mechanisms underlying healthy aging, but rather to highlight possible disparities between the two modalities in detecting age-related differences.

Distinct data representations of EEG and MEG and their potential complementary attributes thereof have been reported in previous studies in the context of visual processing, auditory perception, and tactile and proprioceptive responses [27, 93, 94]. This project shares a similar goal, seeking to contrast EEG and MEG by examining how age-associated differences are reflected in static and dynamic brain network features. To the best of our knowledge, no previous research has specifically compared these modalities in the context of healthy aging. Considering that aging is an important risk factor for neurodegenerative disorders, it is believed that exploring the dynamics of brain activity in healthy individuals will further offer valuable insights into our study of early-stage AD.

In the following sections, we demonstrate that static and dynamic RSN metrics are good indicators of age effects in both EEG and MEG. The observed age-related effects corroborate the validity of the methodologies utilized for metric extraction and analysis in producing sensible results. As the EEG and MEG data used in this study are two separate openly available datasets, we attempted to match them as much as possible (e.g., in data lengths and preprocessing configurations), thereby allowing comparisons between two modalities to some extent (see *Methods*). While presenting our findings, however, we would like to caution the readers that the

[2]Although frequency ranges used in these studies varied slightly, the alpha and beta bands were generally defined as 8-13 Hz and 13-30 Hz, respectively.

statements made on M/EEG pertain to the specific datasets we used and cannot be blindly generalized to the neuroimaging modalities themselves (see *Discussion*). Acknowledging the unique nature of datasets and their unaccounted variances, our results suggest that MEG may be more sensitive to age-related differences than EEG in source space, and that the age effects observed in the spectral and spatial domains can reveal distinct patterns in the source space RSNs across modalities.

2.2 Methods

2.2.1 Datasets

The resting-state EEG and MEG data used in this chapter are openly available datasets called the Leipzig Study for Mind-Body-Emotion Interactions (LEMON) and the Cambridge Centre for Ageing and Neuroscience (Cam-CAN), respectively. For simplicity, we hereinafter refer to LEMON as the EEG dataset and Cam-CAN as the MEG dataset. Both datasets were obtained from the healthy adults, and recordings were measured while participants were seated. The protocols and demographics related to the data are outlined in [95] for EEG and [96] for MEG in detail and are partly repeated here for clarity.

The EEG recordings from 96 subjects were used for the analysis. The data were obtained using a BrainAMP MR plus amplifier with 62-channel[3] ActiCAP electrodes (Brain Products, Gilchling, Germany). The channel montage adapted the 10-10 layout, which was referenced and grounded at FCz and the sternum, respectively. The acquisition time of the recordings was 16 min, with 1 min blocks alternating between eyes-closed and eyes-open conditions. Signals were collected with a sampling rate of 2500 Hz and bandpass filtered between 0.015 Hz and 1 kHz. For coregistration purposes, the T1-weighted structural MRI (sMRI) was collected over 8 min 22 s, using Magnetization-Prepared 2 RApid Acquisition Gradient Echos

[3]These channels consisted of 61 EEG electrodes and 1 vertical electrooculogram (VEOG) channel. A surrogate horizontal electrooculogram (HEOG) channel was additionally attained by taking the difference between channels F7 and F8 [97].

(MP2RAGE) sequences with a 3T MAGNETOM Verio scanner (Siemens Healthcare, Erlangen, Germany) equipped with a 32-channel head coil.

For MEG, the recordings from 96 subjects were used for the analysis. The data were obtained with a 306-channel Vector View system (Elekta Neuromag, Helsinki, Finland), consisting of 102 magnetometers and 204 orthogonal planar gradiometers. The acquisition time of the recordings was 8 min 40 s, with the first 20 s discarded. Only eyes-closed resting-state data were recorded at a sampling rate of 1 kHz, bandpass filtered between 0.03 Hz and 330 Hz. The eye- and pulse-related artefacts were monitored using two pairs of bipolar electrooculogram (EOG) electrodes and one pair of bipolar electrocardiogram (ECG) electrodes, respectively. For coregistration, the T1-weighted sMRI was recorded for 4 min 32 s, using a Magnetization-Prepared RApid Gradient Echos (MPRAGE) sequence[4] with a 3T TIM Trio scanner (Siemens Healthcare, Erlangen, Germany) equipped with a 32-channel head coil.

To allow us to make some comparisons between the performance of EEG and MEG data, only eyes-closed segments were extracted from the EEG after preprocessing (see below). The mean and standard deviation of the data lengths were 474.4 ± 25.48 s for EEG LEMON and 517.8 ± 63.25 s for MEG Cam-CAN, with an average data length ratio between EEG and MEG resulting in 0.9162. The homogeneity of two datasets was further improved by matching the sample size of each dataset to have an identical age distribution (Fig. A.1). The age-matched dataset comprised a total of 96 subjects, consisting of 60 young (aged between 20-35 years) and 36 old (aged between 55-80 years) participants.

2.2.2 Data Preprocessing and Source Reconstruction

The preprocessing and source reconstruction pipelines were largely adopted from [77] and [97]. The precise protocols applied to the M/EEG data were slightly different due to the unique data characteristics intrinsic to each modality. However, they were

[4]It should be noted that sMRI in LEMON and Cam-CAN used different sequences; contrary to MPRAGE T1-weighted images, MP2RAGE images are less affected by morphometric measurements [95].

aligned as closely as possible to mitigate any unknown variance that could arise from discrepancies in the data preparation. Prior to applying these pipelines, the MEG data were maxfiltered using the temporal signal-space separation (tSSS) method after the data collection to separate recordings of neural activity within the brain from any external noise sources [77]. The entire process of preprocessing and source reconstruction was conducted using the OHBA Software Library (OSL) package [98].

Preprocessing

To account for the subject acclimation and stabilization of measurement devices, we began the initial preprocessing procedure by excluding the first 30 seconds of the recordings from raw EEG and MEG data. These raw signals were then bandpass filtered between 0.5 and 125 Hz using a fifth-order IIR Butterworth filter. A notch filter at 50 Hz and its harmonics was applied to suppress any interference caused by the power line noise. After filtering, the recordings were downsampled to 250 Hz to reduce the computational cost in analysis. Next, the data were segmented into 2-second slices, and the generalized-extreme studentized deviate (G-ESD) algorithm [99] was employed to automatically identify segments with significantly high variance across channels. This same G-ESD approach was utilized to detect anomalous channels within the EEG and MEG data[5]. Further data denoising was performed by applying a FastICA decomposition [100] to the M/EEG channels, decomposing signals into 64 and 54 components, respectively. Components associated with ocular artefacts (i.e., blinks and saccades) were subsequently removed. In the case of MEG, components corresponding to ECG-related artefacts were also excluded. Prior to the ICA decomposition, bad segments from EOG recordings were identified to prevent the inadvertent removal of pertinent M/EEG signals due to concurrent noise artefacts in both M/EEG and EOG. Finally, to keep the data dimension consistent across the subjects, any bad channels detected earlier were interpolated from ICA-cleaned data using spherical spline interpolation [101].

[5]For MEG, bad segment and channel detection procedures were applied separately to different sensor types (i.e., magnetometers and gradiometers).

Source Reconstruction

The source reconstruction of the electrophysiological data is the process of solving the forward-inverse problem. The forward problem refers to predicting the electric potential or magnetic field at each sensor given some source configurations constituting the neural activities within the brain [102]. The inverse problem, on the other hand, attempts to find the location and orientation of the current sources within the brain given the observed data at the sensors [103].

Solving the forward problem typically consists of three steps: extracting brain and skull surfaces, coregistration (of the sMRI, head shape, and device space), and building a head (forward) model. In this study, the surfaces of a scalp, inner skull, and brain were extracted from sMRI data with FSL's Brain Extraction Tool (BET) program [104]. The M/EEG data were coregistered to individual structural images via the iterative closest point (ICP) algorithm using the RHINO (Registration of Headshapes Including Nose in OSL) tool in the OSL package. This step involved matching the digitized Polhemus head points to scalp surfaces for each individual subject. Because the reliability of these head shape points was poor for both EEG and MEG data, the head points and the fiducials were manually adjusted at the individual level prior to M/EEG coregistration to enhance its quality.[6] Finally, the boundary element model (BEM) was chosen as a head model. For MEG, a BEM with a single layer of a scalp surface was utilized, whereas for EEG, a BEM with triple layers of scalp, skull, and cortex surfaces was employed to account for the volume conduction problem.

[6]When submitted to our automatic pipeline, the original headshape points in the EEG and MEG data could not be sufficiently mapped to our estimated scalp surfaces. To improve this mapping, the headshape points were shrunk by 5%, and the fiducials were moved down and back by 1 cm for all subjects in the EEG data. For MEG, the nasion point was dropped by 4 cm, and the headshape points that are more than 7 cm away from this point was kept for all subjects, while removing any points out of left and right pre-auricular points (LPA, RPA) at the horizontal axis. Since headshape points in the MEG data had higher subject variability, they were additionally removed subject-wise using one of the following options: remove headshape points (1) on the face, (2) 1 cm below LPA, (3) 2 cm below LPA, (4) 1 cm abvoe LPA, (5) 2cm above LPA, (6) 3 cm above LPA, (7) below RPA, and (8) 3 cm above RPA. This manual adjustment ensured that headshape points align well with fiducials and scalp surfaces when observed with eyes.

Next, the beamforming method was adopted to solve the inverse problem. The preprocessed sensor data were first bandpass filtered between 1-45 Hz with an IIR Butterworth filter of the fifth order. These signals were source reconstructed onto an 8 mm isotropic grid using a linearly constrained minimum variance (LCMV) beamformer [58, 105]. The rank of a data covariance matrix used to compute the beamformer weights was set to 60 for MEG and 50 for EEG. The vector describing the activity at each source dipole (i.e., voxel) was converted to a scalar by selecting the dipole to be in the direction that maximized the variance explained.

Voxels were then parcellated into 38 anatomically defined regions (see Appendix A.1.2). Source reconstructed signals were obtained by applying principal component analysis (PCA) to these voxel-wise data, wherein a time series of each parcel would be the first principal component that explains most variance from all voxels, weighted by the parcel's spatial map. As the source reconstructed data can suffer from the source leakage problem, the symmetric multivariate leakage reduction technique [106] was additionally applied to minimize the spurious correlations between neighboring parcels that may obscure true connectivity in the RSNs.

Lastly, the volumetric scalar beamforming we used cannot distinguish the polarity of a dipolar source, making the signs of the estimated source-space data arbitrary across channels and subjects [78]. To correct such sign ambiguity, signs of the data time courses were matched by randomly flipping them and choosing the flips that maximize the Pearson correlation of the covariance matrices[7] between subjects. The signs were flipped 5,000 times per subject for the M/EEG data, with a maximum number of 20 channels flipped in each iteration. This process was repeated 3 times, and a set of flips that resulted in the highest correlation was saved for use.

2.2.3 Generative Modeling of Resting State Networks

Once the data were preprocessed and source reconstructed, the next step was to identify different brain networks characterizing the resting state and pinpoint

[7]The covariance matrix was calculated from the source-space parcel time courses. Prior to calculation, these time courses were time-delay embedded with 15 lags and subsequently standardized.

time periods during which they activate. To infer the temporal dynamics of RSNs from the observed data, the source reconstructed M/EEG signals were modelled using the TDE-HMM and DyNeMo. For each dynamic model, an identical set of hyperparameter configurations was used across the datasets.

Data Preparation

The HMM and DyNeMo followed the same procedure of data preparation to incorporate the spectral attributes of a signal into the training data. The source reconstructed data were first time-delay embedded with 15 lags. With a 38-region parcellation, however, this embedding resulted in a total of 570 channels. To prevent overloading the graphics processing unit (GPU) memory and decrease the computational cost, PCA was applied to reduce the dimensionality down to 80 channels (i.e., components). The transformed data were subsequently standardized over time, since the standardization is known to enhance the model optimization process [58]. These prepared data served as the input training data, which was then shuffled and batched prior to model training.

Hyperparameters

The HMM and DyNeMo shared three identical hyperparameters. First, the number of HMM states and DyNeMo modes was set to 8 to ensure a reasonably low-dimensional data representation [58]. Before the data were analyzed, it was validated that 8 states and modes produce interpretable RSNs without any loss in the training quality. Secondly, the batch size necessary for stochastic VB inference was set to 64. Lastly, the HMM and DyNeMo learned the covariances of an observation model, while the mean values were fixed to zero. As discussed in Chapter 1, this was because this project is interested in the transient patterns of spectral events, which are reflected in the covariance when we use time delay embedding.

These models also had different hyperparameters due to their algorithmic nature. The input sequence length for segmenting the data was 800 samples for HMM, whereas it was 200 for DyNeMo. A shorter sequence length was used for DyNeMo due to its RNN-based architecture, which leads to a slower training time if longer

sequences are used. The RNNs can be trained more effectively if shorter sequences are processed in parallel on a GPU, given that it is difficult to allocate longer sequences into GPU memory. On the contrary, since the HMM does not have any RNN component, it can operate on much longer sequences. One advantage following this property is that a longer sequence can provide less noisy updates of parameter estimates as it guarantees fewer discontinuities between the data segments.

Moreover, different numbers of training epochs and learning rates were used. The training epochs were determined empirically to train a model in a reasonable time frame while maintaining an acceptable degree of convergence. For the HMM, the appropriate number was 20, and for DyNeMo, it was 60. As DyNeMo is a larger model and trains for more epochs, it costed a longer wall-clock time. Given that both models utilize the Adam optimizer [107] to update their trainable parameters, learning rates served as one of the most important hyperparameters. They were also chosen empirically to prevent poor updates of the model parameters. For the HMM and DyNeMo, the selected learning rates were 0.001 and 5e-4, respectively.

In addition to the hyperparameters discussed above, DyNeMo has unique hyperparameters related to its design. DyNeMo consists of two architecture components: a model RNN, which describes the latent variables and observation model, and an inference RNN, which learns the variational posterior distributions for the parameters of a model RNN.[8] Both RNNs were built with 64 hidden units with one LSTM layer. The layer normalization was added to avoid vanishing and exploding gradient problems. The temperature of a softmax function, which determines the amount of mixing between modes, was set as a learnable parameter and initialized to 1.

Finally, the total loss of DyNeMo is the sum of the negative log-likelihood (LL) and scaled Kullback-Leibler (KL) divergence, adding up to the variational free energy:

$$\mathcal{L} = -LL + \lambda \cdot KL \tag{2.1}$$

[8]For more details on the architecture of DyNeMo, especially the difference between the model and inference RNN, please refer to [58].

While LL depends on the outputs of the inference RNN, KL divergence depends on the outputs of both the model and inference RNNs. Since the model RNN can influence the inference RNN before the latter learns a logit time course, KL divergence was annealed by the annealing factor[9], λ [58]. For the calculation of this factor, the annealing sharpness was set to 10, and the *tanh* curve was used as the annealing curve. The annealing epoch was set to 40, after which the annealing factor was fixed to 1. The hyperparameters of DyNeMo are explained in more detail in [58].

Model Initialization

As the optimization processes for the models are stochastic, a certain level of run-to-run variability is inevitable. To mitigate this variability, multiple initialization techniques were employed before training a model. For the HMM, we utilized the random state time course initialization method. In this approach, a pseudo-state time course is randomly sampled and used to estimate the covariance matrix for each state at the individual level. These covariance matrices are then averaged across subjects and set as initial covariances. This initialization process was repeated five times, with each run trained for two epochs. The random initialization that yielded the lowest free energy was selected for the full model training. Next, for the DyNeMo model, we used the random subset initialization method. In this method, the learnable parameters are randomly initialized. The model was trained for four epochs, each using different random subset of the training dataset. The size of a random subset was set to half of the total number of batches. This process was repeated ten times. Again, the initialization that resulted in the lowest free energy was chosen for the full model training.

Model Runs

Due to the stochastic nature of the parameter optimization process, different model runs may converge to different local optima. To obtain the best possible parameter estimates, therefore, HMM and DyNeMo models were trained ten times each using

[9]The scaled KL divergence can also be thought of as a regularization term that regularizes the inferred logits for the training data [58].

the same training dataset for both LEMON and Cam-CAN. From these 10 runs, a model with the lowest free energy was selected as the best run. This procedure was again repeated ten times, yielding a total of 100 runs (and 10 best runs) for each model type and dataset (ultimately resulting in 400 model runs and 40 best runs). The best of the 10 best runs, hereinafter denoted as the *optimal* run, was chosen to be used for all subsequent analyses (Fig. A.2). To assess the variability across the best runs and confirm the reproducibility of the results attained from the optimal runs, the metrics of the 40 best runs were additionally compared (see Appendix A.5).

As the order of inferred states or modes is random for each model, it was necessary to align the orders of all best runs to establish their correspondence across the datasets and model types. To achieve this, the EEG and MEG states from the optimal HMM runs were first aligned manually with eyes. Then, for each modality, the order of modes from the optimal DyNeMo run was matched to its respective state order using the linear sum assignment algorithm [108], which used the correlation between the state time courses (i.e., the Viterbi paths) of HMM and the mode mixing coefficients of DyNeMo as a cost matrix. Having the matched state/mode orders of the optimal runs as a reference, orders of remaining best runs were aligned to their reference for each model type and data modality, again using the linear sum assignment method. The quality of alignment within and across model types and data modalities was tested with the optimal runs after their state/mode orders were matched and is documented in Appendix A.1.4.

2.2.4 Summary Statistics of Network Dynamics

Four summary metrics were computed to quantify the temporal characteristics of the HMM states and DyNeMo modes [57, 58]. Because the HMM and DyNeMo infer posterior probabilities of network activations at each time step, we had to first binarize these probabilities to define time points at which the states and modes are activated, namely the HMM state time course and DyNeMo mode time course. For the HMM, the state time course was calculated by applying an argmax operation to the maximum a posteriori probability estimates of the

states. This time course represents the most probable state at each time point, in which only one state is regarded as active.

For DyNeMo, a two-component Gaussian Mixture Model (GMM) was fitted to the mixing coefficients to generate a mode time course for each mode, with one component describing time periods in which a mode is active and the other classifying otherwise. As the mixing coefficients have a sum-to-one constraint, their distributions were non-Gaussian. The distributions were thus transformed closer to Gaussian by using the logit function and standardizing the data before fitting a GMM. GMM was selected over an argmax operation, as it is reported to produce more stable summary statistics for DyNeMo [58]. It is important to note, however, that as a GMM is fitted separately to mixing coefficients of each mode, there can be time points at which multiple or no modes are active.

Using the state and mode time courses, we computed the summary metrics accordingly. These summary statistics were: (1) fractional occupancy (the proportion of the total time spent in each state or mode), (2) mean lifetime (the average amount of time spent in each state or mode before transitioning into other ones), (3) mean interval (the average amount of time elapsed between state or mode activations), and (4) switching rate (the number of state or mode activations per second).

2.2.5 Network Analysis

To further analyze the spectral properties and spatial patterns of the static and dynamic networks, three quantities were calculated: power spectra, power maps, and functional connectivity (FC) maps. FC was measured as amplitude envelope correlation (AEC) and coherence for the static and dynamic analysis, respectively. In this chapter, we used a wide-band frequency range (1-45 Hz) for these metrics unless specified otherwise, as using specific narrow bands mostly led to similar results and conclusions. All the analyses took place within source space, except for the static power spectra, which were examined in both data spaces (i.e., sensor and source space). The analyses described in this subsection were largely adopted from [58] and conducted using the OSL Dynamics toolbox [109].

Power Spectral Densities (PSDs)

The spectral analysis in this study was conducted using PSDs to examine the power distribution across distinct frequency ranges within the neural oscillatory signals. For the static analysis, the Welch's method was employed, yielding an [N x M x K] matrix, where N is the number of subjects, M is the number of sensors (or parcels), and K is the number of frequency bins. This matrix encapsulates the power at each frequency for specific locations and subjects. The computation of each PSD was performed using a 2 s Hanning window with a 50% overlap across a 1-45 Hz frequency range. Prior to these calculations, the dataset was standardized at the individual subject level (i.e., demeaned and variance-normalized). To evaluate and compare the PSDs between the young and old cohorts, the group average of the PSDs was obtained by simply taking the mean of subject-specific PSDs for each cohort, with each subject weighted by the corresponding data length. We then computed the group-level differences by subtracting the group-averaged PSD of the young participants from that of the old participants.

Additionally, to compare age effects in each modality in light of their subject variability, a group-level General Linear Model (GLM) was used, where the data it is fitted to are the sensor(parcel)-averaged power spectra for individual subjects. Note that a separate GLM was fitted to each frequency bin. The group-level GLM contained two regressors that model the group means of the young and old cohort separately. From the fitted GLMs we computed contrast of parameter estimates (COPEs), corresponding to the mean group differences and mean percentage change from the young to old group. For a detailed derivation of the variance and standard errors of these COPEs, please refer to Appendix A.2.1.

To estimate alpha peak frequency, the PSD of each subject was averaged over channels (i.e., sensors or parcels). From each channel-averaged PSD, the peak frequency with the strongest power between 7 and 14 Hz was selected for each subject. The frequency range to detect a peak frequency was set wider than the defined alpha band (8-13 Hz) to account for the shift in peaks due to subject variability and aging effects.

For the dynamic analysis, a power spectrum for each state and each subject was calculated using the multi-taper method [78] for the HMM and the GLM method [58] for DyNeMo, since these two different approaches have previously been found to work best for the corresponding dynamic analyses. As in the static analysis, the PSDs were demeaned and variance-normalized at the individual subject level in preparation for both approaches. In the multi-taper method, a PSD was estimated for each state from a state time course and raw training data (before applying TDE and PCA). The state time course here allows for the selection of time points corresponding to the active states.[10] Hence, for each subject and each state, a multi-taper spectrogram was computed over the entire time points wherein a single state was activated, using 7 tapers with a time-half-bandwidth of 4 (equating to a 2 s time window and 0.5 Hz frequency bin resolution). By averaging a spectrogram over time, an [N x M x K] matrix was obtained for each of the eight states. Additionally, coherence was calculated from the multi-taper cross-spectral densities, resulting in an [N x M x M x K] matrix for each state.

For DyNeMo, the GLM method was favored because its linear mixture description allows multiple modes to activate simultaneously. As the GLM method utilizes mixing coefficients instead of mode time courses, it enables mode-specific power spectra to consider cases in which two or more modes are approximately equally probable. For each subject, the GLM-spectrum was computed by regressing the standardized mixing coefficient time courses onto the spectrogram such that:

$$P_t(f) = \sum_{j=1}^{J} \alpha_{jt} P_j(f) + P_0(f) + \epsilon_t(f) \tag{2.2}$$

where $P_t(f)$ is the cross spectrogram of each pair of sensors (or parcels) measured by the Welch's method at each frequency f (using a 4 s Hanning window and 12.5% overlap), α_{jt} is the mixing coefficient factor for each mode j at time t, $P_j(f)$ and $P_0(f)$ are regression coefficients and intercepts, and $\epsilon_t(f)$ is a residual error. The spectrograms were computed over a 1-45 Hz frequency range. Here, the regression

[10] That is, if the training data is multiplied by the state time course, time points at which a state is inactive will be essentially zeroed out.

coefficients correspond to the mode-specific PSDs, and the regression intercept signifies the mean spectra common to all modes. Again, coherence[11] was calculated for each pair of locations from the summed regression coefficients and intercepts. The dimensions of PSD and coherence match those of the HMM.

These dynamic PSDs are temporally resolved in that they describe state- or mode-specific spectral characteristics, since each state or mode activates at different time points. However, static spectral information common to all transient brain networks may still be present. To further isolate the dynamic information of these networks, the static information shared across all states or modes was removed. For the HMM, the mean across all states was computed and subtracted from the PSDs of each state at the subject level. Likewise, the regression coefficients of DyNeMo were used as the dynamic PSDs devoid of static spectral information, as the regression intercept models the mean over all time points when a covariate regressor is standardized [97]. In the following sections, the mean spectral densities across all states or modes are called *static mean spectra*, and the dynamic PSDs without static spectral information is called *dynamic state/mode-specific PSDs*.

The static mean spectra and dynamic state/mode-specific PSDs were compared between the young and old cohort as described in the static case above. The group averages of these PSDs were defined as the mean of PSDs over all subjects in each group, and the group-level differences were calculated by subtracting the group average of the young cohort from that of the old.

Power Maps

Next, the spatiotemporal distribution of powers in the static and dynamic brain networks was examined. The power in the spatial domain was estimated by integrating the PSD over defined frequency ranges of 1 to 45 Hz (wide-band), 1 to 4 Hz (delta), 4 to 8 Hz (theta), 8 to 13 Hz (alpha) or 13 to 30 Hz (beta). A static power map for each dataset was attained from its respective static PSD. Similarly, state-

[11] As stated in [58], the calculation of coherence from a given window necessitates an averaging of multiple cross-spectra estimates within that window. Therefore, in implementing the GLM-spectrum, each window was segmented into eight smaller sub-windows, and the cross-spectra estimated from these sub-windows were averaged.

and mode-specific power maps were derived from the HMM multi-taper spectra and DyNeMo GLM-based spectra. To probe the aging effects in healthy adults, the power maps of young and old group were averaged across participants, with each subject weighted by the corresponding data length. This resulted in a group-averaged power map represented as an [M x 1] vector for each age group. The group-averaged power map of the young group was subsequently subtracted from that of the old group to underscore the difference in power between the two cohorts. These power maps and power difference maps were plotted as two-dimensional heatmaps projected onto the surface of the brain to illustrate the power at each region of interest. For a smoother visualization, the power values between parcels were voxel-weighted and interpolated. No thresholding was applied to the visualizations.

Like the PSDs, the dynamic information in the power maps was separated by removing the static information common to all RSNs. The mean power across all states or modes was subtracted from the state- or mode-specific power maps at the subject-level. For the HMM, the mean power was weighted by the fractional occupancy of each state. Alternatively, these power maps could also be simply computed from the mean-subtracted PSDs for the HMM and regression coefficients for DyNeMo. These approaches allowed the quantification of the dynamic power features relative to a mean power activity, highlighting the spatial patterns unique to each state or mode.

Functional Connectivity Maps

To quantify the functional connectivity[12] of RSNs and explore the linear relationships between the amplitude or power of different brain regions, FC maps were computed. The static FC was measured using the AEC method, which was previously identified as one of the most consistent methods for stationary connectivity estimation with relatively high test-retest reliability [111]. To compute AEC, the amplitude envelopes

[12]Borrowing the definition posited by [110], functional connectivity estimates "statistical similarities between signals measured from different brain regions and is thought to be indicative of functional integration."

were extracted by applying a Hilbert transform to the orthogonalized and band-limited parcel time courses (see Source Reconstruction). The pairwise correlations between these envelopes were then calculated separately for each subject to produce wide-band static FC maps with a dimension of [N x M x M]. On the other hand, the dynamic FC was measured using coherence measures (see Power Spectral Densities (PSDs)). The coherence provides an index of the stability of phase differences (i.e., phase-locking synchronization of oscillations) between two specified regions of interest. By integrating a coherence matrix of each state or mode over 1-45 Hz, wide-band dynamic FC maps could be computed, resulting in an [N x M x M] matrix.

A group-averaged FC map for each group was obtained by averaging over individual participants within a specific age cohort. The FC group difference was computed by subtracting a group-averaged FC map of the young group from that of the old group. The pairwise connections of the FC maps and FC difference maps were displayed as two-dimensional heatmaps or graph networks projected onto the brain. For the graph network, a threshold of 97-th percentile was applied for better visualization, and connection edges with high AEC/coherence values were selected for plotting.

Like the power maps, the dynamic information in the FC maps was isolated by excluding the static information common to all RSNs. The mean FC across all states or modes, weighted by the fractional occupancy of each state/mode, was subtracted from the state- or mode-specific FC maps at the subject-level. Alternatively, these FC maps could also be simply derived from the mean-subtracted coherences. These approaches allowed the quantification of the dynamic functional connectivity features relative to an average FC activity, revealing the spatial patterns unique to each state or mode.

2.2.6 Statistical Analysis

Following the estimation of static and dynamic brain network features, statistical differences between two age groups in these metrics were examined to probe how age effects are captured by each modality and how modalities compare to one

another. To determine whether there is a statistically significant shift in alpha peak frequencies of the static PSDs, the independent t-test (i.e., the two-sample t-test) was conducted after checking the assumptions of normality and equal variance (using the Kolmogorov-Smirnov test and Bartlett's or Levene's test, respectively)[13]. P-values were adjusted with Bonferroni correction (n=2) to account for multiple comparisons across the data spaces.

We used nonparametric permutation tests for all other statistical analyses, using t-statistics as the permuted statistic [112, 113]. For PSDs, a group-level statistical significance was assessed using a two-tailed cluster permutation test in the MNE software (with clusters formed over frequencies) [114, 115]. In each test, PSDs of each age cohort was inputted as a separate group observation, and group labels were permuted 1,500 times. The t-statistics were calculated using the independent t-test to quantify the group mean difference, with a cluster-forming threshold set to 3.

For summary statistics, power maps, and FC maps, a group-level statistical significance was evaluated using a two-tailed max-t permutation test. First, a metric of interest was fitted to a GLM, in which a separate GLM was fitted to each feature dimension (i.e., states/modes for summary statistics, parcels for power maps, and connection edges for FC maps). A group-level GLM had two regressors modelling the group means of the young and old cohort separately. From the fitted GLMs, we computed COPEs (i.e., mean group differences) and their variances, from which t-statistics could be computed. The regressors of group variables were permuted 10,000 times to build a max-t distribution, and a threshold was extracted from this distribution to test for a statistical significance.

In the case of DyNeMo models trained on the EEG data, outliers were observed in mean lifetimes and mean intervals. These outliers were confirmed to be a result of subject variability and were therefore excluded from statistical tests on summary

[13]The distributions of alpha peak frequencies between the young and old group exhibited homogeneity of variances across all datasets and data spaces. Furthermore, these distributions conformed to normality across the datasets and data spaces, except for those derived from the MEG sensor-space PSDs of the young cohort. For the sake of consistency and due to its stronger statistical power relative to alternative nonparametric methods, an independent t-test was employed for all datasets and data spaces.

statistics and all other EEG DyNeMo analyses. Consequently, subjects with mean lifetime or interval values outside 3 standard deviations above or below the mean were removed. Exclusion of outliers was performed without prior knowledge about the subject age and at the level of an individual model run. Across the 10 best runs, a total of 24 unique outliers (15 young and 9 old) were identified. In each run, the number of outliers ranged from 7 to 15 subjects.

The cluster and max-t permutation tests were utilized to control for the family-wise error rate when testing hypotheses across states/modes, parcels, or frequencies. The use of Bonferroni correction was deemed too conservative in this context, as neighboring oscillatory frequencies or brain regions often exhibit statistical similarities [116]. Additionally, Bonferroni correction was applied to the resulting nonparametric statistics when cluster and max-t approaches were applied multiple times across data spaces, metrics, or states/modes. This correction was applied within the dataset, and tests repeating over modalities (i.e., datasets) were not considered to be a part of the same family.

2.2.7 Reproducibility

Finally, as the temporal dynamics inferred by the HMM and DyNeMo suffer from run-to-run variability, we verified the reproducibility of age-related differences in summary statistics, power maps, and FC maps for each dataset and model type. For summary statistics, the distributions of mean group differences and t-statistics over the 10 best runs were visualized for each state and mode. The number of states and modes that showed statistically significant age-related differences across the runs was reported. For power and FC maps, the average t-statistics over the 10 best runs were plotted as a brain surface map and graph network, respectively. The averaged t-statistics of the FC maps were thresholded at the 97-th percentile for better visualization. Similar to summary statistics, parcels and connections with significant age effects were counted across the runs for each state and mode.

2.2.8 Data and Code Accessibility

For the original LEMON and Cam-CAN data, the readers should refer to [95] and [96], respectively. For preprocessing and source reconstruction, the OSL software [98] was used. All analyses and data visualizations were performed using the custom codes written in Python (https://github.com/scho97/CompareModality). Some of the analyses and visualizations were built upon the OSL Dynamics software [109] (https://github.com/OHBA-analysis/osl-dynamics) and scripts in [97] (https://github.com/OHBA-analysis/Quinn2022_GLMSpectrum). Further requests for prepared data or concerns regarding the codes should be directed to and will be fulfilled by the author (sungjun.cho@psych.ox.ac.uk).

2.3 Results

2.3.1 MEG and EEG reveal comparable static spectral differences between age groups

We started by examining the effect of age on the static (i.e., time-averaged) power spectra (Fig. 2.1). The static power spectra were averaged across sensors or parcels, depending on which data space they were computed in. The group-level cluster permutation tests were then conducted on these spatially averaged PSDs to determine statistical significance along the frequency axis (Fig. 2.2). While age-related differences between the young and old group showed slight disagreements across the data spaces and modalities, we found that static power spectra unveil comparable frequency ranges with age effects in both MEG and EEG.

Across both modalities, the static PSDs in sensor and source spaces consistently reported age effects within the lower frequency (1-8 Hz) and beta (13-30 Hz) bands. Moreover, the alpha band (8-13 Hz) predominantly exhibited no marked age-related differences, except for the sensor space MEG data.[14] The only noteworthy difference

[14]Our evidence suggests that an age effect in the alpha band observed in the sensor space MEG data is likely be due to the subject variability introduced by the random subsampling of the MEG dataset (Fig. 2.2C). Note that the subjects had to be randomly sampled to match the age distributions in the M/EEG data. When tested multiple times with different random subsamples, some tests yielded no age effects in the alpha frequencies.

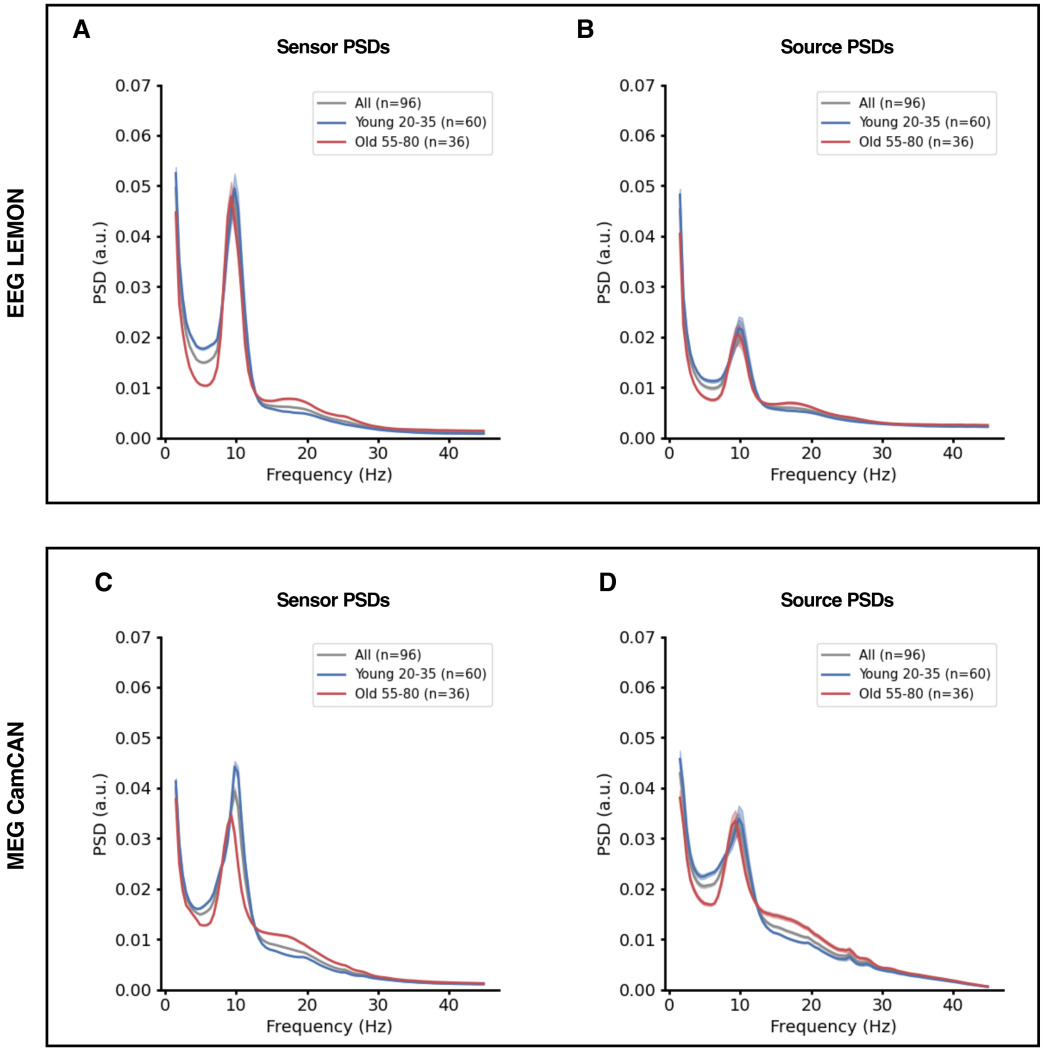

Figure 2.1: Static PSDs in the EEG and MEG data. (A) Sensor space PSDs of the young (blue), old (red), and combined (grey) groups are computed from the EEG data. The PSDs are averaged over subjects and sensors, and the standard errors over sensors are shaded in their corresponding colors. **(B)** Source space PSDs of the age groups and entire dataset are averaged over subjects and parcels. The PSDs are displayed in the same format as in (A). **(C)** Sensor space PSDs are computed from the MEG data using the same analysis as in (A). **(D)** Source space PSDs are computed from the MEG data using the same analysis as in (B).

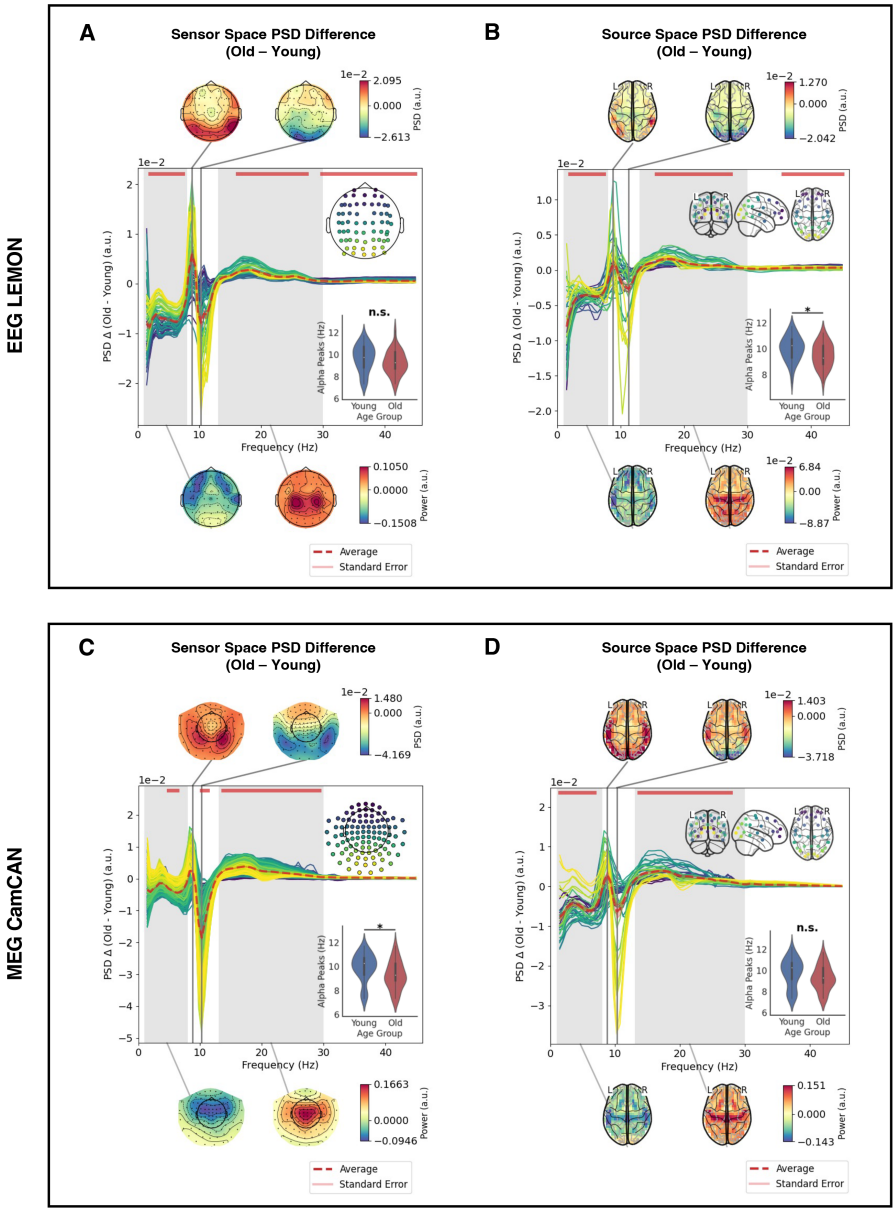

Figure 2.2: Static power spectra in sensor and source space shows frequency-dependent between-group differences. (A) The green lines represent sensor(parcel)-wise PSD differences between the old and young group, accompanied by their average (red dotted line) and standard error (pink shade). Frequency ranges with significant PSD differences are identified through cluster permutation tests on sensor(parcel)-averaged PSDs of the two age groups (red bars) ($p < 0.05$; Bonferroni-corrected, n=2). Each subplot includes two insets. The top-right inset displays the locations of sensors (parcels) corresponding to each PSD difference line, while the bottom-right inset portrays the distributions of alpha peak frequencies for each group, along with their statistical differences. Statistical differences were assessed using the Bonferroni-corrected (n=2) two-sample t-test after the Kolmogorov-Smirnov normality test and Bartlett's/Levene's equal variance test (***: $p < 0.001$, **: $p < 0.01$, *: $p < 0.05$, n.s.: non-significant). The peak differences in alpha power averaged across subjects are plotted as topographies, displayed at the top. The group-level PSD differences were integrated over the lower (1-8 Hz) and beta (13-30 Hz) frequency bands (grey shades) and depicted as topographies at the bottom. **(B)-(C)** The same analysis as described in (A) is applied to (B) EEG source data, (C) MEG sensor data, and (D) MEG source data. For (C), the topographies only display the measurements of magnetometers.

between MEG and EEG was that whereas EEG showed significant age effects in the low gamma (30-45 Hz) band, MEG did not (Fig. 2.2A, B). Despite this disparity, however, MEG and EEG captured similar static spectral age effects. Their similarity is also apparent in the topographic maps showing the differences in the alpha peak power, lower frequency band power, and beta band power between age groups. All of these maps displayed analogous spatial distributions of power across the modalities and data spaces (Fig. 2.2, top and bottom). Having confirmed similar age effects in the source space PSDs, we decided to conduct our subsequent analyses of static and dynamic network features exclusively within source space.[15]

Next, an examination of shifts in alpha peak frequencies was undertaken to ascertain whether the slowing of an alpha peak frequency with age is consistently observed across modalities and to juxtapose this observation with extant literature. Hence, the distributions of alpha peak frequencies were extracted from the sensor- or parcel-averaged PSDs for each age group and compared between age groups. While a significant shift in alpha peak frequencies in the source-space EEG and sensor-space MEG corroborated findings from [86], such shifts were found statistically insignificant in the sensor-space EEG and source-space MEG (Fig. 2.2A, D). Based on this finding, it was difficult for us to assert that alpha peak frequency experiences a shift with healthy aging, and definitive conclusions regarding the dependence of the alpha peak slowing on modality were left elusive for these datasets.

In summary, MEG and EEG demonstrated roughly comparable age effects in static PSDs within both sensor and source space. These age effects were localized in the lower frequency and beta bands. However, the difference between modalities was observed at the low gamma band, in which only EEG reported significant differences between age groups. Regarding the alpha peak frequency shift, no specific conclusion could be drawn about modality differences, since no age effects were consistently observed across the modalities and data spaces.

[15]The rationale behind this decision is multifold. Analysis in source space is more relevant to neuronal information, as it isolates and relates them directly to distinct regions of the brain. This approach allows us to better interpret the results spatially, offering clearer insights into specific brain areas.

2.3.2 MEG and EEG demonstrate distinct age-related effects in wide-band static power maps

We next examined the effect of age on the static wide-band (integrated over 1-45 Hz) power maps. Fig. 2.3A, C shows the group-level power map differences, with both MEG and EEG illustrating qualitatively distinct spatial patterns. While EEG demonstrated pronounced activation in the frontal region amongst the young cohort, MEG had higher frontal, temporal, and parietal activations in the old cohort. Increased occipital activity in the young group was apparent in both modalities.

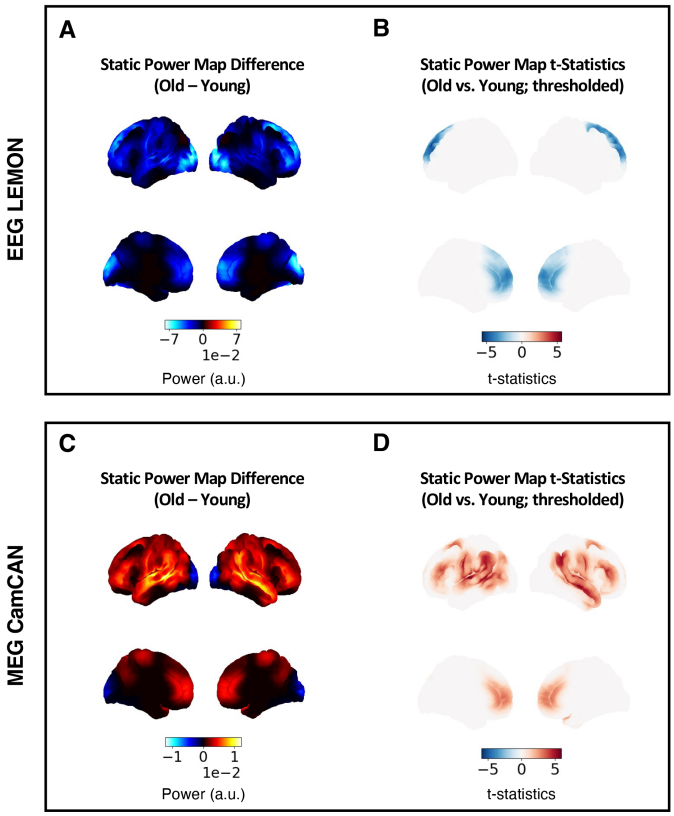

Figure 2.3: Static source-space EEG and MEG reveal distinct between-group differences in the wide-band (1-45 Hz) power maps. (A) Brain surface map of the power difference between the old and young group for the EEG data. The power map of each group was integrated over the frequency range of 1-45 Hz and averaged across subjects, before calculating group differences. **(B)** The max-t permutation test was applied to wide-band power maps of the participants to examine the difference between age groups. The parcels with significant t-statistics ($p < 0.05$) are highlighted. **(C)** Similar to (A), the group-level power map difference is shown for the MEG data. **(D)** As in (B), parcels exhibiting significant between-group differences in power are colored on the brain surfaces. Higher power in old and young participants are represented by red and blue, respectively.

Statistical analysis of age-group differences largely reflected the group-level power map differences mentioned above (Fig. 2.3B, D). However, the occipital region did not show any notable age effects in either modality. Given a well-documented association of the occipital lobe with alpha oscillations (c.f., topographic maps in Fig. 2.2), this observation is consistent in part with our preceding findings in the static source space PSDs, which did not report any significant age effects in the alpha band. For the same analysis on the static wide-band FC maps, readers should refer to Appendix A.3.1.

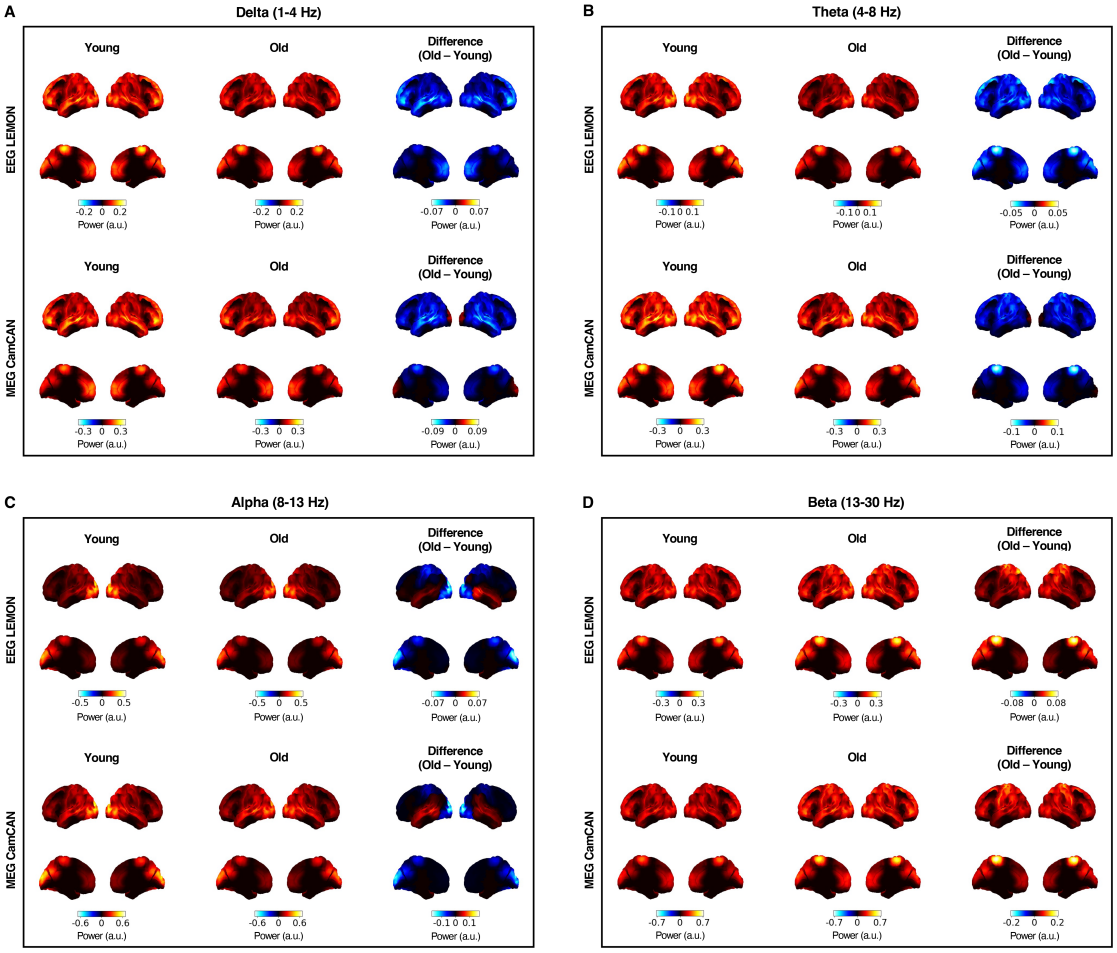

Figure 2.4: Narrow-band static power maps illustrate comparable power spatial distributions between MEG and EEG. (A) Group-averaged static power maps of young (left) and old (middle) participants, along with their subtracted difference (right), are computed from the delta band (1-4 Hz) and depicted for the EEG (top row) and MEG (bottom row) data. The same analysis is repeated for **(B)** theta (4-8 Hz), **(C)** alpha (8-13 Hz), and **(D)** beta (13-30 Hz) bands.

One potential cause of these differences between MEG and EEG is due to

differences in the 1/f aperiodic activity between the two modalities. As can be seen in the subject-averaged static PSDs, the source-space PSD estimates of EEG are characterized by a steeper exponential decay compared to those of MEG (Fig. 2.1). This dissimilarity in slope indicates that the power at each frequency contributes differently to each modality when they are integrated over the wide band. When static power maps were partitioned into narrower bands, the resulting spatial patterns of mean group power differences were more qualitatively analogous across the modalities (see Fig. 2.4). Furthermore, the statistical significance of these differences was also roughly comparable between MEG and EEG (Fig. 2.5).

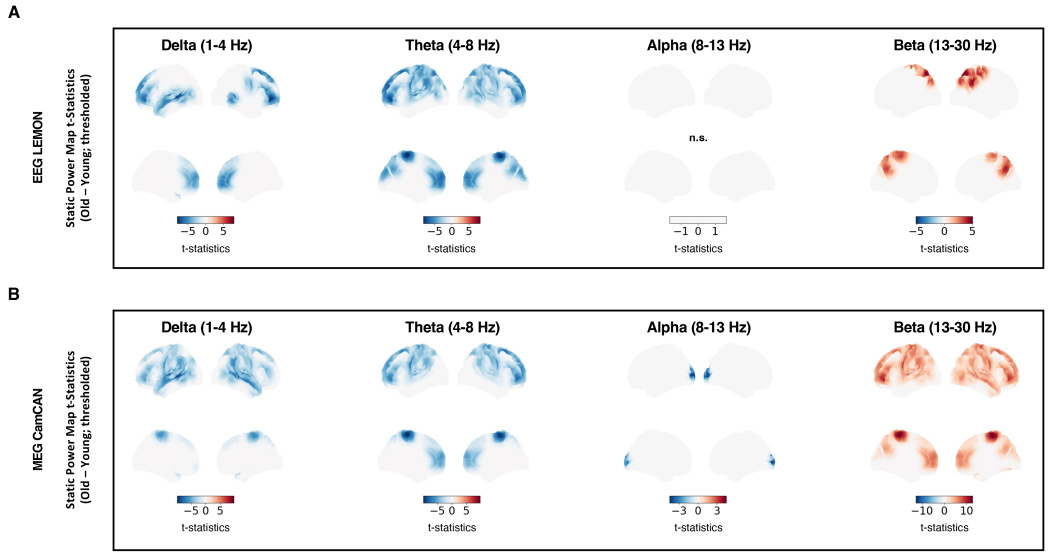

Figure 2.5: Age effects in narrow-band static power maps are analogous between MEG and EEG. (A) The max-t permutation tests ($p < 0.05$; Bonferroni-corrected, n=4) were applied to narrow-band static power maps of the EEG data to highlight the difference between age groups. The parcels with significant t-statistics are highlighted. The power maps show lateral surfaces at the top and medial surfaces at the bottom. Higher power in old and young participants are represented by red and blue, respectively. Non-significant results are labeled as n.s. **(B)** The same analysis as in (A) is conducted for the MEG data.

In summary, our examination of MEG and EEG in this section delineates their unique spatial patterns of age effects in wide-band static power maps. The divergence observed in power maps could be attributed to non-sinusoidal aperiodic activity, although the origins of this aperiodic component — whether they emanate from source reconstruction, unaccounted variance within the datasets, or neural and

physiological signals measured by the modalities themselves — remain a subject of further investigation. Age effects in M/EEG were much more comparable in narrow-band static power maps.

2.3.3 MEG shows more pronounced age-related effects in network dynamics than EEG

Next, we examined the effect of age on summary metrics of the network dynamics obtained using the HMM. RSNs inferred from the HMM were matched across the modalities to make the comparison between EEG and MEG HMM states congruous (Fig. 2-6). Upon inference, these states were associated with the canonical RSNs based on their spatial power distributions. For EEG, State 1 represents the visual network; State 2, the sensorimotor network; States 6 and 8, the anterior DMN; State 7, the posterior DMN; and States 3, 4, and 5, the other networks that cannot be clearly identified. For MEG, States 1, 3, and 8 represent the visual network; State 2, the sensorimotor network; State 6, the anterior DMN; State 7, the posterior DMN; and States 4 and 5, the other networks.[16]

In EEG, State 8 showed statistically significant age effects across all summary metrics following max-t permutation tests (Fig. 2-7A-D). In MEG, State 4 displayed age effects in fractional occupancy, mean lifetimes, and mean intervals (Fig. 2.7E-H). A comprehensive power map of each state, when averaged over entire subjects, illustrated a noticeable power suppression in the occipital region relative to the average across all states (Fig. 2.7I, J). The EEG state, however, also showed heightened activation in the frontal region.

When we replaced the HMM with DyNeMo, a clear discrepancy was observed between MEG and EEG. Whereas EEG did not show any modes with statistically significant age effects, three distinct modes were identified in MEG as having

[16]Depending on how the model is trained, a specific canonical RSN may divided into multiple distinct states. Additionally, there are instances where components considered as noise or neural activities not typically associated with canonical spatial patterns may constitute what is termed *other networks*. Due to the variability in model training and datasets, it is not always true that multiple model runs on the same dataset or a single model run across modalities produces perfectly matching states with identical correspondence to canonical RSNs. For more detailed information and visualizations of HMM states and DyNeMo modes, as they relate to canonical RSNs, readers should refer to [58].

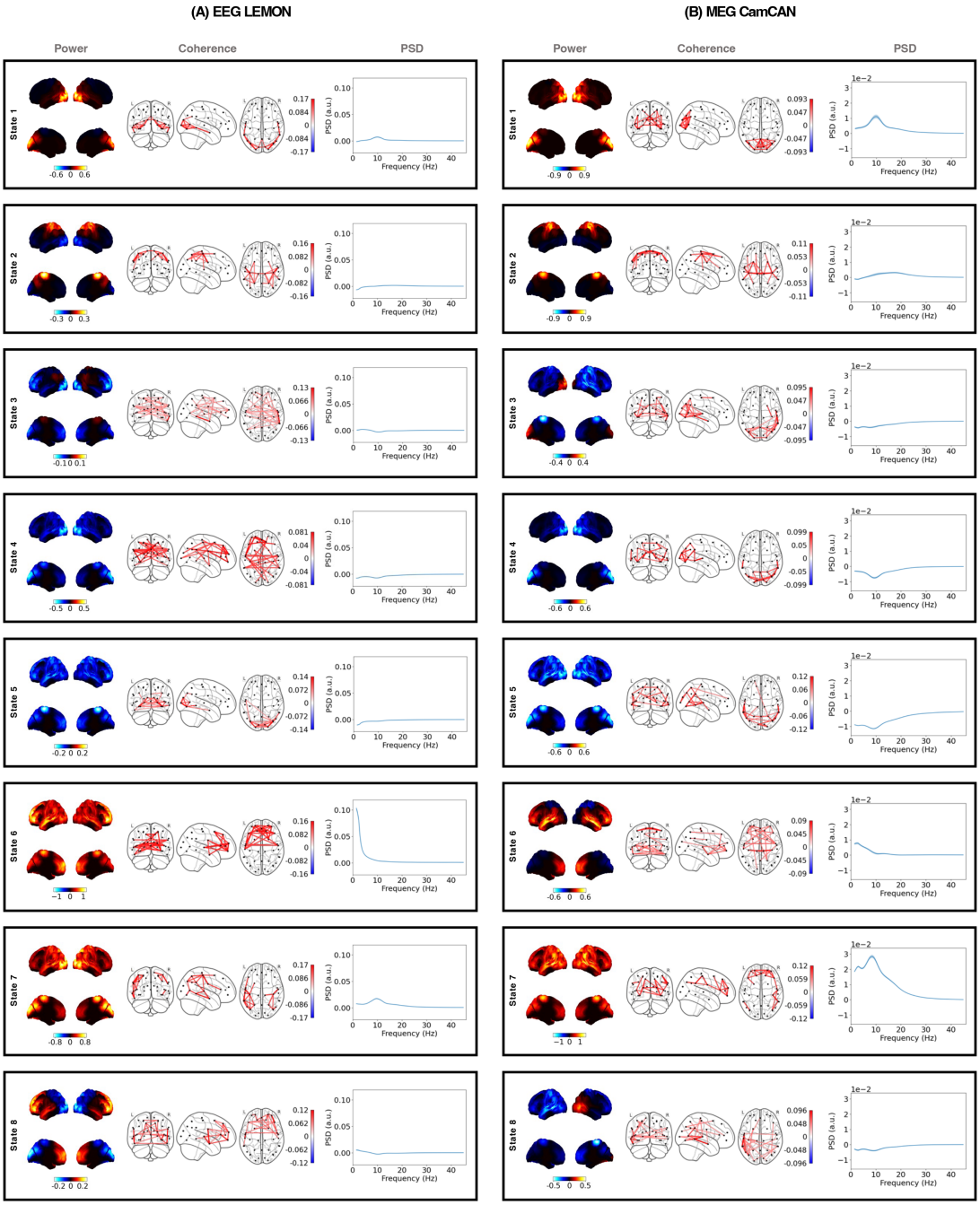

Figure 2.6: HMM resting-state network states inferred from the EEG and MEG datasets. (A) Each box shows the power map (left), FC network (middle), and parcel-averaged PSD (right) of each HMM state for 96 EEG subjects. The power maps show lateral surfaces at the top and medial surfaces at the bottom. The FC networks illustrate connections with the top 3% coherence values. The shaded areas of the PSDs represent the standard error of the mean. The power maps, FC networks, and PSDs are visualized relative to their average across all states. **(B)** The plots follow the same format as (A), showing the RSNs computed from 96 MEG subjects.

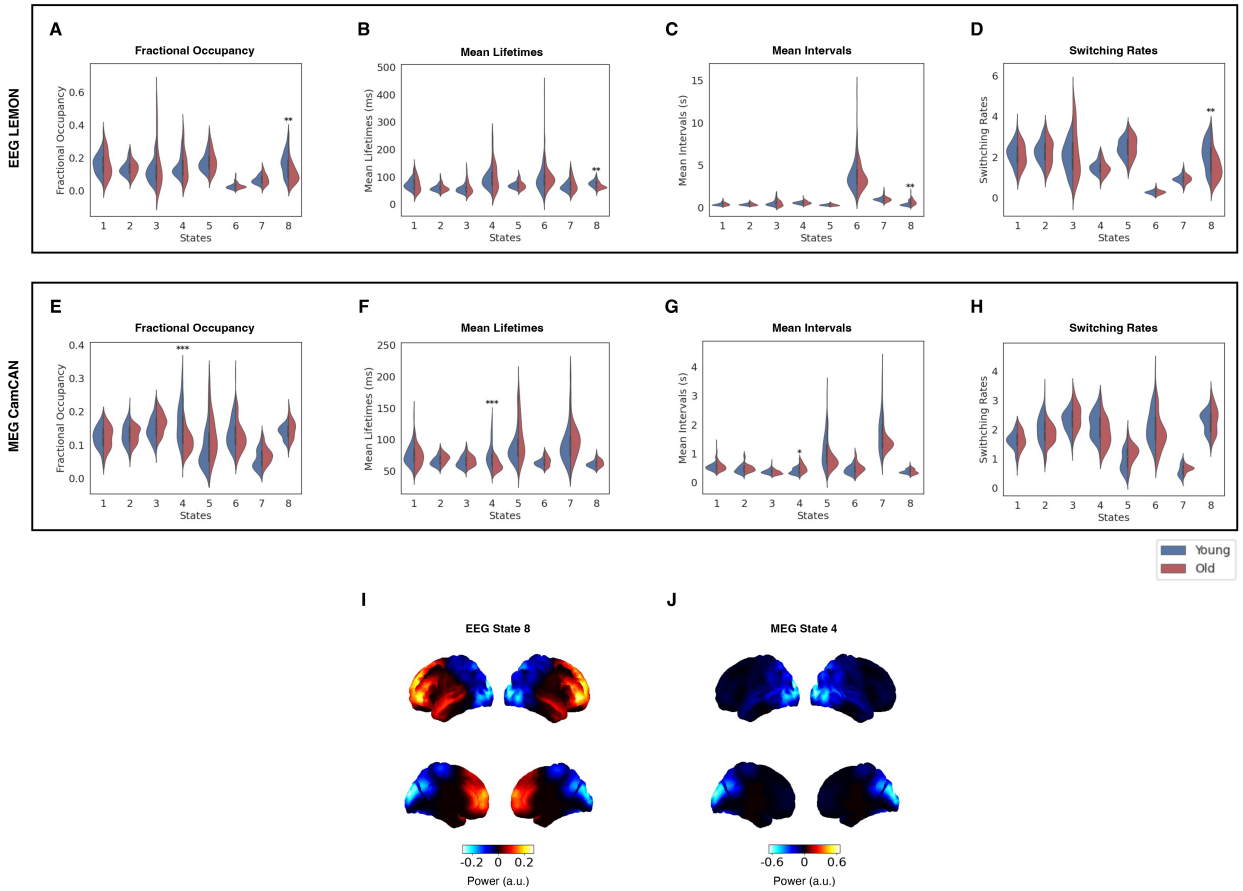

Figure 2.7: Source-space MEG and EEG report distinct dynamic age-related effects in HMM summary statistics. Summary statistics of the state time courses inferred from the EEG data – **(A)** fractional occupancies, **(B)** mean state activation lifetimes, **(C)** mean state activation intervals, and **(D)** state switching rates – are plotted as distributions over the grouped subjects. **(E)-(H)** Same plots for the MEG data are presented. The states showing significant between-group differences are marked by asterisks. Statistical significance was determined using max-t permutation tests for each dataset, Bonferroni-corrected by the number of metrics (n=4). (***: $p < 0.001$, **: $p < 0.01$, *: $p < 0.05$, n.s.: non-significant) **(I)** A wide-band (1-45 Hz) power map of State 8 in EEG, averaged over the entire subjects, are illustrated. **(J)** Likewise, a wide-band power map of State 4 in MEG is depicted.

significant differences in summary metric values between the age groups (Fig. A.8). Yet, the spatial patterns of power in these MEG modes did not mirror the aforesaid MEG HMM state but rather highlighted increased activation in the sensorimotor and temporal regions (Fig. A.8I-K).The observations on both HMM states and DyNeMo modes demonstrated consistency across each summary metric over multiple model runs, increasing confidence that the observed disparities between M/EEG in representing age effects are reliable and robust (see Appendix A.5.1).

In summary, MEG demonstrated more pronounced age-related effects in summary metrics of network dynamics than EEG. This finding suggests that MEG can potentially be more sensitive to age effects represented by the timings of RSN activation. Such observation was conspicuous with DyNeMo but not with the HMM. For the HMM, although both MEG and EEG reported age effects in a single network state, these states were distinct from one another and showed different spatial patterns of power.

2.3.4 MEG and EEG report distinct sets of dynamic brain networks with age-related spectral differences

Expanding on the static spectral analysis, we examined the effect of age on the state-specific PSDs found using the HMM. We computed the static mean across all HMM states and subtracted it from the state-specific PSDs, thereby isolating the static and dynamic information from one another. Reassuringly, the static mean spectra reflected age-related effects previously noted in the static PSDs for both EEG and MEG (Fig. 2.8A, C; Fig. 2.2). This also highlights how any results we find on the residual dynamics can be considered as distinct from the static effects we have already seen.

For each modality, a group-level statistical assessment of dynamic state-specific PSDs showed significant age effects within delta, beta, and low gamma (30-45 Hz) frequency bands. These frequencies were largely comparable to those identified from the static mean spectra as having age-related effects (Fig. 2.8B, D). However, slight differences did exist for some states. State 8 in EEG revealed age effects at

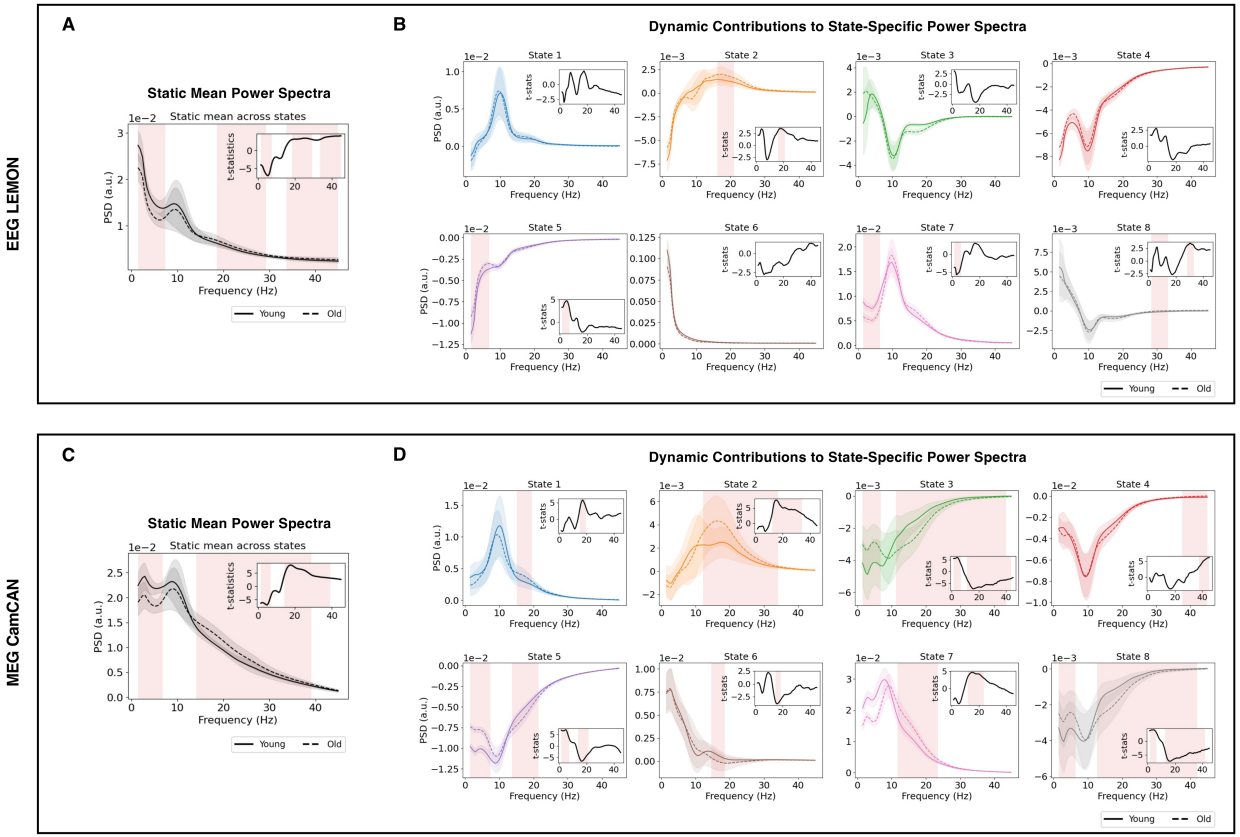

Figure 2.8: Source-space EEG and MEG HMM states report distinct spectral differences when dynamic information is isolated. **(A)** The mean PSD across all states is obtained from the EEG data for young (solid) and old (dotted) participants and averaged over the subjects and parcels. A cluster permutation test is conducted on the parcel-averaged static mean PSD to detect age-related static effects. Frequencies exhibiting statistical significance ($p < 0.05$; Bonferroni-corrected, n=9) are highlighted in red. **(B)** The state-specific PSDs of the EEG data are averaged across each group and parcels after the mean across states is subtracted at the subject level. These group-averaged, mean-subtracted PSDs of young (solid) and old (dotted) participants are illustrated for each HMM state. Cluster permutation tests are conducted on parcel-averaged, mean-subtracted PSDs of each state to detect age-related dynamic effects. Frequencies exhibiting statistical significance ($p < 0.05$; Bonferroni-corrected, n=9) are highlighted in red. **(C)** The same analysis as in (A) is performed on the MEG data. **(D)** The same analysis as in (B) is performed on the MEG data. For all plots, the inset portrays t-statistics contrasting its corresponding PSDs of the young and old group.

approximately 28-33 Hz, which did not overlap with the frequencies reported in the static mean spectrum. Likewise, States 7 and 8 in MEG additionally detected age effects at about 13-15 Hz and 39-42 Hz, respectively, which extended beyond the frequency ranges reported in the MEG static mean spectrum. Interestingly, MEG delineated more dynamic states with age-related effects than EEG, marking every state to have significant age effects compared to four states in EEG. It is noteworthy that even when MEG and EEG identified same states to have meaningful age effects, the frequencies associated with these effects differed. For example, State 7 showed age effects in the delta band for EEG, but the same state revealed age effects in the beta band for MEG.

Next, we repeated cluster permutation tests on mode-specific regression-based PSDs, inferred from DyNeMo, again after separating the static and dynamic spectral components (Fig. A.9). For both EEG and MEG, the corresponding static mean spectra across all modes consistently reflected age effects that were previously observed in the static PSD analysis (c.f., Fig. 2.2). As in the case of HMM, dynamic mode-specific PSDs of both modalities revealed frequency ranges with significant age effects that resemble those detected from their respective static mean spectra. However, MEG Modes 1, 5, 7, and 8 also found significant age effects in the alpha or gamma frequencies, which were undetectable in the static mean spectrum.[17] In line with the findings from state-specific PSDs, MEG depicted more dynamic modes with age-related effects than EEG, reporting seven states to have significance compared to two states in EEG.

In summary, regardless of which dynamic model we use, RSNs exhibiting age-related spectral effects varied between MEG and EEG. In general, more dynamic states and modes had age effects in MEG than EEG. This discrepancy between modalities putatively implies that MEG may display a greater sensitivity to age effects in dynamic spectral information than EEG.

[17]Here, we should consider the subject variability concerning the alpha band, as discussed in the previous sections.

2.3.5 Dynamic age-related effects in wide-band power maps are more marked in MEG than EEG

To elaborate on our findings on the static power, we lastly examined the effect of age on the state-specific power maps found using the HMM.[18] As before, to distinguish static from dynamic effects, the static mean power maps obtained by averaging across all HMM states were removed from their respective state-specific power maps.

In the EEG data, significant age-related effects were observed solely in the static mean power, as evidenced by group-level max-t permutation tests on both static mean and dynamic state-specific power maps (Fig. 2.9A). On the other hand, age-related effects in MEG were reported not only in the static mean power map but also across the spatial power distributions of all states (Fig. 2.9B). These age effects were consistently reproduced across the best model runs (see Appendix A.5.2). As in the analysis of the state-specific PSDs, static mean power map differences (i.e., unthresholded t-statistics) between the old and young cohort roughly mirrored spatial patterns that were previously found in the static analysis (c.f., Fig. 2.3A, C). Significant age effects in the static mean power corresponded to findings from the previous static analysis as well (Fig. 2.3B, D; Fig. 2.9). Specifically, stronger power was observed in the prefrontal cortex of the young participants in EEG. In MEG, increased activation in the frontal and temporal lobes was highlighted for the old group, although age-related effects also extended to the sensorimotor and occipital regions.

The identical approach was repeated on the static mean and dynamic mode-specific power maps inferred by DyNeMo. Statistical analysis of age-group differences unveiled age effects in the static mean power maps of both MEG and EEG, while also reporting age effects in dynamic mode-specific power maps for Modes 1, 2, 4, 5, and 7 in MEG (Fig. A.10). All of these effects were confirmed to be reproducible across model runs, except for MEG Modes 1 and 5 which showed limited reproducibility

[18]For the power and FC maps of HMM states and DyNeMo modes that are averaged across all subjects, refer to Fig. 2.6 and Fig. A.7. These maps illustrate the degree of alignment between states and modes, providing an additional validation for our comparison of state- and mode-specific power and FC maps.

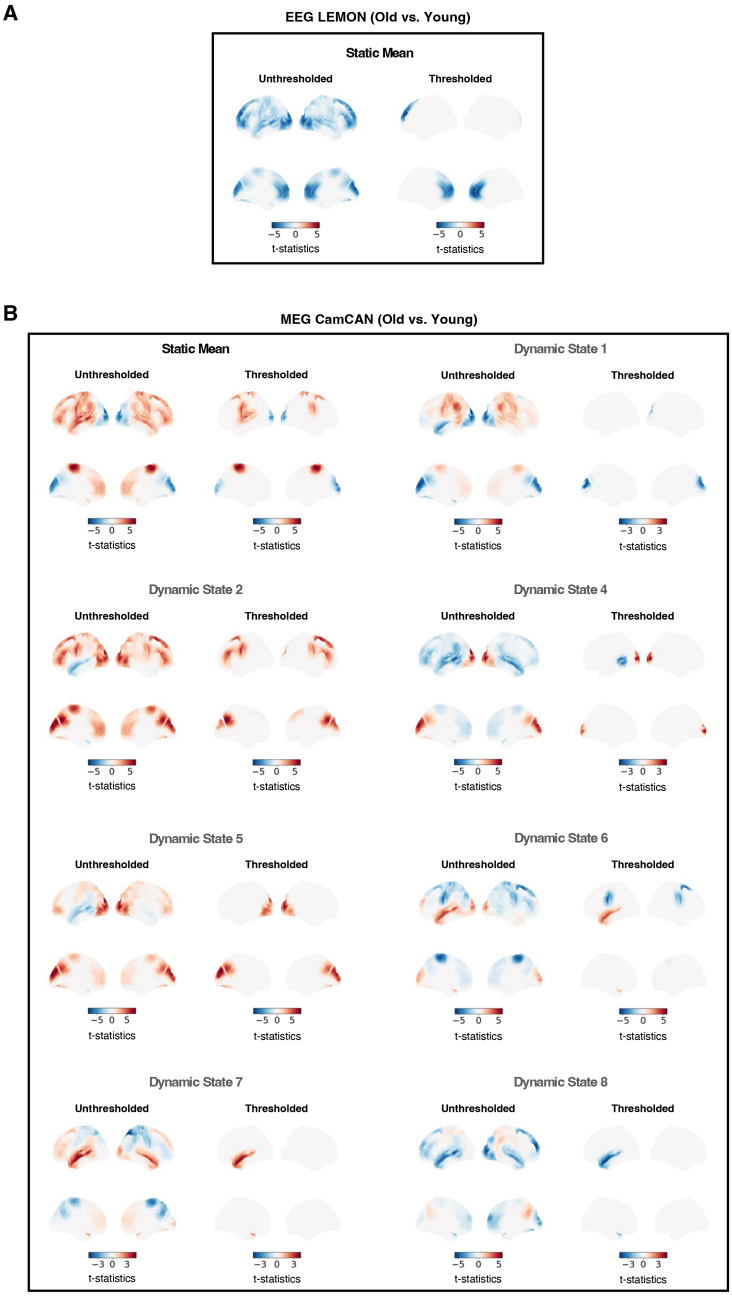

Figure 2.9: Dynamic age effects in spatial power distributions are observed in source-space MEG HMM states but not in EEG. The result of statistical analysis conducted on the wide-band (1-45 Hz) static mean and dynamic state-specific power maps is presented here. Only the power maps with significant age effects are plotted. **(A)** Power maps with significant between-group differences are illustrated for the EEG data. Power maps on the left display t-statistics between groups, and the parcels with significant t-values are colored on the right. Only the static mean power map revealed meaningful age effect in EEG. **(B)** The same analysis is performed on the MEG data. Max-t permutation tests were used to evaluate statistical significance. Parcels are marked significant if $p < 0.05$ (Bonferroni-corrected, n=9).

due to their relatively higher run-to-run variability (Fig. A.17). Again, age-related effects in the static mean power maps portrayed spatial distributions reflective of the static analysis, though age effects in EEG were restricted predominantly to the dorsolateral prefrontal cortical region.

Finally, we explored the relationship between power and coherence for each dynamic brain network. For each modality and age group, we plotted mean-subtracted power and coherence values across states/modes and ROIs (Fig. A.13). HMM-derived power and coherence measures demonstrated vastly distinct patterns between modalities. Whereas MEG exhibited U-shaped joint distributions of power and coherence, EEG showed linearly correlated distributions. With DyNeMo, distributions of power and coherence looked similar for M/EEG, but MEG modes were associated with higher power values. Regardless of the model types, EEG had a higher global coherence in general.

In summary, MEG displayed enhanced sensitivity in detecting dynamic age effects in power maps when compared to EEG. Moreover, the distributions of power and coherence across states and modes showed distinct patterns and values in MEG and EEG. This modality difference additionally hints a possibility that MEG and EEG measure partly idiosyncratic dynamic RSN activity.

2.4 Discussion

2.4.1 Conclusion

In this chapter, we evaluated the efficacy of MEG and EEG in discerning age-related effects in various brain network features. We highlighted potential discrepancies between MEG and EEG and validated the methodologies applied to different neuroimaging modalities, thereby providing insights into our understanding of RSN characteristics in the healthy population, a point that will be further elucidated in the subsequent chapter.

Modality Differences in Detecting Age Effects

Our analysis showed that age-related effects derived from the M/EEG data are largely comparable within static PSDs and narrow-band power maps. This result implies that both modalities capture similar age effects when relevant resting-state network features are averaged over time. Nonetheless, our examination of effect sizes in static PSDs indicated that the relative dominance of MEG or EEG in its size of age effects depends on the metric used (i.e., mean group difference, mean percentage change) and specific frequency bands (Fig. A.4). Therefore, albeit largely analogous, each modality appeared in part to be able to display distinct age effects in certain data domains and features, hinting at their potential complementary attributes.

Such conclusion became clearer with our findings from the dynamic analysis, from which we could observe modality differences in dynamic age-related effects to some extent. RSNs derived from MEG were more sensitive to age effects in summary statistics, PSDs, and power maps than EEG, and these effects were distinct between modalities across various states and modes.

However, while MEG indicated possibly better sensitivity to static FC than EEG, we could not yield definitive conclusions on modality differences regarding connectivity in the dynamic analysis. As discussed in Appendix A.4.4, age may not affect RSN connectivity as strongly as it does on RSN power, hindering our models from accurately capturing age effects in dynamic FC.

Validation of Methodologies

Another pivotal aspect of our study was methodological validation. As depicted in the Results section, our findings either qualitatively or quantitatively aligned with previous literature, reaffirming the validity of our techniques. In Section 2.3.2, we ascertained that the age effects in narrow-band static power maps are consistent with previously documented age effects [87–90]. Corroborating our findings with existing literature, beta band activity in the sensorimotor and frontal regions was observed to significantly increase with age for both MEG and EEG. For MEG specifically, we further confirmed a significant decrease in alpha band

activity in the occipital region. These results[19] together added some robustness and validity to our methodological approach in reliably capturing previously known age effects from resting-state M/EEG data.

It is also worth noting that the differentiation between EEG and MEG in identifying dynamic age effects was sometimes more pronounced in DyNeMo compared to HMM. For instance, in Section 2.3.3, age effects in RSN summary metrics were identified in MEG but not in EEG with DyNeMo, while age effects were reported for both M/EEG with the HMM. This tendency is anticipated since DyNeMo offers a more intricate recapitulation of network dynamics as a linear mixture model, without presupposing mutual exclusivity of RSNs and first-order Markovian properties. As it can describe multiple modes or even the absence of any mode activation at a specific time point, such traits might have rendered DyNeMo modes more adept at capturing nuanced brain network activations that vary across individual subjects and age groups. However, one repercussion of DyNeMo modeling following this advantage is that it may lead to increased run-to-run variability, as evident from our reproducibility study (see Appendix A.5.1), because DyNeMo can find more than one solution for its model parameter estimates. Nevertheless, both the HMM and DyNeMo, which were originally developed for analyzing MEG data, demonstrated that they can be used to successfully infer the transient RSN dynamics from EEG.

Recognizing all of the points above, our study overall confirmed that the analysis techniques initially designed for MEG data can be effectively applied to EEG data and produce reasonable results subjected to our interpretation.

2.4.2 Limitations

As mentioned at the outset, the distinction between MEG and EEG identified in this study is confined to and limited by our datasets. It is difficult to generalize

[19] Although without statistical significance and only in a qualitative manner, an increase in beta activity in the temporal areas and a decrease in alpha activity in the parietal lobes with age were additionally noticed.

that the disparities between these two modalities mainly stem from the unique neural activities measured by each modality, given that:

1. The use of different datasets introduces unaccounted variance in attributes like subject demographics, recording sites, and other cognitive and physiological traits.

2. Random subsampling of the LEMON and Cam-CAN datasets additionally contributes to subject variability.

For the latter, one should note that the age distribution of participants in each dataset was matched as much as possible, even at the cost of sacrificing a sample size. We implemented a strict subsampling on the data to ensure that the incongruity in subject ages between age groups does not influence any age-related effect we observe. We anticipate that the effect sizes of age-related differences can be amplified if a larger sample size is available. For instance, the observations on the alpha peak shift in the sensor-space EEG and source-space MEG might achieve statistical significance with more data (Fig. 2.2).

Given these complexities, therefore, it is hard for us to conclude that MEG outperforms EEG in capturing age-related effects, especially dynamic ones, across diverse brain network features. Nonetheless, we can posit that these modalities do have meaningful similarities and differences and that, recognizing the aforesaid sources of variance, each modality may convey unique, complementary information.

In terms of the methodology, we reckon that the source-space MEG data have a higher spatial resolution compared to EEG. This characteristic is attributed to the greater sensor counts (306 sensors) of MEG in contrast to the 61 electrodes of EEG. Such difference might elucidate why M/EEG exhibit inconsistent exponential decay (i.e., aperiodic activity) in the group-averaged static PSDs within the source space (Fig. 2.1). It is plausible that MEG, with its enhanced spatial resolution, has more accurately represented the underlying physiological and neuronal signals. Another limitation to address is that while age effects were quantitatively assessed within each dataset, their comparison between the modalities was qualitative.

Finally, it is crucial to understand that aging is a gradual biological process affecting the entire brain and body of an organism throughout its lifetime. It may therefore be challenging to detect dynamic RSN activities that are associated with healthy aging on a millisecond scale. This property of aging may explain the lack of dynamic age effects in FC among the age groups (see Appendix A.4.4) and why spectral age effects in dynamic RSNs were akin to those seen in their static mean PSDs (Fig. 2.8; Fig. A9).

In the next chapter, we will discuss how the design of the NTAD dataset addresses most of the aforementioned limitations and integrate the insights from this chapter into our analysis of NTAD.

3

M/EEG Brain Network Features as Biomarkers for Alzheimer's Disease

Contents

3.1 Introduction

The quest to identify biomarkers of AD in resting-state M/EEG has spanned many years. Over the past two decades, researchers have widely explored the differences in RSN power and FC between healthy individuals and AD patients, and many effects of AD have been reported in static brain network features. It was found that the static M/EEG-derived RSN in individuals consistently displays a relative increase in delta and theta power and a relative decrease in alpha and beta power across various brain regions, including the orbitofrontal, occipital, temporal, and parietal cortices, when compared to the healthy elderly population [117–121].[1] Further, in

[1]Although frequency ranges used in these studies vary slightly, the frequency bands were generally defined as delta (0.5-4 Hz), theta (4-8 Hz), alpha (8-13 Hz), and beta (13-30 Hz). The delta band was most variable, with its lower frequency bound often set as 0.5, 1, or 2 Hz.

resting-state, eyes-closed MEG, subjects with MCI exhibited increased FC within the theta band in frontal and parietotemporal regions [117], whereas diminished FC in the alpha and beta band was observed across temporal cortices in early-stage AD [122] and within fronto-frontal and frontoparietal areas in MCI [117]. A global decrease in FC in the alpha and beta band, specifically in leakage-corrected AEC measures, was reported in the resting-state, eyes-closed EEG data as well [118].

On the other hand, only a handful of studies have focused on the dynamic effects of MCI and AD on RSNs. The majority of reported findings on these effects pertain to the DMN. A study by Sitnikova et al. (2018) revealed that the DMN in AD patients activates less frequently and for shorter periods of time compared to healthy controls, signaling that the likelihood and stability of DMN activation are compromised in these patients [49]. Research by Puttaert et al. (2020) confirmed that the posterior DMN exhibits reduced activation for shorter duration in AD patients compared to healthy individuals [123].[2] Although this study is arguably first to investigate the dynamic attributes of resting brain activity in early-stage AD using an HMM approach, they did not find any significant AD effects in transient resting-state brain dynamics of patients at their pre-clinical (with subjective cognitive decline) or pre-dementia (with amnestic MCI) stage. Thus far, therefore, limited studies have explored dynamic effects in both MEG and EEG during rest, and no concrete and reproducible biomarkers have been observed from patients with MCI and early-stage AD with regard to dynamic M/EEG RSNs.

In this chapter, we aim to address whether static and dynamic changes in M/EEG-derived RSN features can adequately represent the neuronal and physiological alterations in the human brain that are induced by AD during its early development. To fulfill this objective, we concentrate on two primary tasks. First, we will confirm the reproducibility of previously known M/EEG biomarkers from our dataset. Secondly, we will explore the potential of dynamic RSN features as a novel and clinically relevant set of biomarkers that is sensitive to the presence of MCI and early-stage AD. In the following sections, we will contrast healthy subjects with those

[2]AD-related aberrations in DMN FC have been corroborated by fMRI studies as well [124, 125].

affected by MCI or early-stage AD to investigate how the disease modifies static and dynamic network properties during rest. We employed the same analysis pipeline that was developed and validated in the preceding chapter to scrutinize these effects.

3.2 Methods

3.2.1 Dataset

The resting-state EEG and MEG data used in this chapter were collected as a part of the NTAD study. M/EEG data were recorded simultaneously in a magnetically shielded room while participants were seated. The protocols and demographics related to the data are outlined in [20] in detail and are partly repeated here for clarity.

The M/EEG recordings from 78 subjects were used for the analysis. The data were recorded from two sites, Oxford and Cambridge. At Oxford, the data were obtained using the MEGIN Triux Neo M/EEG scanner (MEGIN, Surrey UK) with a 60-channel EasyCap EEG (Brain Products, Gilchling, Germany). At Cambridge, the data were attained using either the VectorView system (Elekta Neuromag, Helsinki, Finland) with a 70-channel EasyCap EEG or the MEGIN Triux NEO M/EEG scanner with a 64-channel EasyCap EEG. All MEG scanners had a 306-channel system, consisting of 102 magnetometers and 204 orthogonal planar gradiometers. All EEG channel montages adapted the standard 10-20 layout, which was referenced and grounded at the left side of the nose and left cheek, respectively. Out of different task and resting-state data, we used resting-state eyes-closed recordings. Signals were collected with a sampling rate of 1000 Hz, and the acquisition time of the recordings was approximately 5 min 50 s.

Along with the M/EEG measurements, VEOG and HEOG were recorded with electrodes positioned above and below the left eye and on bilateral canthi, respectively. ECG data were recorded from the electrodes on the right clavicle and left lower rib. For coregistration purposes, the T1-weighted sMRI was collected over 5 min 12 s, using MPRAGE sequences with 3T PRISMA scanners (Siemens

Healthcare, Erlangen, Germany) at the Cambridge MRC Cognition and Brain Science Unit and Oxford Centre for Human Brain Activity.

All participants were aged between 50 and 85 years. Participant demographics including sex, age, and MMSE score and their group-level comparisons are summarized in Table B.1. The NTAD data were divided into two groups for comparison. First group consisted of healthy, elderly participants with normal cognition (n=27) and is denoted as the amyloid negative (AN) group. Second group consisted of participants with symptomatic MCI or early AD (n=51) and is denoted as the amyloid positive (AP) group. As indicated by the group name, all participants with MCI or early-stage AD were diagnosed to be amyloid positive, whose positive amyloid status was tested using CSF or amyloid PET. Amyloid positivity was additionally used to screen AP participants, given that clinical criteria alone cannot reliably diagnose the presence of AD pathology [20]. Among the AP group, 28 subjects had MCI and 23 subjects were diagnosed with early-stage AD.

3.2.2 Data Preprocessing and Source Reconstruction

The preprocessing and source reconstruction pipelines used in this chapter follow a procedure similar to that outlined in Chapter 2. The same set of algorithms were employed using the OSL package [98]. Hence, the repeating details are omitted here where possible to avoid any redundancy. Note that the precise protocols applied to the MEG and EEG data were different due to the unique data characteristics intrinsic to each modality. Prior to applying these pipelines, the MEG data were maxfiltered using the tSSS method to eliminate any external noise sources [77]. Moreover, four channels (i.e., O1, O2, Oz, Iz) had to be dropped from 70-channel EEG data recorded in Cambridge, because their channel positions were unavailable.

Preprocessing

We began the initial preprocessing procedure by excluding the first 20 seconds of the recordings from raw EEG and MEG data. These raw signals were then bandpass filtered between 0.5 and 125 Hz using a fifth-order IIR Butterworth filter. Notch

filteres with a width of 2 Hz were applied to 28, 50, and 100 Hz to suppress any interference caused by the power line noise or any narrow band artefact. After filtering, the recordings were downsampled to 250 Hz.

Next, the data were segmented into slices of varying length, and the G-ESD algorithm [99] was applied to automatically identify bad segments. For the MEG data, recordings were divided into 2.4 s segments, and those with significantly high variance across channels were identified. For the EEG data, recordings were first divided into 0.8 and 1.6 s segments, from which those with significantly high kurtosis across channels were identified. The kurtosis metric was used to remove transient noises that spike sharply. EEG recordings were segmented again into 0.8, 1.6, and 3.2 s slices, and those with significantly high variance across channels were additionally marked. This same G-ESD approach was utilized to detect anomalous channels in the EEG and MEG data, where channels with high variance across time were removed.[3]

Further data denoising was performed by applying a FastICA decomposition [100] to the M/EEG channels, decomposing signals into 64 and 40 components, respectively. Components associated with ocular (i.e., blinks and saccades) and cardiac artefacts were subsequently removed using EOG and ECG recordings. Three subjects lacked EOG or ECG data. For these patients, ICA components were manually marked and removed. Finally, to keep the data dimension consistent across the subjects, any bad channels detected earlier were interpolated from ICA-cleaned data using spherical spline interpolation [101].

Source Reconstruction

To source reconstruct M/EEG data, the surfaces of a scalp, nose, inner skull, and brain were extracted from sMRI data with FSL's BET program [104].[4] The M/EEG data were coregistered to individual structural images via ICP algorithm using the

[3]As in Chapter 2, bad segment and bad channel detection procedures were applied separately to different sensor types for MEG (i.e., magnetometers and gradiometers).

[4]For subjects with low-quality sMRI data, sMRI images of other subjects, matched individually by sex and head size, were used. Three and ten subjects had this problem during MEG and EEG source reconstruction, respectively. More subjects were prone to the problem with EEG, as EEG requires a more complex forward model to account for volume conduction and hence better sMRI quality.

RHINO tool in the OSL package. In this step, the digitized Polhemus head points were matched to scalp surfaces for each subject. To improve the reliability of these head shape points, the head points and fiducials were manually adjusted at the individual level prior to M/EEG coregistration.[5] To construct a head model, a BEM with a single layer of a scalp surface was used for MEG, and a BEM with triple layers of scalp, skull, and cortex surfaces was used for EEG.

Next, the preprocessed sensor data were bandpass filtered between 1-45 Hz with a fifth-order IIR Butterworth filter. These signals were source reconstructed onto an 8 mm isotropic grid using a LCMV beamformer [58, 105]. The rank of a data covariance matrix used to compute the beamformer weights was set to 60 for MEG and 45 for EEG. The vector describing the activity at each source dipole (i.e., voxel) was converted to a scalar by selecting the dipole to be in the direction that maximized the variance explained. Voxels were then parcellated into 38 anatomically defined regions (see Appendix A.1.2). Source reconsturcted signals were obtained by applying PCA to these voxel-wise data. The symmetric multivariate leakage correction [106] was additionally applied to minimize the spurious correlations between neighboring parcels.

Lastly, the signs of voxel-wise data time courses were matched to correct for sign ambiguity of a dipolar source by randomly flipping them and choosing the flips that maximize the Pearson correlation of the data covariance matrices between subjects. Signs were flipped 5,000 times per subject for the M/EEG data, with a maximum number of 20 channels flipped in each iteration. This process was repeated 3 times, and a set of flips that resulted in the highest correlation was saved for use.

3.2.3 Generative Modeling of Resting State Networks

Once the data were preprocessed and source reconstructed, the next step was to identify different brain networks characterizing the resting state and pinpoint time periods during which they activate. To infer the temporal dynamics of RSNs

[5]Specifically, headhshape points more than 15 cm away from the nasion in the vertical axis were identified as outliers and removed. Any points outside LPA and RPA were also removed, except for the nose points.

from the observed data, the source reconstructed MEG and EEG signals were modelled separately using the TDE-HMM and DyNeMo. For each dynamic model, an identical set of hyperparameter configurations was used across the modalities.

Pre-training

Unlike in Chapter 2, the HMM and DyNeMo models in this chapter were built using the pre-trained weights of the HMM and DyNeMo models pre-trained on the full (not age-matched) EEG LEMON and MEG Cam-CAN datasets. For each dataset, a model was pre-trained 10 times, and the one with the lowest free energy was selected for use. We decided to leverage pre-trained models for two reasons. First, the NTAD data could be accessed only on the local computer, given the ethical and safety terms binding the clinical data. With the limited computational power, it was hard to run an entire deep-learning task locally. Second, using the pre-trained model weights allows us to describe the dynamics of the NTAD data with the same RSNs we identified in the previous chapter.

To achieve the latter, we utilized the pre-trained parameter estimates describing each state or mode to infer how the RSNs previously found in LEMON and Cam-CAN describe the NTAD subject data. For the HMM, we loaded the weights of both the transition probability matrix and observation models[6]. Hence, instead of training a new HMM model, we *evaluated* the pre-trained models on the NTAD data, yielding subject-wise state time courses by passing the data through pretrained HMM models. For DyNeMo, we first fixed the weights of the model RNN and observation models obtained from the pre-trained models and then *fine-tuned* the inference RNN on the NTAD data. After training, subject-wise alpha mixing coefficients were inferred from the trained model.

For the full LEMON dataset, hyperparameters used to pre-train the HMM and DyNeMo were identical to those used for the age-matched LEMON data. For the full Cam-CAN dataset, hyperparameters were mostly identical to those used before, except for the training epochs. Epochs for pre-training the HMM and DyNeMo

[6]Here, the weights of the observation models imply the learned parameter estimates of the mode covariances. For more details, please refer to [58].

were reduced to 6 and 15 epochs, respectively, as the full Cam-CAN dataset has much more subjects (n=612) than the age-matched data (n=96). These epochs were selected so that the total number of batches used for learning the age-matched and full Cam-CAN datasets is roughly similar.

Data Preparation

For both the evaluation of an HMM and fine-tuning of a DyNeMo, the NTAD data preparation process followed the same procedure. First, the source reconstructed data were time-delay embedded with 15 lags. To decrease the computational cost, PCA was then applied to reduce the dimensionality down to 80 channels (i.e., components). For both the HMM and DyNeMo, PCA components employed for the pre-training were re-used in order to place the NTAD and LEMON/Cam-CAN data onto a coordinate system defined by the same principal components. Lastly, the transformed data were standardized over time to enhance the optimization process. These prepared data served as the input to the HMM and DyNeMo, which were then shuffled and batched prior to model evaluation or training.

Hyperparameters

As no training is involved in the HMM (i.e., the NTAD data is evaluated by the pre-trained HMM models), no HMM hyperparameters were required. On the other hand, because DyNeMo trains the inference RNN, hyperparameters associated with it had to be defined. First, the number of DyNeMo modes was set to 8 to remain consistent with a pre-trained observation model. The batch size for stochastic VB inference was set to 64, and the input sequence length for segmenting the data was set to 200 samples. DyNeMo was trained for 5 epochs with the learning rate of 5e-4. The inference RNN was built with 64 hidden units with one LSTM layer, and the layer normalization was added to the structure. The temperature of a softmax function was set as a learnable parameter and initialized to 1. Since the model RNN is frozen, KL annealing was turned off, and the annealing factor was fixed to 1 from the beginning. No model initialization was necessary, because pre-trained model weights were loaded in the first place.

Model Runs

Due to the stochastic nature of the parameter optimization process, different model runs may converge to different local optima. To obtain the best possible parameter estimates, DyNeMo were trained three times using the same training dataset on each of the NTAD MEG and EEG data. From these 3 runs, a model with the lowest free energy was selected as the best run. Although the variability across the best runs was not inspected as thoroughly as in Appendix A.5, we validated that the dynamic network features inferred from each run are qualitatively similar and reproducible across runs.

As the order of inferred states or modes is random for each model, it was necessary to align the orders of all runs to establish their correspondence across the datasets and model types. The EEG and MEG HMM states were first aligned manually with eyes. Then, for each modality, the order of DyNeMo modes was matched to its respective state order using the linear sum assignment algorithm [108]. The quality of alignments within and across model types and data modalities was tested with the HMM evaluations and best DyNeMo runs after matching their state/mode orders and is documented in Appendix B.1.3.

3.2.4 Summary Statistics of Network Dynamics

As in Section 2.2.4, four summary metrics—fractional occupancy, mean lifetime, mean interval, and switching rate—were computed from HMM state time courses and DyNeMo mode time courses to quantify the temporal characteristics of the RSNs [57, 58]. HMM state time courses were calculated by applying an argmax operation to the maximum a posteriori probability estimates of the states. DyNeMo mode time courses were computed by fitting a two-component GMM to the alpha mixing coefficients.

3.2.5 Network Analysis

We used power spectra, power maps, and FC maps to analyze the spectral properties and spatial patterns of the static and dynamic networks. FC was measured as

AEC and coherence for the static and dynamic analysis, respectively. All the analyses took place within source space, except for the static power spectra, which were examined in both data spaces (i.e., sensor and source space). The analyses described in this subsection were largely adopted from [58] and conducted using the OSL Dynamics toolbox [109].

To extract these quantities, we employed the same analysis pipeline described in the previous chapter. The only difference was that the confound variable (i.e., site) was regressed out using a GLM when estimating group-level differences in these network features. Hence, the repeating details have been excluded in the following subsections, and we mainly focused on delineating this difference.

General Linear Model (GLM)

To measure the differences in various network features between the AN and AP group, we used a group-level GLM to model the effect of MCI and early-stage AD. Each network feature for individual subjects was fitted to a GLM, wherein a separate GLM was fitted to each feature dimension. This feature dimension was frequency bins for PSDs[7], states or modes for summary statistics, parcels for power maps, and inter-regional connection edges for FC maps. The group-level GLM contained two regressors that model the group means of the AN and AP cohorts separately. In addition, we included site as a covariate to remove any confounding effects introduced by the recording sites.[8] The GLM contained two site regressors, one for Oxford and the other for Cambridge, which were demeaned prior to model fitting. From the fitted GLMs we computed two COPEs, one indicating the *mean group differences* and the other corresponding to the *overall subject mean*. Group-averaged values of each network features could be simply taken from the regression estimates of the fitted GLMs. For the overview of the design matrix

[7]To be more precise, sensor(parcel)-averaged PSDs would have frequency bins as a feature dimension. Before this averaging, PSDs would also have channels as another feature dimension.

[8]Initially, M/EEG device scanner was included as another covariate, but it was subsequently removed because the scanner and site for individual subjects corresponded to each other perfectly, except for just two subjects.

and contrasts we used, readers should refer to Fig. B.2. Below we describe how the GLM was used for each network feature.

Power Spectral Densities (PSDs)

We computed the static PSDs with the Welch's method, after the dataset has been standardized at the individual subject level. The PSD averaged over the entire subjects was obtained by fitting a group-level GLM to PSDs and extracting the overall mean COPEs. To evaluate and compare the PSDs between the AN and AP group, we fitted sensor(parcel)-averaged PSDs to a GLM, from which the mean group differences of these PSDs were extracted.

We noted that the EEG data were recorded with three different montages, each with different number of electrodes. For the sensor-level analysis, therefore, we kept the dimension of PSDs consistent by selecting the electrodes (n=50) common to all montages.

To estimate alpha peak frequency, the PSD of each subject was averaged over channels (i.e., sensors or parcels). From each channel-averaged PSD, the peak frequency with the strongest power between 7 and 14 Hz was selected for each subject. The frequency range to detect a peak frequency was set wider than the defined alpha band (8-13 Hz) to account for the shift in peaks due to subject variability and other cognitive effects. The shift in alpha peak frequencies was then quantified as the mean group differences of these frequencies, attained from a group-level GLM fitted to subject-wise alpha peak frequencies.

For the dynamic analysis, a power spectrum for each state and each subject was calculated using the multi-taper method [78] for the HMM and the GLM method [58] for DyNeMo. As in the static analysis, the PSDs were standardized at the individual subject level in preparation for both approaches. To isolate the dynamic information from these PSDs, the static information shared across all states or modes was separated. As in Chapter 2, the mean spectral densities across all states or modes are called *static mean spectra*, and the dynamic PSDs without static spectral information is called *dynamic state/mode-specific PSDs*. The static mean spectra

and dynamic state/mode-specific PSDs were compared between the AN and AP cohort as described in the static case above. That is, the overall subject mean and mean group differences of these PSDs were computed as COPEs from a fitted GLM.

Power Maps

Next, the power map was estimated by integrating the PSD over defined frequency ranges of 1 to 45 Hz (wide-band), 1 to 4 Hz (delta), 4 to 8 Hz (theta), 8 to 13 Hz (alpha) and 13 to 30 Hz (beta). A static power map for each dataset was attained from its respective static PSD. Similarly, state- and mode-specific power maps were derived from the HMM multi-taper spectra and DyNeMo GLM-based spectra. Like the PSDs, the dynamic information in the power maps was separated by removing the static information common to all RSNs. The mean power across all states or modes was subtracted from the state- or mode-specific power maps at the subject-level. For the HMM, the mean power was weighted by the fractional occupancy of each state. Alternatively, these power maps could also be simply computed from the mean-subtracted PSDs for the HMM and regression coefficients for DyNeMo.

To probe the effect of MCI and early-stage AD in elderly adults, we computed the difference in power maps of AN and AP participants by fitting them to a group-level GLM. The overall mean of power maps across entire subjects were obtained from the same GLM. These power maps and power difference maps were plotted as two-dimensional heatmaps projected onto the surface of the brain to illustrate the power at each region of interest. For a smoother visualization, the power values between parcels were voxel-weighted and interpolated. No thresholding was applied to the visualizations.

Functional Connectivity Maps

The static AEC map was measured by taking the pairwise correlations between the sensor(parcel)-wise amplitude envelopes for each subject.[9] On the other hand, the

[9]In Chapter 2, the AEC method was credited for its consistency in estimating stationary connectivity measures with relatively high test-retest reliability [111]. In line with this observation, M/EEG-derived leakage-corrected AEC has reported high reproducibility in capturing the effects of AD in global FC measures in the alpha (8-13 Hz) and beta (13-30 Hz) bands compared to

state- and mode-specific FC maps were measured by integrating a coherence matrix of each state or mode over defined frequency bands. Like the power maps, the dynamic information in the FC maps was isolated by excluding the static information common to all RSNs. The mean FC across all states or modes, weighted by the fractional occupancy of each state/mode, was subtracted from the state- or mode-specific FC maps at the subject-level. Alternatively, these FC maps could also be simply derived from the mean-subtracted coherences.

The overall mean of FC values and FC group difference were computed by fitting FC values to a group-level GLM and extracting their respective COPEs. The pairwise connections of the FC maps and FC difference maps were displayed as two-dimensional heatmaps or graph networks projected onto the brain. For the graph network, a threshold of 97-th percentile was applied for better visualization, and connection edges with high AEC/coherence values were selected for plotting.

3.2.6 Statistical Analysis

Finally, statistical differences in brain network features between the AN and AP group were examined to probe how MCI and early-stage AD affect the characteristics of RSNs and to evaluate the potential of these features to serve as biomarkers for the prodromal AD. We used nonparameteric permutation tests for all relevant brain network features, using t-statistics as the permuted statistic [112, 113]. For PSDs, a group-level statistical significance was assessed using a two-tailed cluster permutation test. Clusters were formed over frequencies, with a cluster-forming threshold set to 3. For alpha peak frequencies, summary statistics, power maps, and FC maps, a two-tailed max-t permutation test was used to assess a group-level statistical significance.

For both types of permutation test, a metric of interest was first fitted to a group-level GLM as described above. From the fitted GLMs, we computed COPEs (i.e., mean group differences) and their variances, from which t-statistics could be computed. Recall that a GLM had two regressors modelling the group

coherence and phase lag index (PLI) [118, 126]. However, the same studies have also shown PLI to have better reproducibility in the delta (0.5-4 Hz) band in M/EEG and the theta (4-8 Hz) band in MEG.

means of the AN and AP cohort separately. The regressors of group variables were permuted 5,000 and 10,000 times to build a null distribution for a cluster and max-t permutation test, respectively. A threshold was extracted from this distribution to test for a statistical significance.[10]

In the case of DyNeMo models trained on the EEG data, outliers were observed in mean lifetimes and mean intervals. These outliers were excluded from statistical tests on summary statistics and all other EEG DyNeMo analyses as in the previous chapter. Exclusion of outliers was performed without prior knowledge about the subject's group and at the level of an individual model run. The best DyNeMo model run on the EEG data had a total of 14 unique outliers (3 AN and 11 AP participants).

For the cluster and max-t permutation tests, Bonferroni correction was applied to the resulting nonparametric statistics, if cluster and max-t approaches were applied multiple times across data spaces, metrics, or states/modes. This correction was applied within the MEG or EEG data, and tests repeating over modalities were not considered to be a part of the same family.

The demographics of the AN and AP group were mostly compared using the independent t-test after checking the assumptions of normality and equal variance (using the Kolmogorov-Smirnov test and Bartlett's or Levene's test, respectively; Table B.1). Since the MMSE scores of the AN group were non-normal and scores between groups did not have equal variance, a max-t permutation test was applied for the MMSE score specifically. For each metric of the demographics, missing values were excluded from its respective statistical test.

3.2.7 Data and Code Accessibility

For the original NTAD data, the readers should refer to [20]. The preprocessing and source reconstruction of the data were performed using the OSL software [98]. All analyses and data visualizations were performed using the custom codes written in Python (https://github.com/scho97/AnalyzeNTAD), partly adapting the OSL Dynamics software [109] and scripts in [97]. Further requests for prepared

[10] GLM-based permutation tests were implemented using the glmtools software package (https://gitlab.com/ajquinn/glmtools).

data or concerns regarding the codes should be directed to and will be fulfilled by the author (sungjun.cho@psych.ox.ac.uk).

3.3 Results

3.3.1 MCI and early-stage AD are characterized by elevated delta/theta power and reduced beta power

We started by examining the effect of MCI and early-stage AD on the static power spectra (Fig. 3.1). The static PSDs were averaged across sensors or parcels, depending on which data space they were computed in. The group-level cluster permutation tests were then conducted on these spatially averaged PSDs to determine statistical significance along the frequency axis (Fig. 3.2).

Across both modalities, the static power spectra in sensor and source space consistently reported a reduction in the beta spectral power (about 13-20 Hz) for the AP group. In MEG specifically, subjects in the AP group demonstrated an elevation of spectral power in the lower frequency (1-8 Hz) band (Fig. 3.2C, D). Only the sensor space MEG data reported the effects of MCI and early-stage AD on the alpha band (at approximately 11 Hz). Although these statistically significant effects in the lower frequency and alpha bands were unique to MEG, they could at least be observed qualitatively in EEG. In particular, the topographic maps depicting the differences in the alpha peak power, lower frequency band power, and beta band power between the AN and AP group showed comparable spatial distributions of power across the modalities and data spaces (Fig. 3.2, top and bottom). The qualitative group differences were associated with an increased power in the parieto-occipital regions in the lower frequency band for AP subjects, while a decreased power in frontal regions was observed in the beta band. As discussed in Section 2.3.1, we conducted our subsequent analyses of static and dynamic network features exclusively within source space.

Next, shifts in alpha peak frequencies were examined to ascertain whether the slowing of an alpha peak frequency with MCI and early-stage AD is present as

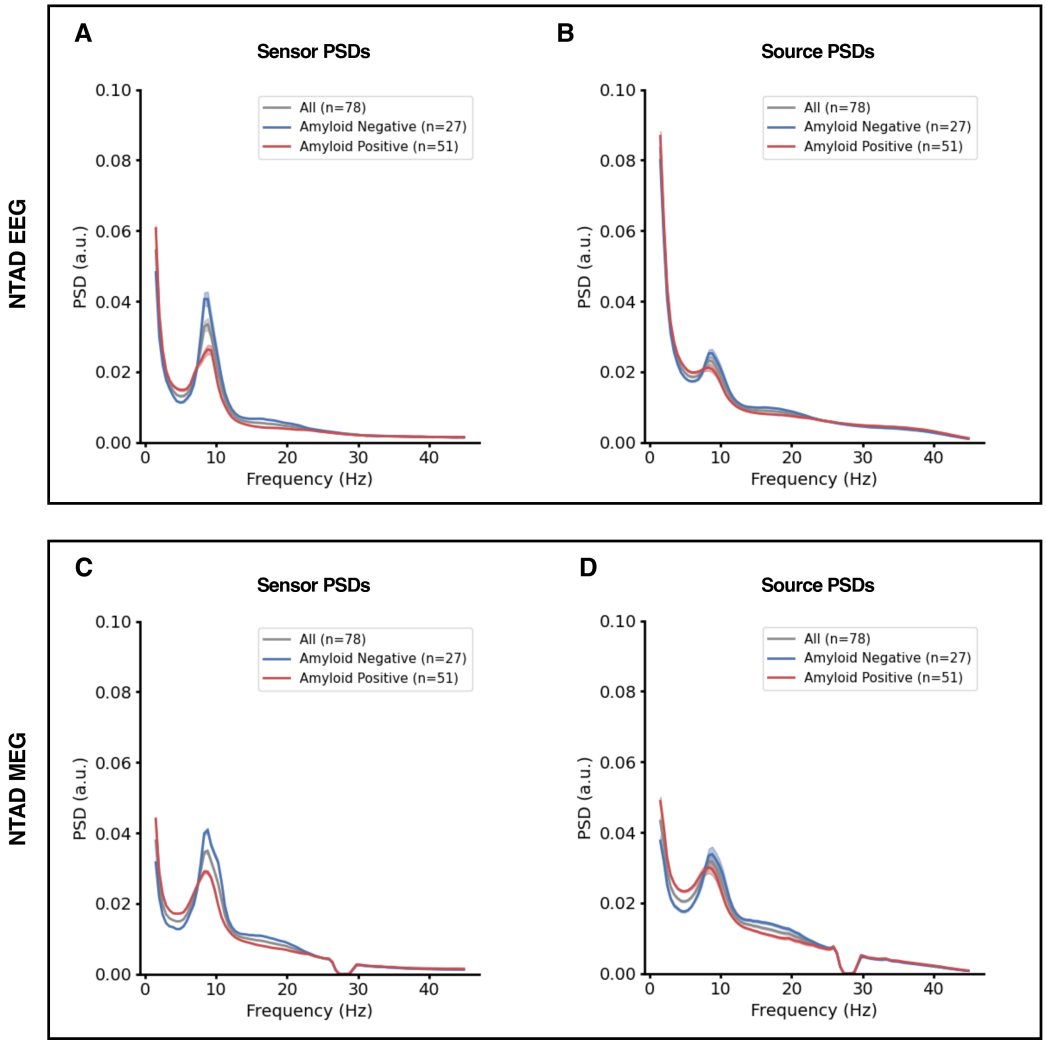

Figure 3.1: Static PSDs in the EEG and MEG data. (A) Sensor space PSDs of the AN (blue), AP (red), and combined (grey) groups are computed from the EEG data. The PSDs are averaged over subjects and sensors, and the standard errors over sensors are shaded in their corresponding colors. **(B)** Source space PSDs of the AN and AP groups and the entire dataset are averaged over subjects and parcels. The PSDs are displayed in the same format as in (A). **(C)** Sensor space PSDs are computed from the MEG data using the same analysis as in (A). **(D)** Source space PSDs are computed from the MEG data using the same analysis as in (B).

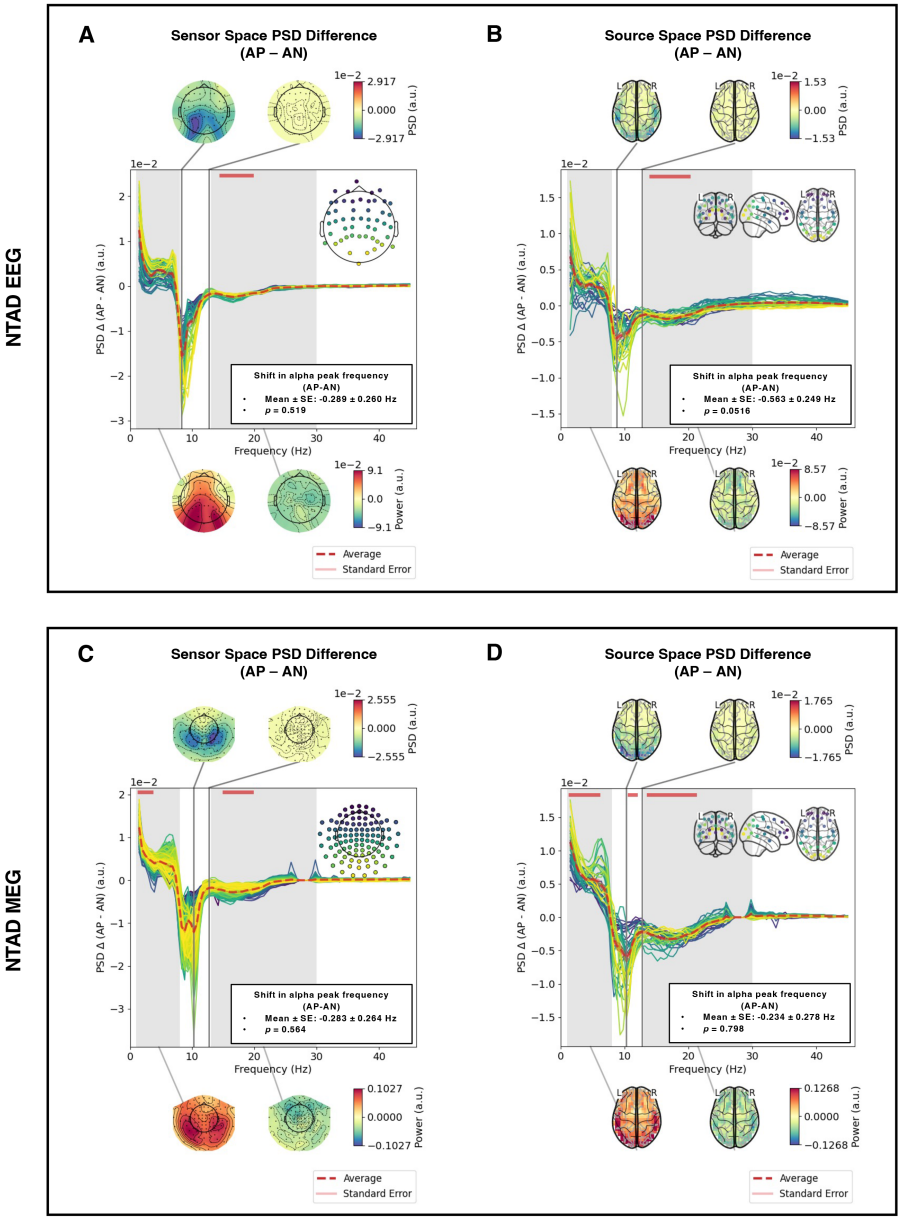

Figure 3.2: Static power spectra in sensor and source space shows frequency-dependent MCI and early-stage AD effects. **(A)** The green lines represent sensor(parcel)-wise PSD differences between the AP and AN group, accompanied by their average (red dotted line) and standard error (pink shade). Frequency ranges with significant PSD differences are identified through cluster permutation tests on sensor(parcel)-averaged PSDs of the two groups (red bars) ($p < 0.05$; Bonferroni-corrected, n=2). Each subplot includes two insets. The top-right inset displays the locations of sensors (parcels) corresponding to each PSD difference line, while the bottom-right inset summarizes an alpha peak frequency shift for each group, along with their statistical differences. SE indicates the standard error of the mean. (***: $p < 0.001$, **: $p < 0.01$, *: $p < 0.05$, n.s.: non-significant) The peak differences in alpha power averaged across subjects are plotted as topographies, displayed at the top. The group-level PSD differences were integrated over the lower (1-8 Hz) and beta (13-30 Hz) frequency bands (grey shades) and depicted as topographies at the bottom. **(B)-(C)** The same analysis as described in (A) is applied to (B) EEG source data, (C) MEG sensor data, and (D) MEG source data. For (C), the topographies only display the measurements of magnetometers.

reported in [117][11]. The distributions of alpha peak frequencies were extracted from the channel-averaged PSDs for each group and compared between groups. However, no shift in alpha peak frequencies was identified to be significant. In the NTAD data, therefore, we concluded that MCI and early-stage AD do not slow down alpha peak frequencies for the AP subjects.

In summary, subjects in the AP group showed reduced beta spectral power in M/EEG and elevated delta and theta power in MEG. This observation was consistent with the previous findings reported in extant literature as surveyed in Introduction. Regarding the alpha peak frequency shift, no significant group difference was found, contrary to previous literature.

3.3.2 Subjects with MCI and early-stage AD show reduced wide-band static power in MEG

Next, we examined the effect of MCI and early-stage AD on the static wide-band (integrated over 1-45 Hz) power maps.[12] Fig. 3.3A, C illustrate the group-level power map differences, with both MEG and EEG showing qualitatively similar spatial patterns. The power maps of AP subjects show reduced wide-band power in frontal, occipital, parietal, and sensorimotor areas across modalities, although the degrees of reduction varied between MEG and EEG. The only noticeable difference between modalities was that EEG showed slight increase of power around central sulcus and temporal lobe in the right hemisphere, while MEG did not.

Statistical analysis of differences between the AN and AP group largely reflected the group-level power map differences mentioned above. We found noticeable effects of MCI and early-stage AD in the frontal, sensorimotor, and parieto-occipital regions, characterized by the reduction in wide-band power (Fig. 3.3D). However, these effects could be observed only in MEG, as no group differences were identified in EEG (Fig. 3.3B). For the same analysis on the static wide-band FC maps, readers should refer to Appendix B.2.2.

[11] Hughes et al. (2019) has reported a significant reduction in the alpha peak frequency from controls (9-10 Hz) to patients with MCI (8-9 Hz).

[12] For group-averaged static wide-band power and FC maps, please refer to Appendix B.2.1.

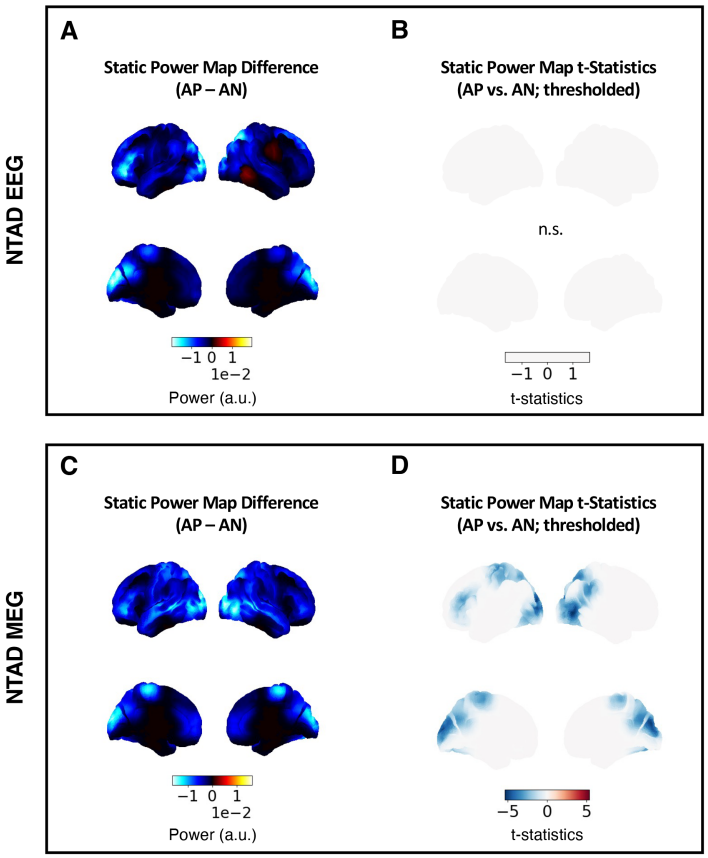

Figure 3.3: Static source-space MEG reveals reduced wide-band (1-45 Hz) power for AP subjects. (A) Brain surface map of the power difference between the AP and AN group for the EEG data. The power map of each group was integrated over the frequency range of 1-45 Hz and averaged across subjects, before calculating group differences. **(B)** The max-t permutation test was applied to wide-band power maps of the participants to examine the difference between the AP and AN group. The parcels with significant t-statistics ($p < 0.05$) are highlighted. **(C)** Similar to (A), the group-level power map difference is shown for the MEG data. **(D)** As in (B), parcels exhibiting significant between-group differences in power are colored on the brain surfaces. Higher power in AP and AN participants are represented by red and blue, respectively. Non-significant results are labeled as n.s.

In summary, our findings illustrate that the wide-band static power in frontal, sensorimotor, and parieto-occipital regions decreases with MCI and early-stage AD. Nevertheless, this group difference could be observed solely in MEG. This result indicates that patients developing AD in its early phase may suffer from attenuation in neural activities in aforesaid brain regions.

3.3.3 Narrow-band static power maps reveal the effects of MCI and early-stage AD across all frequency bands

Following our analysis on static wide-band power maps, we additionally examined the effect of MCI and early-stage AD on the static narrow-band power maps (Fig. 3.4). The group-level power map differences showed increased delta and theta power in the frontal, sensorimotor, and occipital cortices with MCI and early-stage AD, as well as decreased alpha and beta power in the frontal, temporal, and parieto-occipital regions. In general, these differences were comparable across modalities.

For the MEG data, statistical analysis of the between-group differences captured the effects of MCI and early-stage AD across all four frequency bands. We noted significant increases in delta power in the frontal, parietal, and visual cortices and in theta power in the frontal cortex for the AP group (Fig. 3.4B, top). Subjects in this group also demonstrated significant decrease in alpha power in the temporal lobe and in beta power in the frontal, temporal, and parieto-occipital areas (Fig. 3.4B, bottom). No significant MCI and early-stage AD effects were observed for the delta, theta, and beta powers in the EEG data (Fig. 3.4A). Still, AP participants showed reduced alpha power in the frontal and temporal regions, which was roughly analogous to the results seen from MEG.

In summary, patients with MCI and early-stage AD were characterized by increased delta/theta power and decreased alpha/beta power across various cortical regions. This result was in line with previous studies discussed earlier [117–121]. Moreover, the effects of MCI and early-stage AD were much prominent in the MEG data, with EEG showing group differences only in the alpha band.

3.3.4 M/EEG shows pronounced effects of MCI and early-stage AD in network dynamics

We next examined the effect of MCI and early-stage AD on summary metrics of the network dynamics obtained using the HMM. RSNs inferred from the HMM were matched across the modalities to make the comparison between EEG and MEG HMM states congruous (Fig. 3.5). From the power maps averaged over

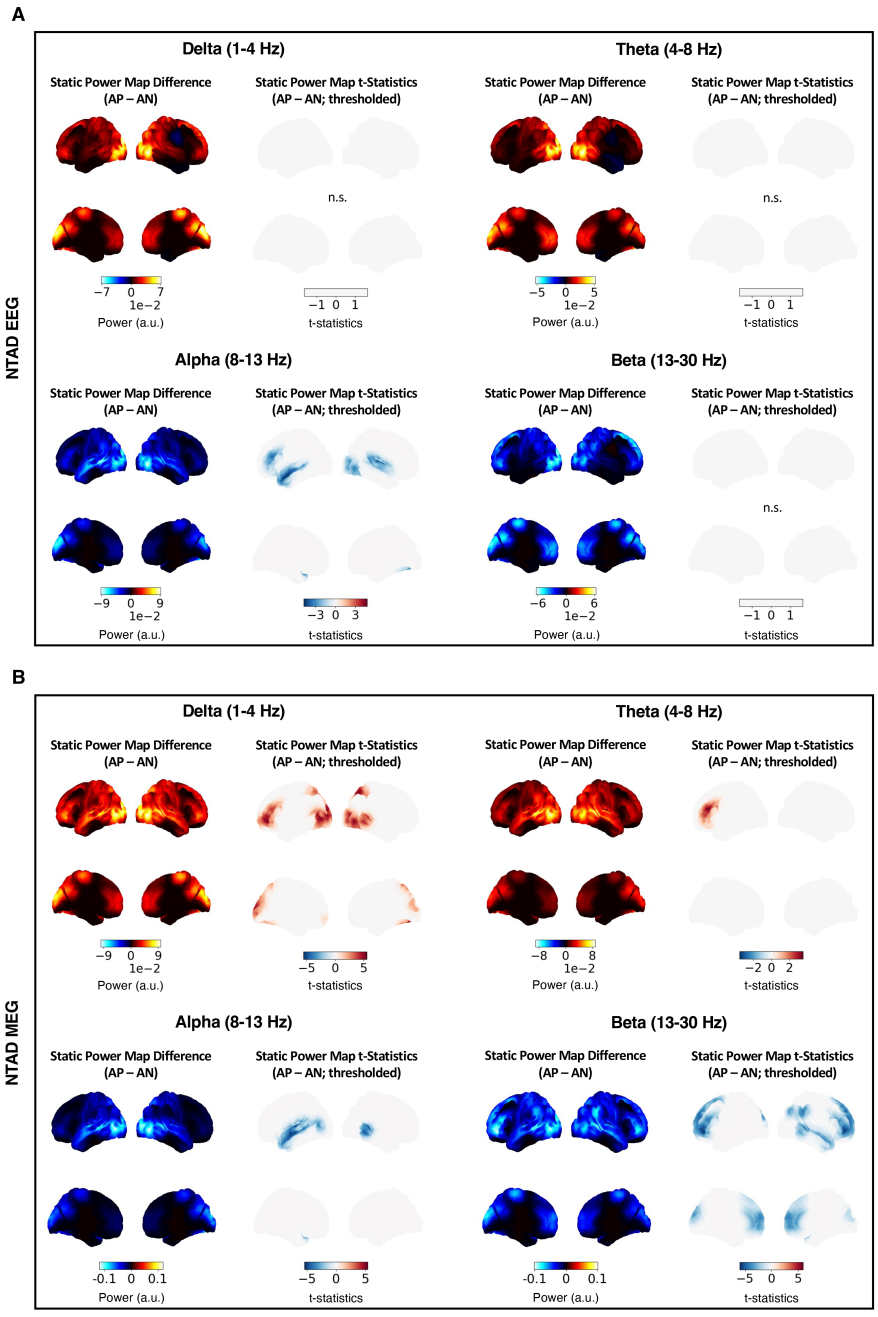

Figure 3.4: Narrow-band static power maps illustrate the effects of MCI and early-stage AD across modalities in source space. (A) A brain surface map of the power difference between the AP and AN group is plotted for each frequency band. The max-t permutation tests ($p < 0.05$; Bonferroni-corrected, n=4) were applied to narrow-band static power maps of the EEG data to highlight the difference between AP and AN participants. The parcels with significant t-statistics are highlighted. The power maps show lateral surfaces at the top and medial surfaces at the bottom. Higher power in AP and AN participants are represented by red and blue, respectively. Non-significant results are labeled as n.s. **(B)** The same analysis as in (A) is conducted for the MEG data.

entire subjects, we discerned EEG States 6 and 7 and MEG State 6 as the states closest to the posterior DMN, while distinguishing M/EEG State 8 as most closely resembling the anterior DMN.

In EEG, State 7 showed statistically significant effects of MCI and early-stage AD in fractional occupancy and mean lifetimes following max-t permutation tests (Fig. 3.6A, B). Both of these summary statistics reported a significant decrease in AP subjects, confirming that the posterior DMN is visited less frequently and for a shorter duration during rest, consistent to previous studies [49, 123]. EEG State 8 demonstrated significant group differences in mean lifetimes, showing increased state lifetime of the anterior DMN for AP subjects.

In MEG, the effects of MCI and early-stage AD became more pronounced. Similar to what was observed in EEG, for AP subjects, State 6 showed reduced fractional occupancy, whereas State 8 showed increased fractional occupancy and switching rate, along with decreased mean interval (Fig. 3.6E-H). This indicates again that the posterior DMN is activated less frequently during rest, while the anterior DMN is activated more frequently. The MCI and early-stage AD effects were observed in States 4 and 5, too. In particular, State 4 appeared to be the RSN representing the suppression of State 6 (posterior DMN). State 5 was associated with increased activity in the occipital cortex as a visual network. These states both illustrated a reduction in mean lifetime with MCI and early-stage AD, with State 4 depicting an additional reduction in fractional occupancy. This potentially implies that the deactivating state of the posterior DMN (State 4) is visited less as well, and further, activity within the visual areas (State 5) is mitigated (see Discussion).

When we replaced the HMM with DyNeMo, the group differences between AN and AP subjects were observed only in MEG (Fig. B.8). MEG Modes 2, 6, and 7 showed significant increase in fractional occupancy and decrease in mean interval for AP subjects. Mode 7 additionally reported a marked increase in switching rate. However, these modes did not resemble the DMNs in contrast to the HMM states above. Mode 2 was one of the sensorimotor networks, while Modes 6 and 7 were RSNs characterized by increased fronto-temporal activity. It is important to note

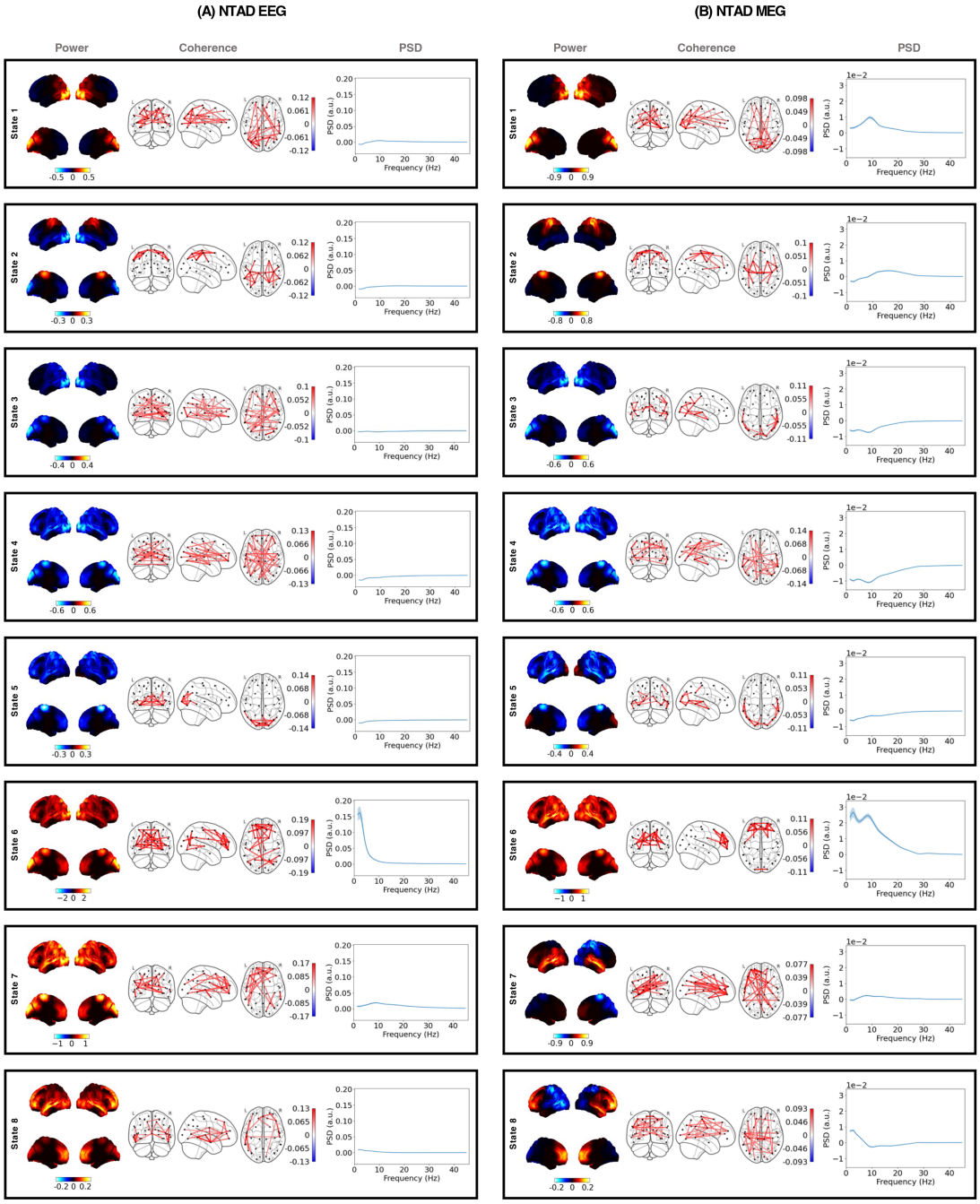

Figure 3.5: HMM resting-state network states inferred from the EEG and MEG datasets. (A) Each box shows the power map (left), FC network (middle), and parcel-averaged PSD (right) of each HMM state derived from EEG for 78 subjects in the NTAD dataset. The power maps show lateral surfaces at the top and medial surfaces at the bottom. The FC networks illustrate connections with the top 3% coherence values. The shaded areas of the PSDs represent the standard error of the mean. The power maps, FC networks, and PSDs are visualized relative to their average across all states. **(B)** The plots follow the same format as (A), showing the RSNs derived from MEG for 78 subjects in the NTAD dataset.

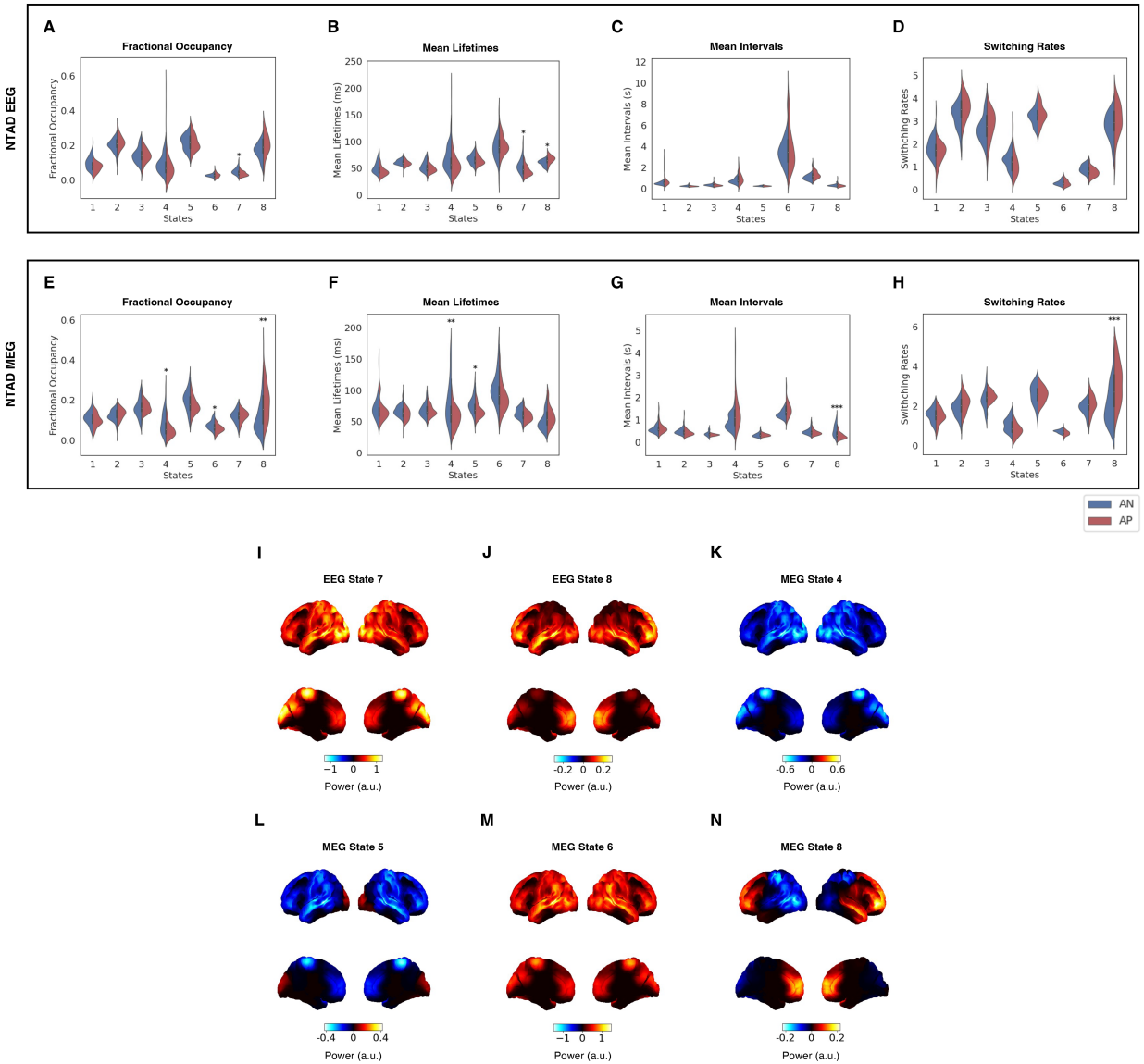

Figure 3.6: Dynamic effects of MCI & early-stage AD in HMM summary statistics are associated with the DMNs. Summary statistics of the state time courses inferred from the EEG data – **(A)** fractional occupancies, **(B)** mean state activation lifetimes, **(C)** mean state activation intervals, and **(D)** state switching rates – are plotted as distributions over the grouped subjects. **(E)-(H)** Same plots for the MEG data are presented. The states showing significant between-group differences are marked by asterisks. Statistical significance was determined using max-t permutation tests for each dataset, Bonferroni-corrected by the number of metrics (n=4). (***: $p < 0.001$, **: $p < 0.01$, *: $p < 0.05$, n.s.: non-significant) **(I-J)** Wide-band (1-45 Hz) power maps of two EEG states, which show significant between-group differences in summary statistics, are illustrated. These power maps are averaged over the entire dataset. **(K-N)** Likewise, wide-band power maps of four MEG states are depicted in the same style.

that while this does not agree with previous findings on the DMN, past studies were conducted using only the HMM. Therefore, DyNeMo, with more detailed descriptions of co-activating modes, may have revealed previously unknown effects of MCI and early-stage AD, potentially offering a novel biomarker candidate.

In summary, the M/EEG data demonstrated pronounced effects of MCI and early-stage AD in summary metrics of the DMNs with the HMM. On the other hand, these effects were seen only in MEG with DyNeMo, and they were associated with sensorimotor and fronto-temopral networks. This result thus confirms findings from past research using the HMM and proposes a putatively novel biomarker candidate for identifying the earliest changes in the brain induced by AD. However, the practical value of this candidate as a biomarker should be further reinforced through studies that substantiate its clinical effectiveness and its resilience to individual variability.

3.3.5 Dynamic spectral effects of MCI and early-stage AD are associated with specific states/modes

Expanding on the static spectral analysis, we examined the effect of MCI and early-stage AD on the state-specific PSDs found using the HMM. We computed the static mean across all HMM states and subtracted it from the state-specific PSDs, thereby isolating the static and dynamic information from one another. Reassuringly, the static mean spectra reflected the effects of MCI and early-stage AD previously noted in the static PSDs for both EEG and MEG, pinpointing roughly 11-20 Hz and 10-23 Hz to have significant group differences, respecitvely (Fig. 3.7A, C; Fig.3.2).[13] As in Section 2.3.4, this also highlights how any results we find on the residual dynamics can be considered as distinct form the static effects we have already seen.

For both modalities, a group-level statistical assessment of dynamic state-specific PSDs showed significant effects of MCI and early-stage AD in the alpha (8-13 Hz) and beta (13-23 Hz) bands. These frequencies were largely analogous to those identified from the static mean spectra as having significant group differences (Fig.

[13]Although the frequency ranges identified here include high alpha frequencies compared to the frequency range of 13-20 Hz found in the static analysis, we reocgnized these effects to be comparable. Note that we used the Welch's method in the static analysis but the multitaper method here for PSD computation. This may yield some differences.

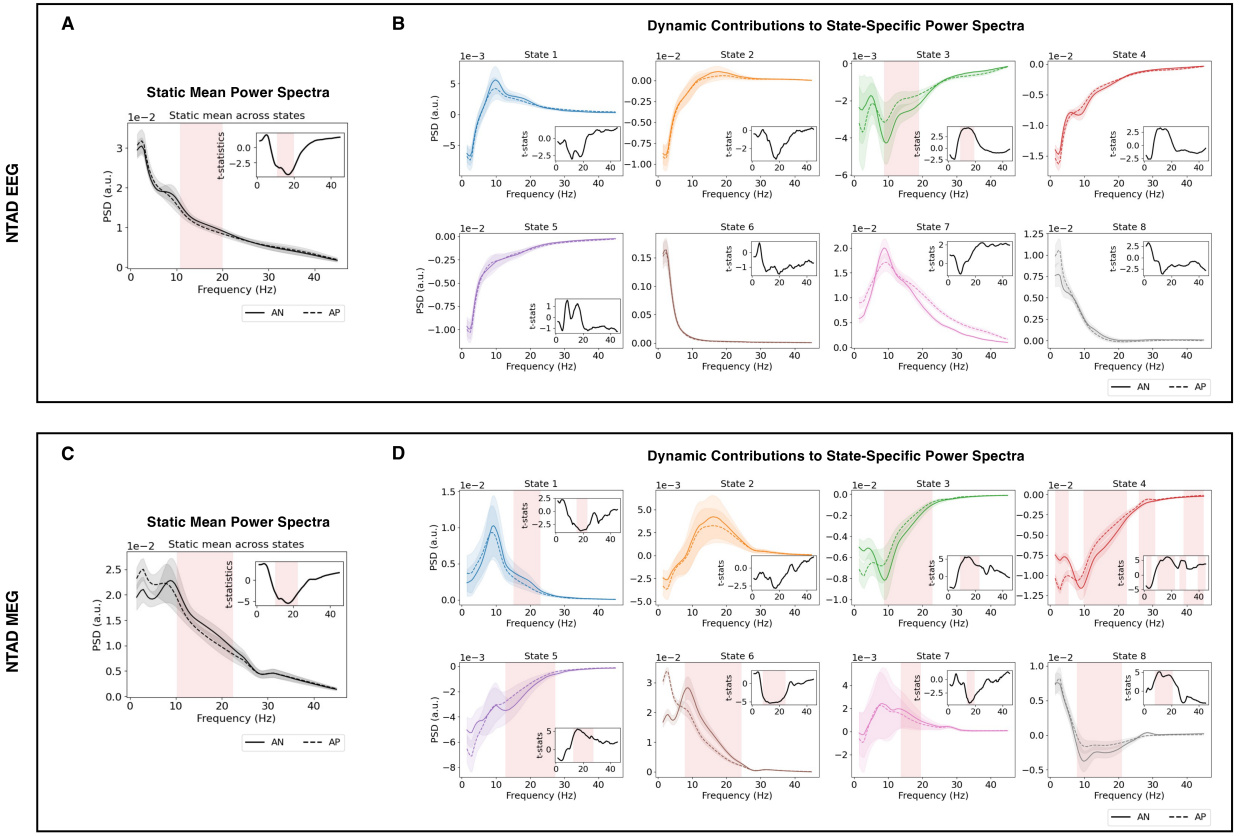

Figure 3.7: Effects of MCI & early-stage AD in spectral powers are observed across multiple frequency bands when dynamic information is isolated. **(A)** The mean PSD across all states is obtained from the EEG data for AN (solid) and AP (dotted) participants and averaged over the subjects and parcels. A cluster permutation test is conducted on the parcel-averaged static mean PSD to detect static effects of MCI and early-stage AD. Frequencies exhibiting statistical significance ($p < 0.05$; Bonferroni-corrected, n=9) are highlighted in red. **(B)** The state-specific PSDs of the EEG data are averaged across each group and parcels after the mean across states is subtracted at the subject level. These group-averaged, mean-subtracted PSDs of AN (solid) and AP (dotted) participants are illustrated for each HMM state. Cluster permutation tests are conducted on parcel-averaged, mean-subtracted PSDs of each state to detect dynamic effects of MCI and early-stage AD. Frequencies exhibiting statistical significance ($p < 0.05$; Bonferroni-corrected, n=9) are highlighted in red. **(C)** The same analysis as in (A) is performed on the MEG data. **(D)** The same analysis as in (B) is performed on the MEG data. For all plots, the inset portrays t-statistics contrasting its corresponding PSDs of the AN and AP group.

3.7B, D). One exception was MEG State 4, which additionally captured MCI and early-stage AD effects in the lower frequency (2-5 Hz), high beta (26-31 Hz), and gamma (39-45 Hz) ranges. Interestingly, MEG delineated more dynamic states with effects of MCI and early-stage AD than EEG, marking every state except State 2 to have significant group differences compared to a single state (State 3) in EEG.

Next, we repeated cluster permutation tests on mode-specific regression-based PSDs, inferred from DyNeMo, again after separating the static and dynamic spectral components. For both EEG and MEG, the corresponding static mean spectra across all modes consistently reflected comparable effects of MCI and early-stage AD that were previously observed in the static PSD analysis, pinpointing roughly 14-19 Hz and 11-21 Hz to have significant group differences, respectively (Fig. B.9A, C). As in the case of HMM, MEG delineated more dynamic modes with MCI and early-stage AD effects than EEG, marking three modes (Modes 1, 6, 7) to have significant group differences compared to one mode (Mode 3) in EEG. Dynamic mode-specific PSDs of MEG revealed frequency ranges with significant group differences that resemble those detected from its respective static mean spectrum. EEG Mode 3, however, showed group differences in the alpha (8-11 Hz) band, which were undetectable in its respective static mean spectrum.

In summary, regardless of which dynamic model we use, M/EEG demonstrated a unique set of RSNs exhibiting dynamic effects of MCI and early-stage AD. Effects in these RSNs were in general akin to what we saw in the static analysis, suggesting that similar effects can be attributed to a set of specific states and modes activating at specific time points.

3.3.6 Dynamic effects of MCI and early-stage AD in wide-band power are observed within specific RSNs in MEG

To elaborate on our findings on the static power, we lastly examined the effect of MCI and early-stage AD on the state-specific power maps found using the HMM.[14] As before, to distinguish static from dynamic effects, the static mean

[14]For the power and FC maps of HMM states and DyNeMo modes averaged across all subjects, refer to Fig. 3.5 and Fig. B.7. These maps illustrate the degree of alignment between states and

power maps obtained by averaging across all HMM states were removed from their respective state-specific power maps.

Static mean power map differences in MEG (i.e., unthresholded t-statistics) between the AP and AN cohort roughly mirrored spatial patterns that were previously found in the static analysis (Fig. 3.8, top left; Fig. 3.3C). In the MEG data, significant effects of MCI and early-stage AD were observed in the static mean power map and power map of State 8 (Fig. 3.8). Group differences in the static mean power crudely corresponded to the findings from the previous static analysis (c.f., Fig. 3.3D). Specifically, reduced power was observed in the frontal and sensorimotor areas for the AP participants, although reduced activation in the bilateral temporal lobes was highlighted additionally instead of the parieto-occipital regions in the static analysis. Conversely, MEG State 8 (anterior DMN) showed significatnly increased power in the temporal areas for the AP subjects. Note that no effect of MCI and early-stage AD was reported in the EEG data. For the same analysis on the dynamic state-specific FC maps, readers should refer to Appendix B.3.4.

The identical approach was repeated on the static mean and dynamic mode-specific power maps inferred by DyNeMo. As with the HMM, static mean power map differences between the AP and AN cohort were similar to static power map differences in Figure 3.3C. In the MEG data, a group-level statistical analysis unveiled significantly reduced power in the frontal and occipital areas in the static mean power maps, while also reporting reduced power in the sensorimotor, parietal, and temporal areas for Modes 4, 6, and 7, respectively (Fig. B.10). As in the case of the HMM, no effect of MCI and early-stage AD was found in EEG. With both the HMM and DyNeMo, we noticed that the RSNs identified to have significant group differences in wide-band power coincide with those identified to have significant effects in summary metrics.

Finally, we explored the relationship between power and coherence for each dynamic brain network. For each modality and group, we plotted mean-subtracted wide-band power and coherence values across states/modes and ROIs (Fig. B.12).

modes, providing an additional insights on our comparison of state- and mode-specific power and FC maps.

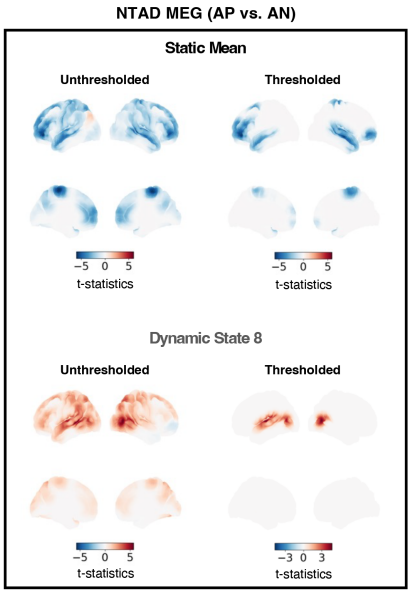

Figure 3.8: Dynamic MEG state reveals increased wide-band power in the temporal regions for AP subjects. The result of statistical analysis conducted on the wide-band (1-45 Hz) static mean and dynamic state-specific power maps is presented here. Only the power maps with significant effects of MCI and early-stage AD are plotted. Power maps on the left display t-statistics between groups, and the parcels with significant t-values are colored on the right. Max-t permutation tests were used to evaluate statistical significance. Parcels are marked significant if $p < 0.05$ (Bonferroni-corrected, n=9).

HMM-derived power and coherence measures demonstrated U-shaped joint distributions for both MEG and EEG. Qualitatively speaking, coherence in State 7 (posterior DMN) increased for AP subjects in the EEG data. In the MEG data, coherence of States 4 and 6 (posterior DMN) strengthened, while that of State 8 (anterior DMN) mitigated.[15] With DyNeMo, distributions of power and coherence demonstrated vastly distinct patterns across modalities. Qualitative group differences were clearer in MEG, where Mode 1 (posterior DMN) showed decrease in coherence, and Modes 3 and 8 (anterior DMNs) showed increase in coherence for AP subjects. In both modalities, it was hard to detect any qualitative group differences in power values.

In summary, dynamic effects of MCI and early-stage AD in wide-band power maps could be observed across the state and modes in the MEG data. Subjects in the AP group were characterized by increased power in the anterior DMN with the HMM and reduced power in the sensorimotor and fronto-temporal RSNs

[15]Following this observation, significant group differences in wide-band FC (i.e., coherence) maps were reported in MEG States 6 and 8. For more details, please refer to Fig. B.11.

with DyNeMo. From the joint distributions of power and coherence, we could further observe qualitative group differences in RSN-specific coherence across DMN-like states and modes.

3.4 Discussion

3.4.1 Conclusion

In this chapter, we demonstrated that the previously known biomarkers identified from M/EEG are reproducible in the NTAD dataset. We then highlighted a set of dynamic brain network features as potentially novel biomarkers for AD, although the clinical significance of these features remains to be confirmed. While effects of MCI and early-stage AD in M/EEG RSNs were deemed subtle and hard to capture in the past [123], our identification of dynamic effects in the NTAD data hints that they can still be detected, suggesting that resting-state M/EEG can promote early detection of AD and enhance our understanding of disease progression in the future.

Reproducibility of M/EEG-derived AD biomarkers

The first objective of this chapter was to ascertain the reproducibility of M/EEG biomarkers reported in previous literature. In our analysis of static PSDs and power maps, significant increase in delta/theta power and significant decrease in alpha/beta power could be observed across the brain globally, encompassing all of the frontal, occipital, temporal, and parietal cortices, consistent to [117–121] (Fig. 3.2; Fig. 3.4). We also observed diminished FC in the alpha and beta bands from group-level statistical analysis of the static FC maps, as indicated by [117, 118, 122] (Fig. B.6). However, the effect size of group FC differences was small in EEG, and these effects were not spatially localized in MEG.

Furthermore, our analysis on summary metrics of HMM network dynamics confirmed that the posterior DMN activates less frequently and for shorter duration for subjects in the AP group. While previous studies [49, 123] have reported this effect in AD, we found the same effect in MCI and early-stage AD. Notably, EEG State 7 (posterior DMN) showed significant decrease in mean lifetime for

AP subjects (about 50 ms), which was even shorter than what was observed in [49] with MEG (150 ms).

Based on the results above, we could confidently affirm that the MCI- and AD-related biomarkers, extracted from resting-state M/EEG, can be robustly reproduced in the NTAD dataset. This outcome is promising, lending reliability to our use of M/EEG RSN features as one of the AD biomarkers. Nonetheless, determining their clinical meaningfulness and evaluating their standalone efficacy as a biomarker without any auxiliary tests necessitate further examination and validation.

Dynamic brain network features as a novel biomarker candidate

The second objective of this chapter focused on identifying potentially new biomarkers for prodromal, early-stage AD. While our static analysis did not unveil novel biomarkers, several candidates emerged from dynamic brain network features. First, in summary metrics of RSNs, we discovered that the HMM-derived anterior DMN exhibits an increased state lifetime in EEG and a higher switching rate and fractional occupancy with a decreased state interval in MEG (Fig. 3.6). The anterior DMN (M/EEG State 8) is known to be associated with self-referential mental thoughts, whereas the posterior DMN (EEG States 6, 7; MEG State 6) is known to be involved in episodic memory retrieval, mental scene construction, and future-oriented thoughts [127]. Adding onto our observations on the posterior DMN above, it may be interpreted that AP subjects tend to access the anterior DMN more frequently, immersing themselves in self-related thoughts, while their capacity for memory retrieval and scene construction declines. Decline in scene construction capacity may also be related to a reduction in mean lifetime in the visual network (MEG State 5) (Fig. 3.6L).

We also found that summary metrics, inferred by DyNeMo, indicate increased fractional occupancy and decreased mode interval in the sensorimotor and fronto-temporal networks, alongside an elevated switching rate in one of the fronto-temporal networks (i.e., MEG State 7). From a previous chapter, we saw that the HMM and DyNeMo could yield different results, with DyNeMo providing more

pronounced dynamic age effects than the HMM as a linear mixture model. It is plausible that observing the dynamics of co-activating modes allows DyNeMo to detect more nuanced dynamic effects of MCI and early-stage AD. The group differences we observed in summary statistics of DyNeMo modes suggest that AP subjects experience more frequent visit to the sensorimotor and fronto-temporal networks. This implies that MCI and early-stage AD are potentially related to increased activation of these RSNs.

Secondly, in our dynamic analysis of wide-band power maps, we discovered that the HMM-derived anterior DMN demonstrates increased power in the bilateral temporal lobes when measured with MEG. Utilizing DyNeMo, MEG Modes 4, 6, and 7 displayed diminished power in the sensorimotor, parietal, and temporal regions, respectively. Interpreting this result in the context of previous findings proposes that while the anterior DMN sees more frequent visits bolstered by its power increase, frequent visits to the sensorimotor and fronto-temporal networks may have been necessitated due to their reduced activity.

Throughout all dynamic analyses, we observed that MEG appears more adept than EEG at capturing the effects of MCI and early-stage AD. However, it is crucial to acknowledge that we cannot definitively state that MEG outperforms EEG in detecting MCI/early-stage AD effects. As mentioned in the previous chapter, MEG employs significantly more sensors than EEG (306 MEG sensors $>$ 60-70 electrodes). Therefore, when subjected to source space analysis after implementing spatial orthogonalization (i.e., leakage correction), EEG is affected by more smoothing over fewer sensors with neighboring correlations, enhancing uncertainty in region-specificity. Further examinations, both at the sensor level and in the source space without orthogonalization, are required to draw conclusive insights on modality-dependent performance.

Based on our findings discussed thus far, we are optimistic that the dynamic network analysis will be able to pave a new path towards identifying a biomarker for AD from M/EEG RSNs. We presume future investigations into dynamic power and FC in narrow bands to be beneficial. Furthermore, our analysis of RSN-specific

PSDs revealed that dynamic effects in state/mode-specific power spectra parallel static effects. However, the states or modes housing this effect differed across modalities and model types. Hence, we believe subsequent studies that explore RSN activation timing could potentially unveil how each RSN may convey similar spectral effects at varied time intervals.

3.4.2 Limitations

The dataset and methodology utilized in this chapter come with certain limitations and caveats. Firstly, it is imperative to acknowledge that the sample size used here is small, consisting of 27 AN subjects and 51 AP subjects, with subject losses resulting from participant attrition, missing data, and poor data quality, particularly among AP subjects, given that the NTAD study originally comprised 30 controls and 100 patients.

Secondly, we only set site as covariates to be regressed out, excluding other potential confounds like age and sex. This decision was made out of caution, recognizing that age and sex could explain variability in our effect of interest and also correlate with it. Thus, we sought to run our analysis pipeline on our data without regressing them out, deferring this step for future studies.

Thirdly, the dynamics of RSNs were inferred by utilizing pre-trained HMM and DyNeMo weights dervied from the LEMON and Cam-CAN datasets. Consequently, the RSNs deduced from the NTAD dataset may partly biased to the characteristics of those identified within LEMON and Cam-CAN. A more comprehensive validation of the pre-training approach is mandated, which can be achieved by contrasting these results with those extracted from the models trained on the NTAD dataset without any pre-trained weights.

Lastly, subjects with MCI and early-stage AD were combined into a single group. For the purpose of this thesis, we assumed that the effects of MCI and early-stage AD together could be distinguishable from the controls. Also, we had to take into account that the AP group has an insufficient sample size to divide the group further. Nonetheless, it is pertinent to note that progression from

MCI to AD is not guaranteed, and therefore, the MCI-related effects cannot be directly regarded as the effects of prodromal AD. Future research might benefit from evaluating them as distinct groups.

In addition to the limitations above, it is crucial to acknowledge that while the dynamic brain network features identified in this study are promising biomarker candidates, their clinical utility must be thoroughly established before they can be considered a new standard for effective diagnosis. Despite their statistical significance, the statistical power of these findings might be inadequate when confronted with the heterogeneity of the disease and the variability around effect sizes among subjects is high.

4
Conclusion

Contents

This thesis delves into two crucial research domains in neuropsychiatry: healthy aging and Alzheimer's disease. The chapter dedicated to healthy aging elucidates the distinctions between resting-state MEG and EEG in capturing age-related effects and validates the methodologies employed throughout the thesis. The key contributions of Chapter 2 are summarized as follows:

1. MEG and EEG reveal comparable age effects in both sensor and source space static PSDs, as well as in source space static narrow-band power maps.

2. In the source space, MEG exhibited higher sensitivity to age effects than EEG in general, though this does not necessarily imply the overall superiority of MEG.

3. We confirmed that dynamic analysis methods, specifically the TDE-HMM and DyNeMo, developed initially for MEG can be reliably applied to EEG to infer transient resting-state network dynamics.

4. The previously documented effects of healthy aging on the alpha and beta power were successfully replicated. Specifically, the decrease in alpha power in the occipital cortex observed in MEG and the increase in beta power in the sensorimotor and frontal regions noted in M/EEG with aging were confirmed.

Informed by these findings, the chapter on Alzheimer's disease assessed the viability of using M/EEG-derived RSN features as emerging biomarkers for MCI and early-stage AD, while also reaffirming the reproducibility of previously identified AD-related biomarkers.The important takeaways from Chapter 3 are encapsulated as follows:

1. The effects of MCI and AD in static brain network features and the HMM-derived posterior DMN are successfully reproduced in the NTAD dataset.

2. Dynamic effects of MCI and early-stage AD, discerned from DyNeMo-inferred summary statistics and wide-band power maps, are demonstrated to potentially serve as AD biomarkers in its initial phase.

3. Source space MEG captures the effects of MCI and early-stage AD in M/EEG-derived static and dynamic RSN features better than EEG, suggesting that MEG produces more reliable biomarkers given its superior spatial resolution arising from a larger number of sensors and subsequent spatial orthogonalization.

4.1 Future Research Directions

The prospective directions for augmenting our present study and addressing open questions in the field can traverse various avenues. Some of them are delineated below. For all potential topics, it is important to ensure careful structuring of study designs and large sample sizes to obviate the risk of underpowered statistical analyses. In the following subsections, we additionally consider how these topics might confront the principal reasons behind the underperformance of present biomarkers that were discussed earlier in Chapter 1.

Trajectory of Disease Progression

Our study of the NTAD data found a set of potential biomarkers derived from dynamic RSN features, inferred from resting-state M/EEG data measured from the participants at their fist visit. Given that the NTAD data involves longitudinal measurements at subsequent 12 and 24-month intervals, future research endeavors might aim to identify a biomarker set that can predict disease progression and ensuing trajectories. An exploration into whether such biomarkers explain variations in cognitive degeneration over time can be helpful. By understanding the earliest changes in the brain instigated by AD and learning how they develop, pathways toward novel treatments might be illuminated. Moreover, a comparative analysis between biomarkers from initial and advanced stages of AD may reveal whether their predictive capacities diverge and, if so, which specific biomarkers elucidate each respective AD stage. Comparing disparate AD populations, as opposed to the conventional framework which juxtaposes healthy controls with patients (often symptomatic having a disease at its later stage), might attenuate uncertainties inherent to large effect sizes found under such framework.

Predictive Efficacy of Combined M/EEG Features

We suspect that the predictive efficacy of the biomarkers identified in Chapter 3 can be measured by implementing a classification task, which might help defining their clinical meaningfulness in quantifiable metrics. It would be interesting to see how accurately biomarkers of each modality can detect AD in its early stage. Further exploration into the predictive power of combined M/EEG-derived resting-state biomarkers may shed light on their potential to function as complementary data modalities in precisely diagnosing the prodromal AD.

Comparison to Other AD Biomarkers

As knowledge concerning M/EEG-derived resting-state biomarkers for MCI and early-stage AD grows, it becomes plausible to contrast their sensitivity to disease progression against the biomarkers identified in alternative modalities — such

as MRI, cognitive assessments, and other physiological and genetic data sources (e.g., from blood and CSF neuropeptides). Should one modality manifest superior performance, dissecting the underlying causes of this superiority can inform applicative biomarker studies in health and medical sciences, thereby assisting in sculpting a "gold standard" definition for AD.

Individual Differences in Early-stage AD

Finally, the pervasive issue of individual heterogeneity in the onset and progression of AD cannot be overlooked. The development of methodologies to quantify individual subject variability in modeling RSNs — to elucidate subject-dependent cognitive declines, symptoms, and biomarker sensitivity — merits attention. A division between individuals with MCI who did not advance to AD and those who did, coupled with an analysis of early-stage AD, may illuminate their distinctive characteristics and trajectories, providing a further nuanced understanding of the disease.

4.2 Closing Remarks

The lack of clinically meaningful biomarkers remains one of the most significant challenges confronting neuropsychiatry research, affecting populations worldwide. For biomarkers to be clinically effective, they must exhibit robustness against subject variability, recording sites, impacted races, and various other sources of variances. Studies on biomarkers can facilitate the sub-categorization of numerous neuropsychiatric disorders including AD and provide insights into their underlying biological mechanisms. This thesis aspires to lay a foundational step towards a future research, continuing the pursuit of identifying neurophysiologically solid and consistent biomarkers, eventually contributing to the development of an objective, mechanism-based prognosis and diagnosis for the neuropsychiatric disorders.

Appendices

A

Supplementary Materials for Chapter 2

A.1 Data & Methods

A.1.1 Datasets

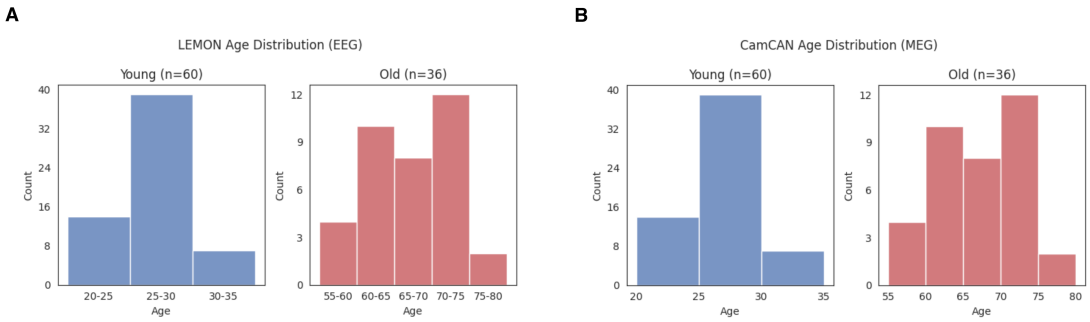

Figure A.1: Age distributions of participants in EEG LEMON and MEG Cam-CAN datasets. (A) Histograms depict the distribution of ages for the young (blue) and old (red) group in the EEG data. **(B)** Similarly, histograms show the age distribution for the young and old group in the MEG data. Both datasets have a sample size of 60 young and 36 old participants. To ensure comparable sample sizes between the LEMON and CamCAN datasets, a subsample of participants was taken for each age group from each dataset.

A.1.2 Source Parcellation Index

Location	Hemisphere	ROI Index
Occipital lobe (visual cortex)	L	1, 3, 13, 15, 25
	R	2, 4, 14, 16, 26
Parietal lobe + motor cortex	L	5
	R	6
Temporal lobe	L	7, 17, 33
	R	8, 18, 34
Motor cortex	L	9, 19, 27
	R	10, 20, 28
Parietal lobe	L	11, 21
	R	12, 22
Frontal lobe	L	23,29, 31, 35
	R	24, 30, 32, 36
Medial posterior cingulate cortex	Both	37
Anterior cingulate cortex	Both	38

Table A.1: Index of parcellation ROIs. The ROI numbers in the source parcellation are indexed into four main lobes and multiple canonical cortical regions. The odd numbers designate brain areas of the left hemisphere, while the even numbers mark those in the right hemisphere, except for the cingulate cortices (i.e., regions 37 and 38). L: left hemisphere, R: right hemisphere.

A.1.3 HMM and DyNeMo Model Training

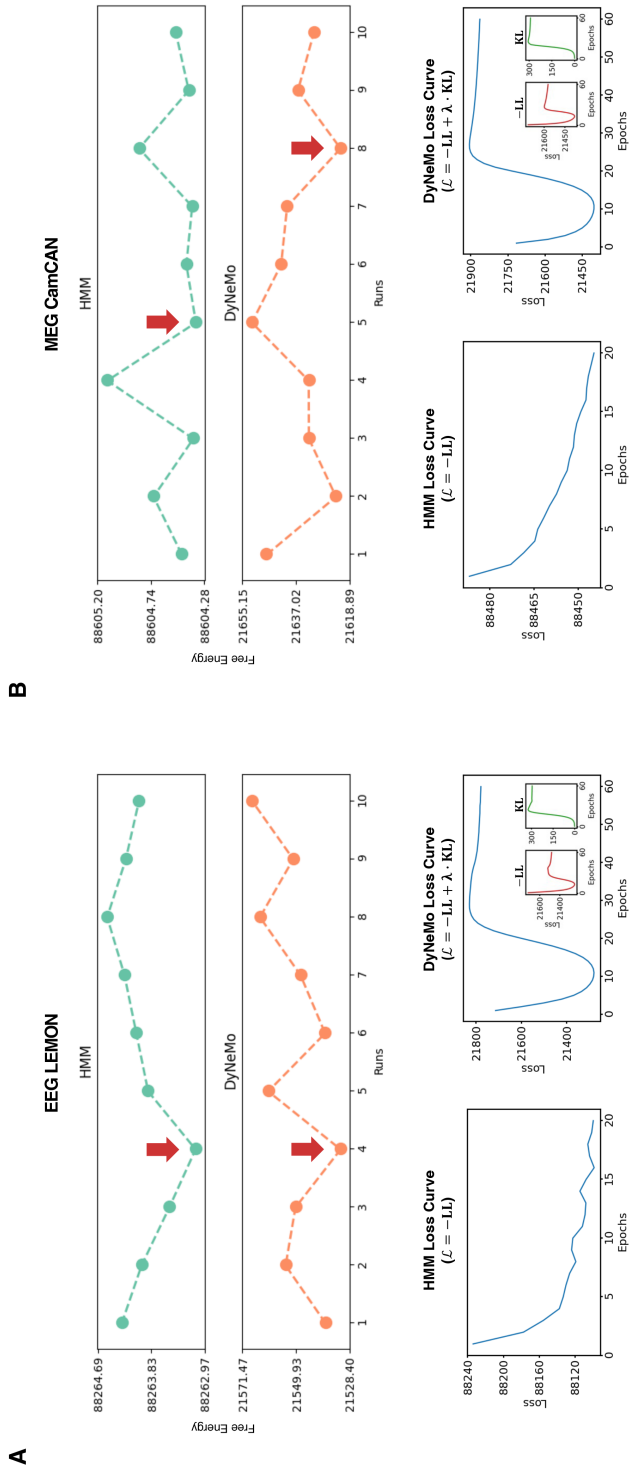

Figure A.2: Free energy and training losses of HMM and DyNeMo models on EEG and MEG datasets. **(A)** The variational free energies of the 10 best HMM and DyNeMo models trained on the EEG LEMON dataset are displayed on the top. The optimal run with the minimum free energy is indicated by a red arrow for each model, and the training loss curves of these runs are plotted at the bottom. The loss of HMM is represented by the negative log likelihood, whereas the loss of DyNeMo is a sum of the negative log likelihood and scaled Kullback-Leibler divergence. Each loss component of DyNeMo is presented in the inset. **(B)** The same analysis as in (A) is performed on the MEG Cam-CAN dataset.

A.1.4 Matching State and Mode Orders

After the orders of states and modes from the four optimal runs were matched, the quality of their alignment was assessed based on the correlations between their state and mode time courses. It was shown that the cross-modal matching (Fig. A.3A-B) has a lower performance than cross-model matching (Fig. A.3C-D) in general, as indicated by higher diagonal values of the correlation matrices between HMM state time courses and DyNeMo mode mixing coefficients. Also, note that although Mode 7 of EEG and MEG both show high correlations with most of the states, they were not a mode activating at the background but a mode with high temporal activities.

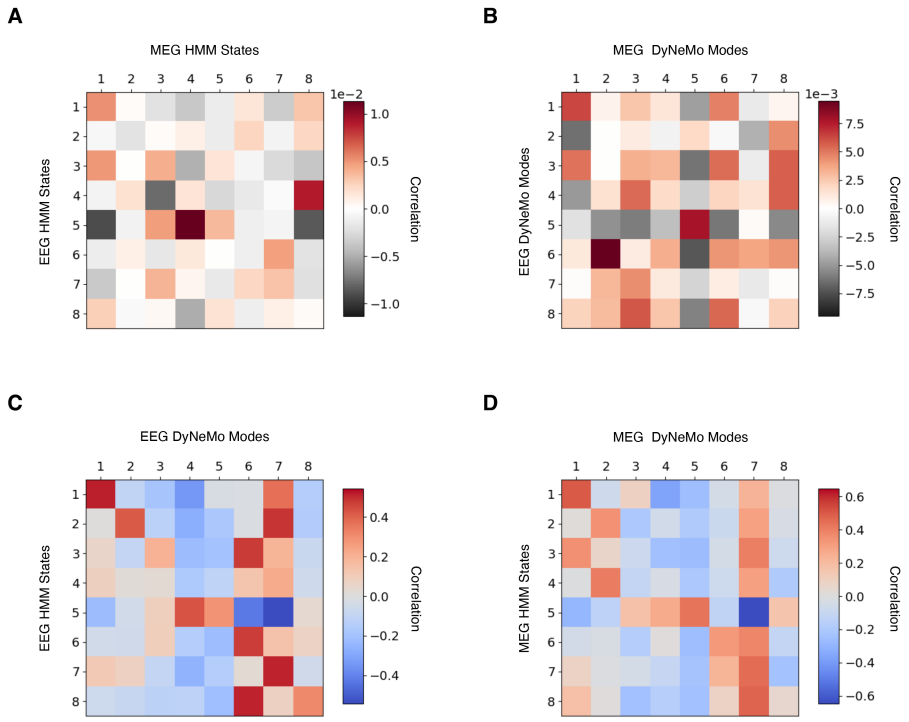

Figure A.3: Correlations of inferred state and mode time courses following state/mode matching. (A) Heatmap displaying the correlations between the HMM state time courses of the EEG and MEG datasets, after the state orders are aligned. **(B)** The same analysis as in (A) is conducted on the DyNeMo mode mixing coefficients. **(C)** Heatmap illustrating the correlations between the pre-aligned HMM state time courses and DyNeMo mode mixing coefficients for the EEG data, after the states and modes are aligned in the same order. **(D)** Similar to (C), the correlations between the pre-aligned HMM state time courses and DyNeMo mode mixing coefficients are shown for the MEG data.

A.2 Effect Sizes of Static PSDs

A.2.1 Derivation of Effect Size Variances

Mean Group Difference

The variance estimation of the mean group differences (i.e., COPEs) using GLM is well documented in [97]. A part of its derivation is repeated here for the clarity of our methodology. For more mathematical details, please refer to this paper.

By fitting a static power spectrum onto a GLM, we can quantify the uncertainty in mean group difference values arising from individual subjects. The GLM-based spectrum can be defined as

$$S_y(f) = XB(f) + e(f) \tag{A.1}$$

where $S_y(f)$ is an $N \times 1$ channel-averaged spectrum estimated at a frequency f across N subjects, X is an $N \times P$ design matrix with P regressors, and $e(f)$ is an $N \times 1$ vector of residual errors. In our case, we used two regressors to assign subjects to either of the two age groups. The resulting vector $B(f)$ of a size $P \times 1$ contains the fitted regression parameters.

To estimate regression parameters, we used the Moore-Penrose pseudo-inverse approach:

$$\hat{B}(f) = X^{+} S_y(f) \tag{A.2}$$

where $+$ denotes the Moore-Penrose pseudo-inverse. The whole vector of estimates across frequency, $\hat{B}$, is called the GLM *beta-spectrum*. Using these estimates, we calculated the mean group difference between the two age groups such that

$$\text{COPE}(f) = C\hat{B}(f) = \begin{bmatrix} -1 \\ 1 \end{bmatrix} \begin{bmatrix} \hat{b}_y(f) \\ \hat{b}_o(f) \end{bmatrix} \tag{A.3}$$

having C as the contrast matrix to take the difference between parameter estimates of the young ($\hat{b}_y$) and old ($\hat{b}_o$) group.

Now, we can compute the variance of COPEs, or Var(COPE), by first calculating the residual dot product $\sigma^2(f) = diag(R_y(f)R_y(f)^T)$ where $R_y(f)$ is the residuals

of the model fit defined as $S_y(f) - X\hat{B}(f)$. Scaling this with the Var(COPE) forming matrix, we have

$$\text{Var(COPE)}(f) = diag(C(X^TX)^{-1}C)\sigma^2(f) \tag{A.4}$$

Then, the standard error of our mean group difference can finally be written as $\text{SE(COPE)}(f) = \sqrt{\text{Var(COPE)}(f)}$.

Percentage Change

In the case of using the percentage change as our effect size estimates, we can formulate the estimate as

$$PC = h(\hat{B}) = \frac{(\hat{b}_o - \hat{b}_y)}{\hat{b}_y} \tag{A.5}$$

where PC is the percentage change of a static power spectrum from the young to old group across frequencies, and $h(\cdot)$ is a scalar-valued function of the regression parameters.

To estimate the variance of the percentage change, we employed the multivariate delta method. Assuming that our estimator $\hat{B}$ is asymptotically normal (based on the Central Limit Theorem) such that $\hat{B} \sim \mathcal{N}(B, \sigma^2(X^TX)^{-1})$, $h(\hat{B})$ can be estimated with the second-order Taylor expansion as

$$h(\hat{B}) \approx h(B) + \nabla h(B)^T(\hat{B} - B) \tag{A.6}$$

where B is the true value of our estimator. Using this equation, we can infer the variance of $h(\hat{B})$ with

$$\begin{aligned}
\text{Var(PC)} &= \text{Var}(h(\hat{B})) \\
&\approx \text{Var}(h(B) + \nabla h(B)^T(\hat{B} - B)) \\
&= \text{Var}(\nabla h(B)^T\hat{B}) \quad (\because \text{constant } h(B), (B)) \\
&= \nabla h(B)^T\text{Cov}(\hat{B})\nabla h(B) \\
&= \sigma^2 \nabla h(B)^T(X^TX)^{-1}\nabla h(B)
\end{aligned} \tag{A.7}$$

Since B cannot be known in a practical sense, we insert $\nabla h(\hat{B})$ instead to get the variance estimate and its standard error, $\text{SE(PC)} = \sqrt{\text{Var(PC)}}$.

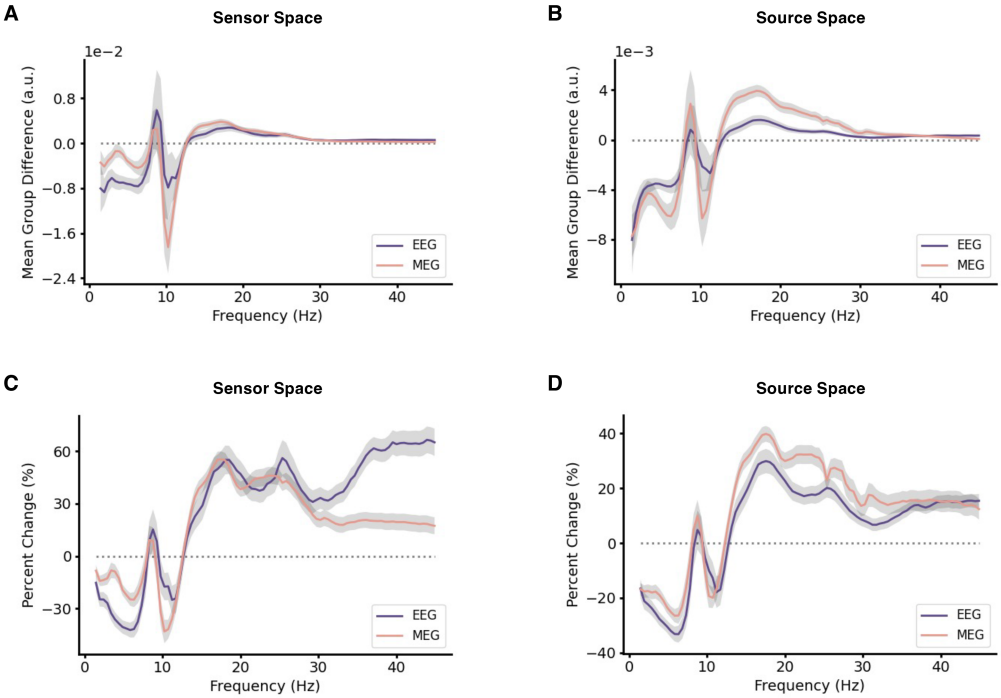

Figure A.4: Effect sizes of static power spectral differences between age groups in EEG and MEG. Changes in static spectral power are measured in terms of both absolute and relative values, with the mean group difference and percentage change computed between the old and young group. The GLM was applied to the sensor (parcel)-averaged PSDs using age group as a regressor, yielding the means and variances of group difference and percentage change. **(A)** Mean group differences of spectral power in EEG (purple) and MEG (pink) are computed from the sensor space PSDs at each frequency. The gray shading represents the standard error, reflecting subject variability. **(B)** The same analysis as in (A) is performed using the source space PSDs. **(C)** Mean percentage changes of spectral power in EEG (purple) and MEG (pink) are calculated from the sensor space PSDs at each frequency. The gray shading represents the standard error, reflecting subject variability. **(D)** The same analysis as in (C) is conducted using the source space PSDs.

A.3 Static Analysis

A.3.1 Age Effects in Wide-Band Static FC Maps

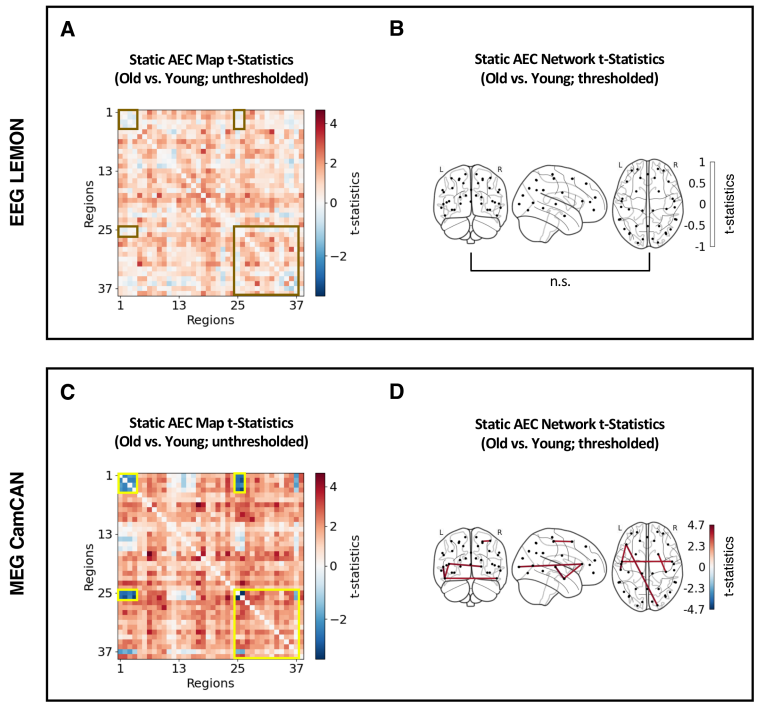

Figure A.5: Static source-space EEG and MEG reveal distinct between-group differences in the wide-band (1-45 Hz) FC maps. (A) Heatmap summarizing t-statistics of pair-wise AECs computed from the age group data. Exemplary regions exhibiting rough similarities across modalities were highlighted in boxes (brown). Table A.1 outlines the brain regions corresponding to the numerical indices. **(B)** From the heatmap, the significant t-values above the threshold ($p < 0.05$) defined from the max-t permutation test are presented as a brain network. **(C)** The same analysis as in (A) is performed on the MEG data, reporting t-statistics of AEC values for all inter-regional connections. Exemplary regions exhibiting rough similarities across modalities were highlighted in boxes (yellow). **(D)** The significant t-statistics identified by the max-t permutation test are depicted as a graph network, following the format of (B). Higher connectivity in old and young participants are represented by red and blue, respectively. Non-significant results are labeled as n.s.

In addition to static power maps, we examined the effect of age on the wide-band static FC maps by applying the same analysis as described in Section 2.3.2. The group-averaged AEC maps revealed an elevated FC in young participants around the occipital lobe (parcels 1-4, 25-26) and in old participants around frontal areas (parcels 25-37) across both M/EEG (Fig. A.5A, C). However, the SNR of such connectivity appeared to be higher in MEG. Statistical analysis of age-

group differences revealed significantly higher interhemispheric connectivity between frontal and temporal regions in MEG but not in EEG (Fig. A.5B, D). No significant age-related differences were observed in EEG. Adding onto the results from static power maps, our exploration of FC maps alludes to an enhanced sensitivity of MEG over EEG in discerning age-related effects within the spatial domain.

A.3.2 Group-Averaged Static Power and FC Maps

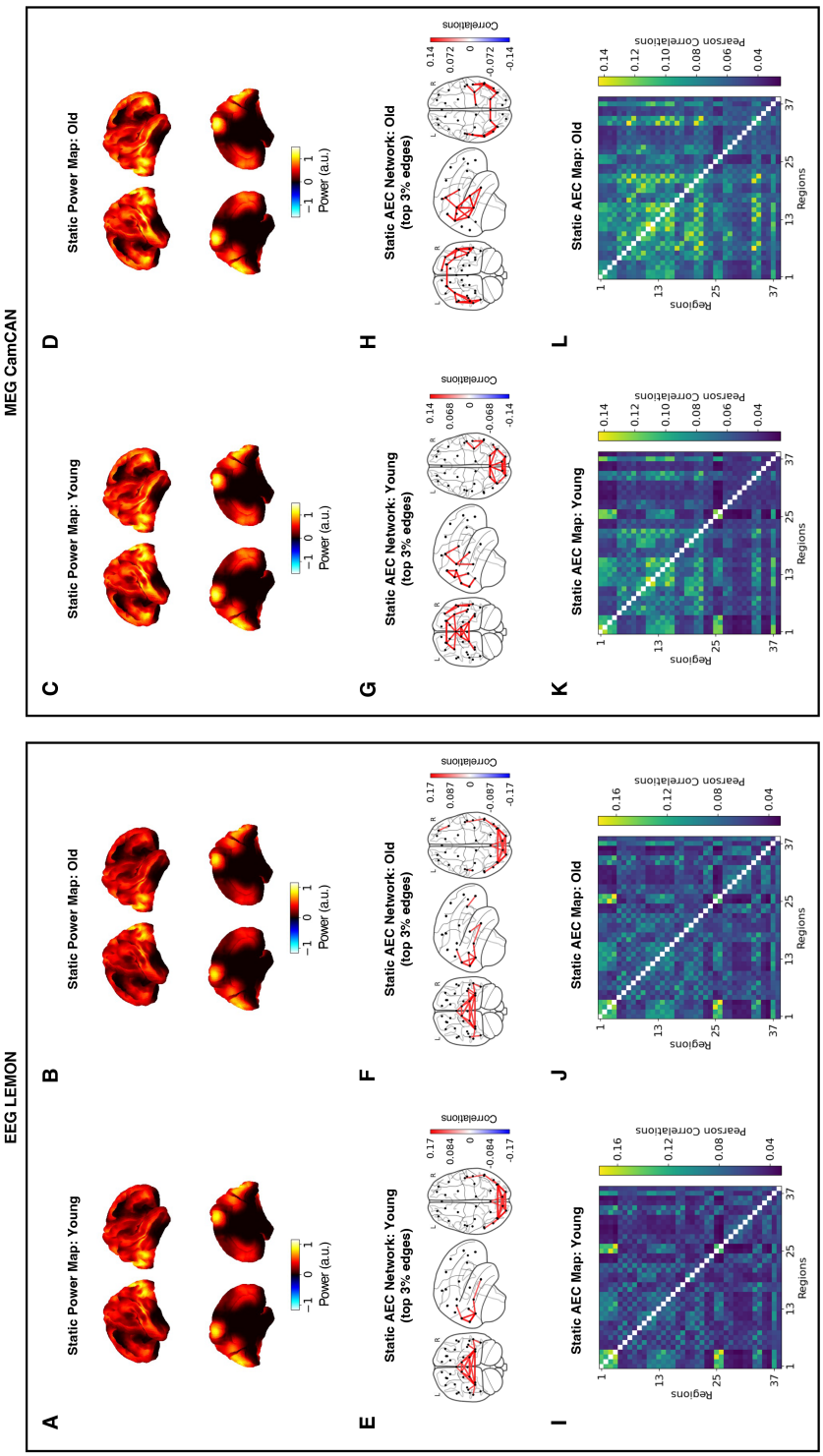

Figure A.6: Static wide-band (1-45 Hz) power and connectivity maps of young and old participants in source-space M/EEG. (A) The distribution of power is computed by integrating subject-averaged PSDs of the young participants across the frequency range of 1-45 Hz and represented as a brain surface map. Power values are standardized at the subject-level. **(B)** Similar to (A), the power map of old participants is obtained. **(C)-(D)** The power maps are computed as in (A) and (B), respectively, but using the MEG data. **(E)** Pair-wise amplitude envelope correlations are calculated from the source-reconstructed brain activities and depicted as a brain network. The top 3% of correlation strengths (above the 97th percentile) are displayed for visualization. **(F)** The same analysis as in (E) is performed on the old participants. **(G)-(H)** The functional connectivity networks are computed as in (E) and (F), respectively, using the MEG data. **(I)-(L)** Heatmaps of the entire correlation values between different regions of the brain are presented for the young and old participants for the EEG and MEG data. For details of the parcellated brain regions, refer to Table A.1.

A.4 Dynamic Analysis

A.4.1 Mode Power and FC Maps of the Entire Dataset

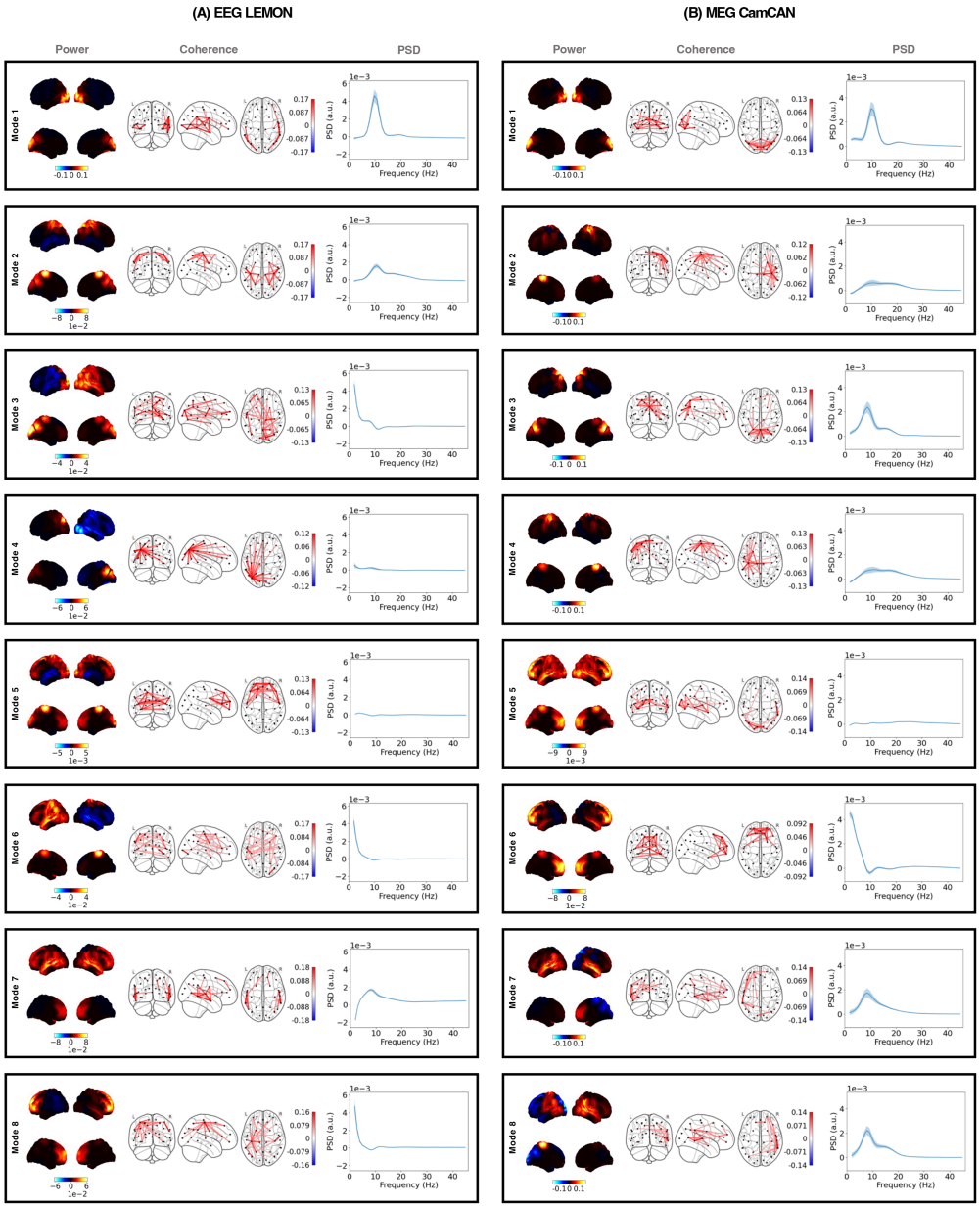

Figure A.7: DyNeMo resting-state network modes inferred from the EEG and MEG datasets. (A) Each box shows the power map (left), FC network (middle), and parcel-averaged PSDs (right) of each DyNeMo mode for 96 EEG subjects. The power maps show lateral surfaces at the top and medial surfaces at the bottom. The FC networks illustrate connections with the top 3% coherence values. The shaded areas of the PSDs represent the standard error of the mean. The power maps, FC networks, and PSDs are visualized relative to their average across all modes. **(B)** The plots follow the same format as (A), showing the RSNs computed from 96 MEG subjects.

A.4.2 Summary Statistics of DyNeMo Modes

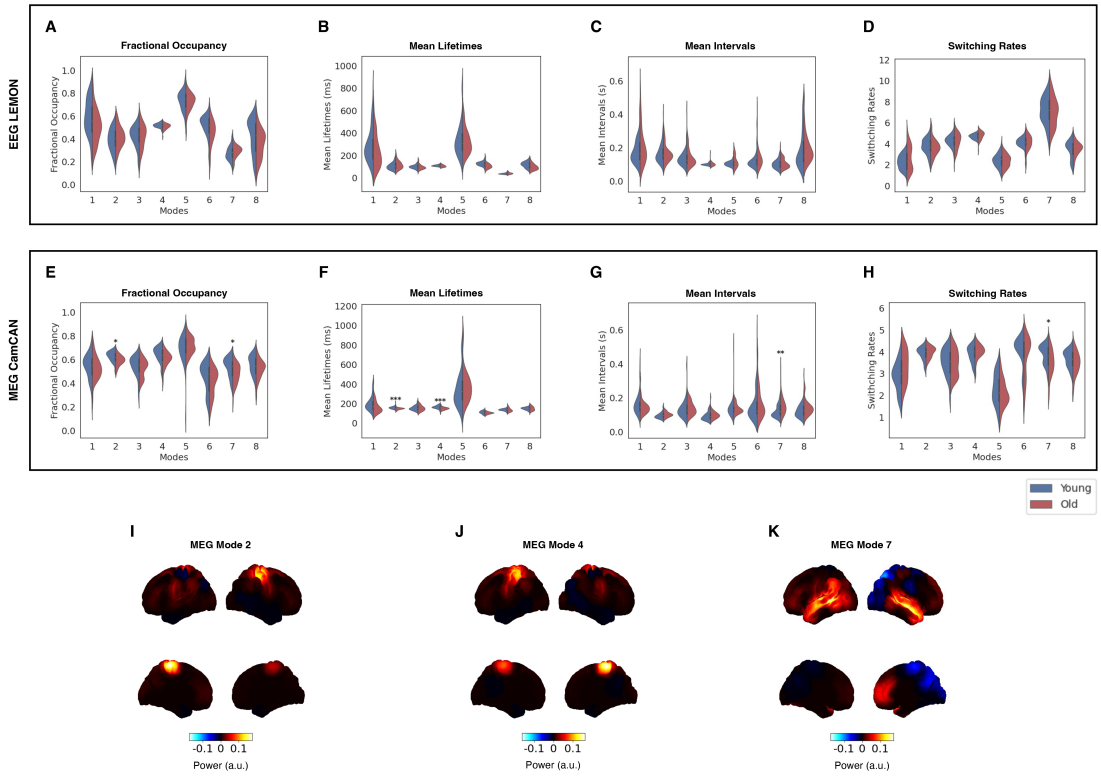

Figure A.8: Dynamic age-related effects in DyNeMo summary statistics are observed in source-space MEG but not in EEG. Summary statistics of the mode time courses inferred from the MEG data – **(A)** fractional occupancies, **(B)** mean mode activation lifetimes, **(C)** mean mode activation intervals, and **(D)** mode switching rates – are plotted as distributions over the grouped subjects. **(E)-(H)** Same plots for the MEG data are presented. The modes showing significant between-group differences are marked by asterisks. Statistical significance was determined using max-t permutation tests for each dataset, Bonferroni-corrected by the number of metrics (n=4). (***: $p < 0.001$, **: $p < 0.01$, *: $p < 0.05$, n.s.: non-significant) **(I)-(K)** Wide-band (1-45 Hz) power maps of three MEG modes, which show significant between-group differences in summary statistics, are illustrated. These power maps are averaged over the entire dataset.

A.4.3 Age Effects in Mode-Specific PSDs

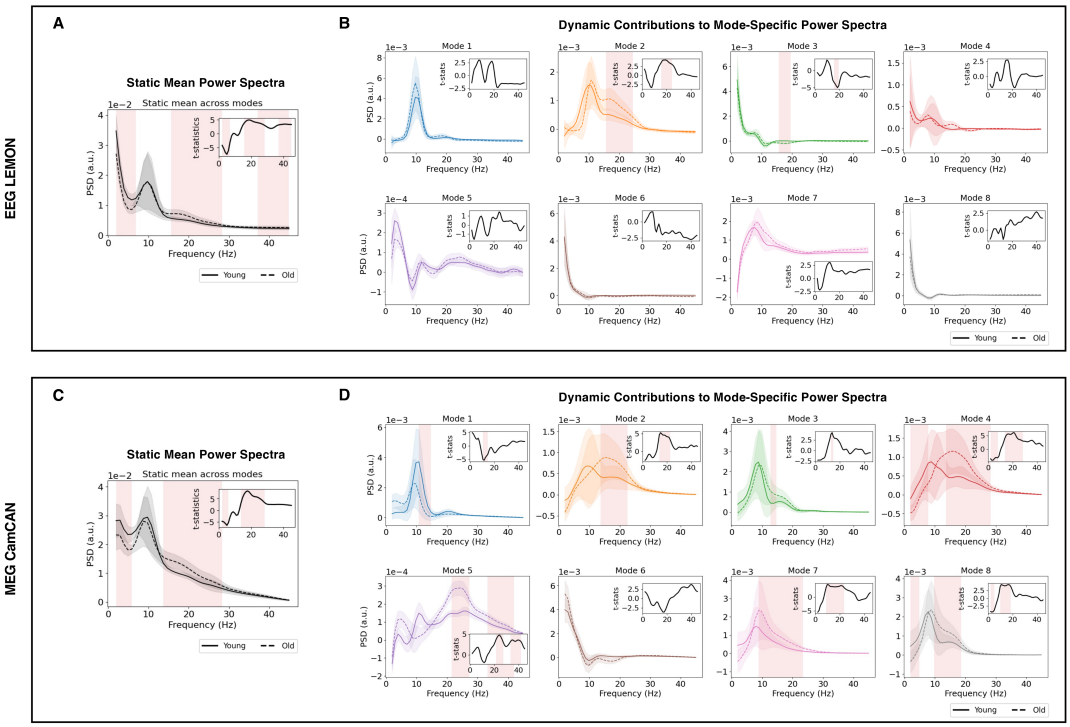

Figure A.9: Source-space EEG and MEG DyNeMo modes report distinct spectral differences when dynamic information is isolated. (A) The mean PSD across all modes is obtained from the EEG data for young (solid) and old (dotted) participants and averaged over the subjects and parcels. A cluster permutation test is conducted on the parcel-averaged static mean PSD to detect age-related static effects. Frequencies exhibiting statistical significance ($p < 0.05$; Bonferroni-corrected, n=9) are highlighted in red. **(B)** The mode-specific PSDs of the EEG data are averaged across each group and parcels after the mean across modes is subtracted at the subject level. These group-averaged, mean-subtracted PSDs of young (solid) and old (dotted) participants are illustrated for each DyNeMo mode. Cluster permutation tests are conducted on parcel-averaged, mean-subtracted PSDs of each mode to detect age-related dynamic effects. Frequencies exhibiting statistical significance ($p < 0.05$; Bonferroni-corrected, n=9) are highlighted in red. **(C)** The same analysis as in (A) is performed on the MEG data. **(D)** The same analysis as in (B) is performed on the MEG data. For all plots, the inset portrays t-statistics contrasting its corresponding PSDs of the young and old group.

A.4.4 Age Effects in State/Mode-Specific Power and FC

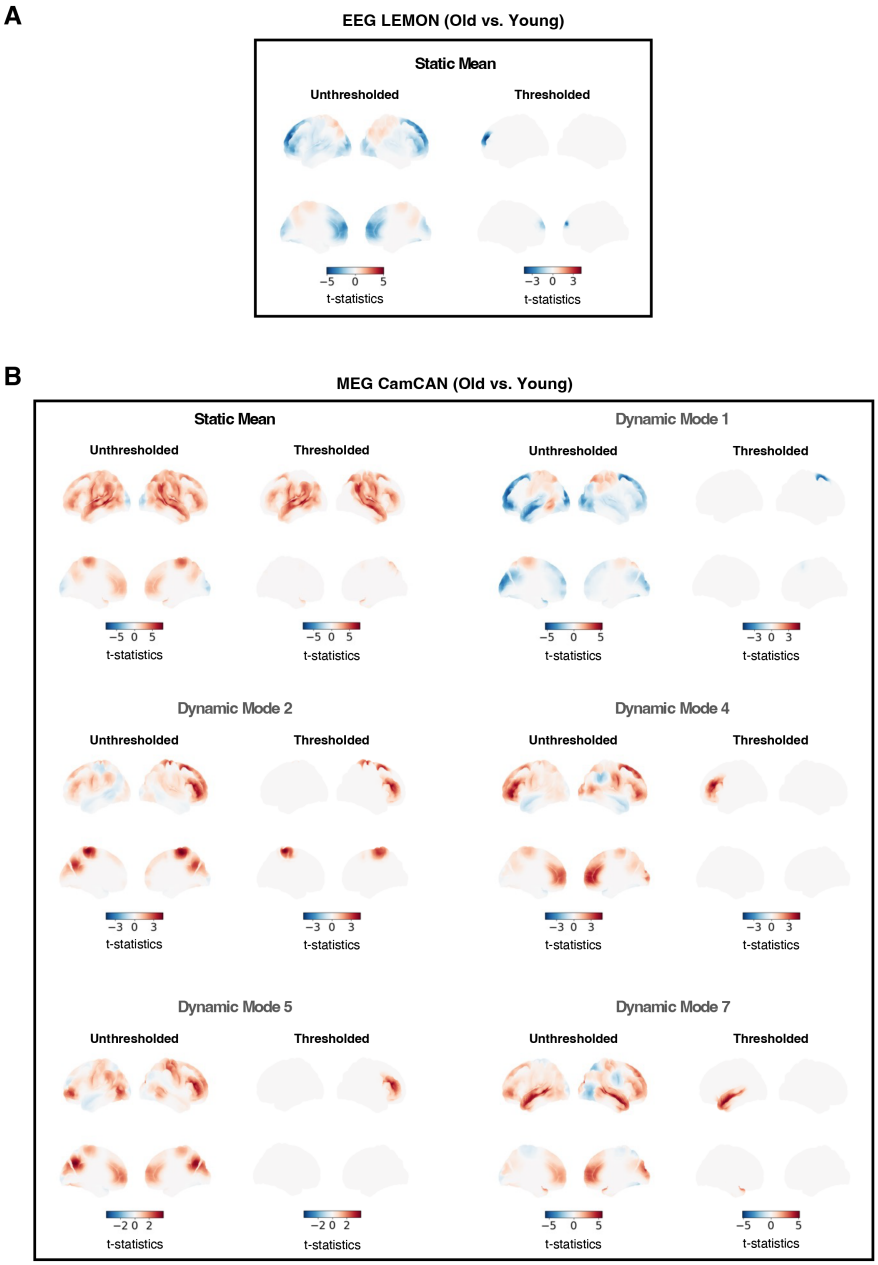

Figure A.10: Dynamic age effects in spatial power distributions are observed in source-space MEG DyNeMo modes but not in EEG. The result of statistical analysis conduced on the wide-band (1-45 Hz) static mean and dynamic mode-specific power maps is presented here. Only the power maps with significant age effects are plotted. **(A)** Power maps with significant between-group differences are illustrated for the EEG data. Power maps on the left display t-statistics between groups, and the parcels with significant t-values are colored on the right. **(B)** The same analysis is performed on the MEG data. Max-t permutation tests were used to evaluate statistical significance. Parcels are marked significant if $p < 0.05$ (Bonferroni-corrected, n=9).

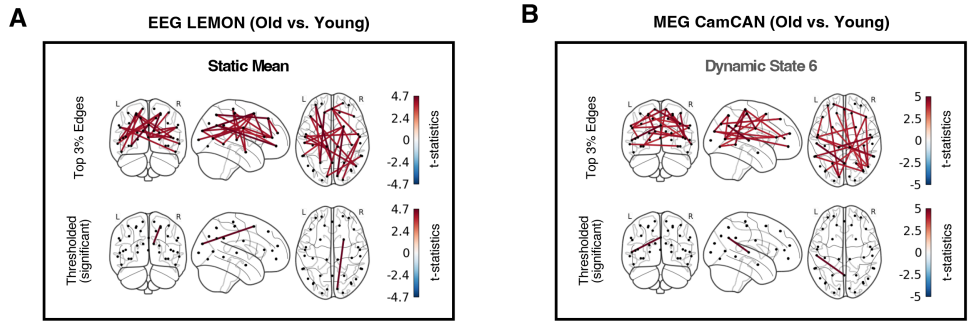

Figure A.11: Source-space M/EEG HMM states exhibit distinct spatial distributions of connectivity differences between age groups. The result of max-t permutation tests conducted on FC maps is presented here, once the static mean FC across all states was separated from the wide-band (1-45 Hz) state-specific dynamic FC maps. The static mean or dynamic state-specific FC maps are plotted only if one or more significant connections were present. **(A)** FC maps with significant between-group differences are illustrated for the EEG data. Only the static mean FC map revealed meaningful age effect. On the top, t-statistics of the FC maps between the old and young group (above the 97-th percentile) are portrayed. Connection edges with significant t-values ($p < 0.05$; Bonferroni-corrected, n=9) are displayed on the bottom. **(B)** The same analysis as in (A) is conducted for the MEG data. Significant age effect was present in State 6.

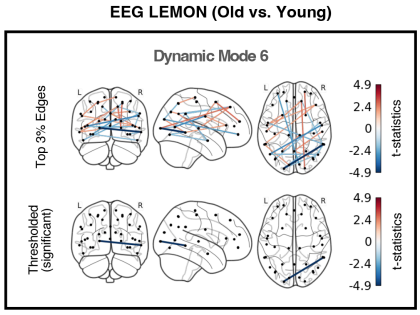

Figure A.12: Source-space EEG reports a DyNeMo mode with between-group FC differences, when dynamic information is isolated. The result of max-t permutation tests conducted on FC maps is presented here, once the static mean FC across all modes was separated from the wide-band (1-45 Hz) mode-specific dynamic FC maps. The between-group differences in FC maps are plotted only if one or more significant connections were present. On the top, t-statistics of the FC maps between the old and young group (above the 97-th percentile) are portrayed. Connection edges with significant t-values ($p < 0.05$; Bonferroni-corrected, n=9) are displayed on the bottom.

In addition to state- and mode-specific power maps, we examined dynamic age effects on functional connectivity. Group-level max-t permutation tests on FC maps, however, produced an obscure outcome. While HMM-based EEG analysis identified age effects in the static mean FC, MEG detected age effects in State 5 (Fig. A.11). Despite these connections being reproducible (Fig. A.18), the unthresholded FC map differences between two age groups distinguished no specific regions with apparent connectivity difference and rather appeared noisy. Furthermore, age effects in the static mean FC of EEG was not comparable to those found in the static analysis.

With DyNeMo, EEG showed age-related effects in Mode 6, but MEG did not report any age effects (Fig. A.12). However, effects in EEG were not reproducible with respect to run-to-run variability, emerging only in two model runs (Fig. A.19). Overall, the complexities in discerning age-related effects in FC from our datasets were evident, echoing the existing ambiguity and lack of consensus in the healthy aging literature concerning age-associated connectivity changes. This may indicate that age might exert relatively less influence on RSN connectivity than its power.

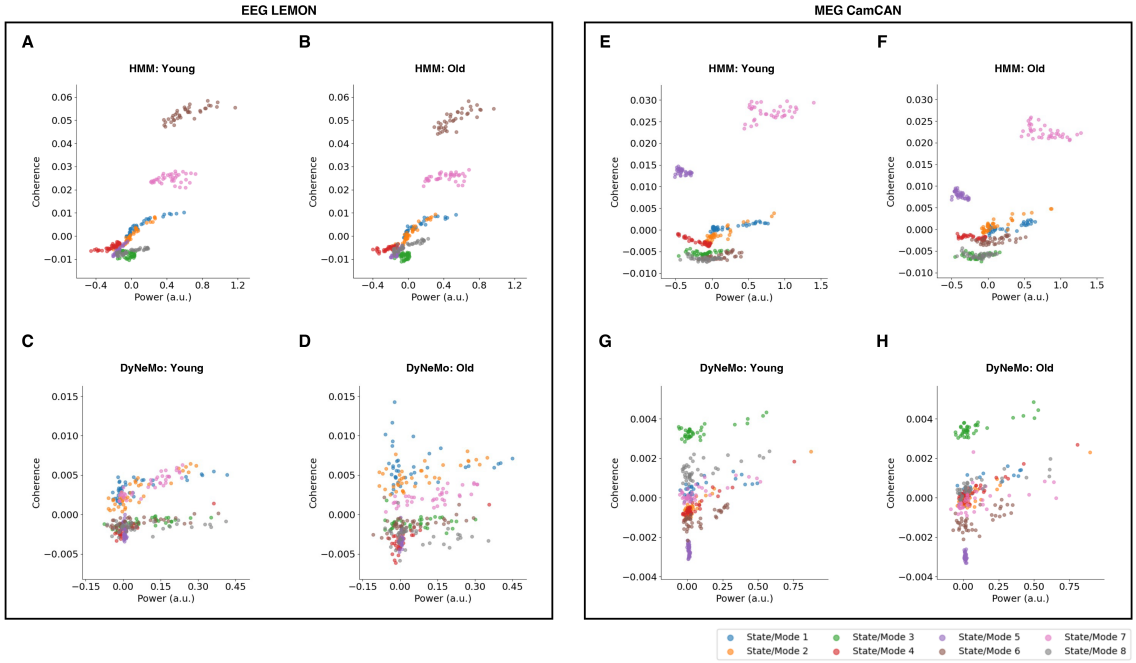

Figure A.13: Distributions of dynamic power and coherence in source-space EEG and MEG. Distributions of power and coherence values, computed from the HMM multi-taper spectra, are plotted for **(A)** young and **(B)** old participants relative to their state/mode-wise means. The same analysis is conducted using DyNeMo GLM PSDs for **(C)** young and **(D)** old subjects. **(E)-(H)** The identical analysis is repeated on the MEG dataset. Each color represents a state or mode, and each scatter point denotes a specific parcellated region. With DyNeMo, power values were rescaled with the maximum alpha mixing coefficient value of each mode at the subject level for better visualization.

A.5 Reproducibility Analysis

A.5.1 Reproducibility of Age Effects in Summary Statistics

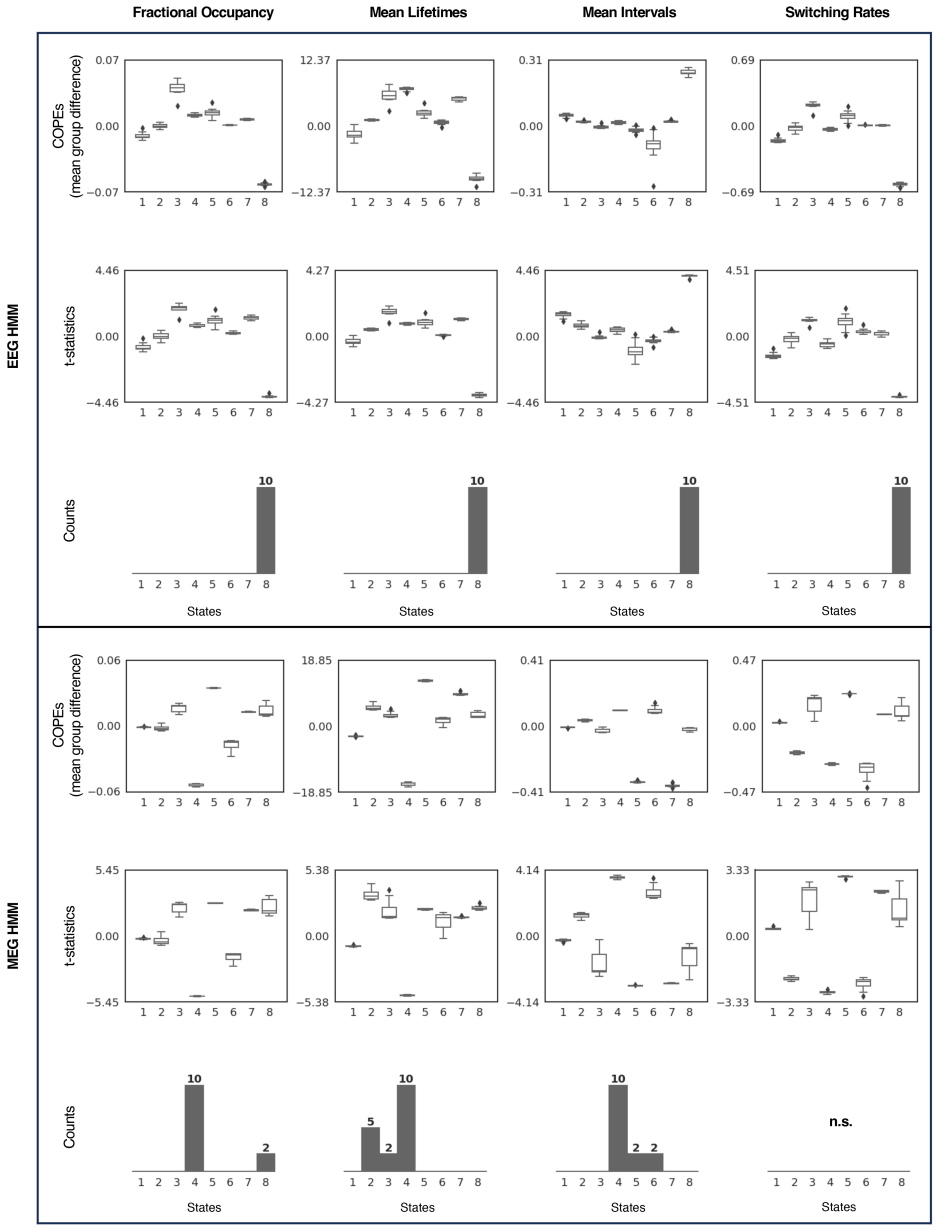

Figure A.14: Run-to-run variability of between-group differences in HMM summary statistics for source-space EEG and MEG data. The reproducibility of the differences between age groups in four summary metrics derived from the HMM state activation time courses was evaluated for EEG (upper panel) and MEG (lower panel). For each panel, the distributions of COPEs and t-statistics across the best 10 runs are illustrated as box plots (top, middle). The bar plot in the bottom displays the number of runs with significant between-group differences for each state. If no states demonstrated significance across all runs, it was denoted by n.s. (non-significant).

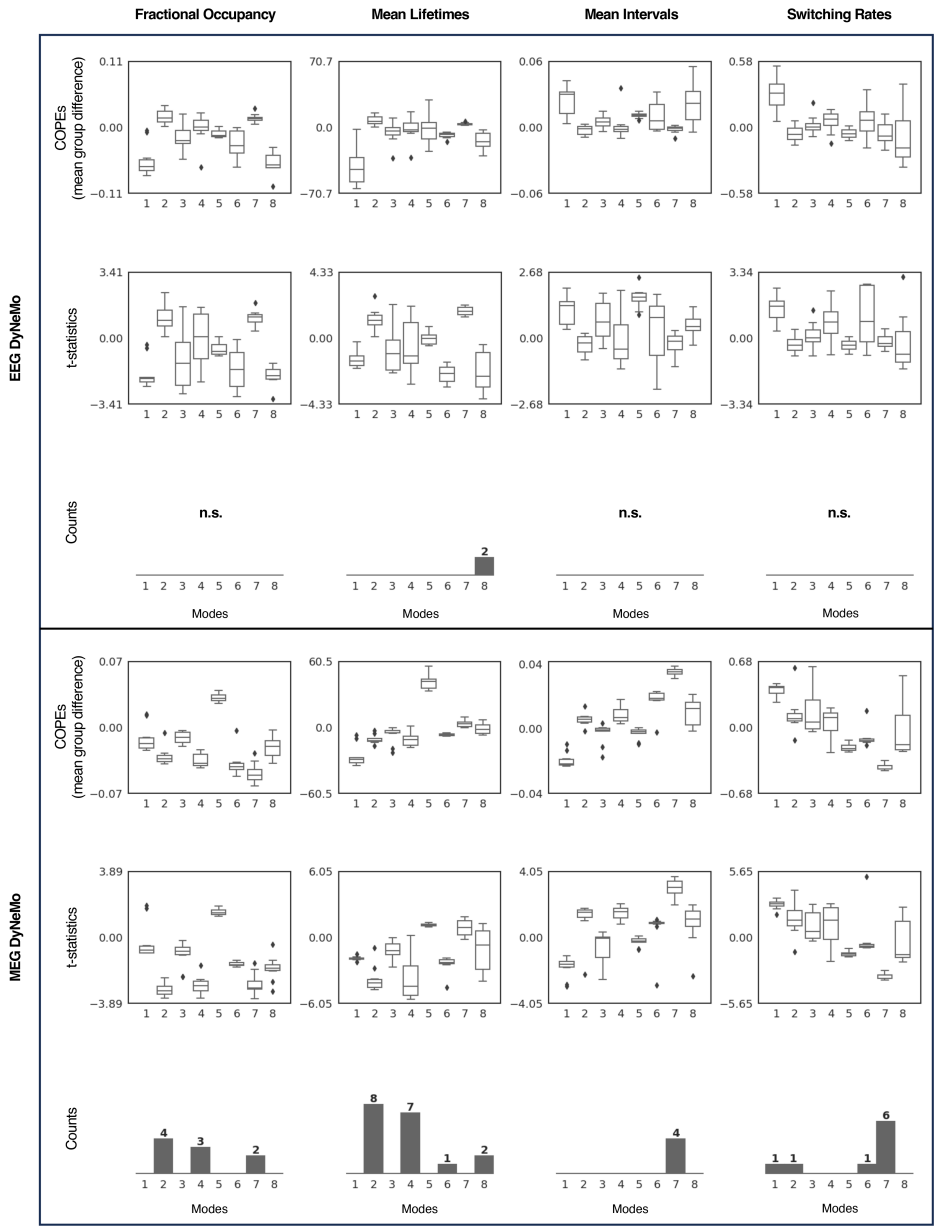

Figure A.15: Run-to-run variability of between-group differences in DyNeMo summary statistics for source-space EEG and MEG data. The reproducibility of the differences between age groups in four summary metrics derived from the DyNeMo mode activation time courses was evaluated for EEG (upper panel) and MEG (lower panel). For each panel, the distributions of COPEs and t-statistics across the best 10 runs are illustrated as box plots (top, middle). The bar plot in the bottom displays the number of runs with significant between-group differences for each mode. If no modes demonstrated significance across all runs, it was denoted as n.s. (non-significant).

With DyNeMo, the effect sizes of between-group differences in summary statistics showed higher variability in general compared to those of HMM. This is expected, as DyNeMo is a linear mixture model and thus has an extra flexibility in modeling

time-varying covariances, since it can infer multiple solutions of mode mixing coefficient factors.

A.5.2 Reproducibility of Age Effects in Power Maps

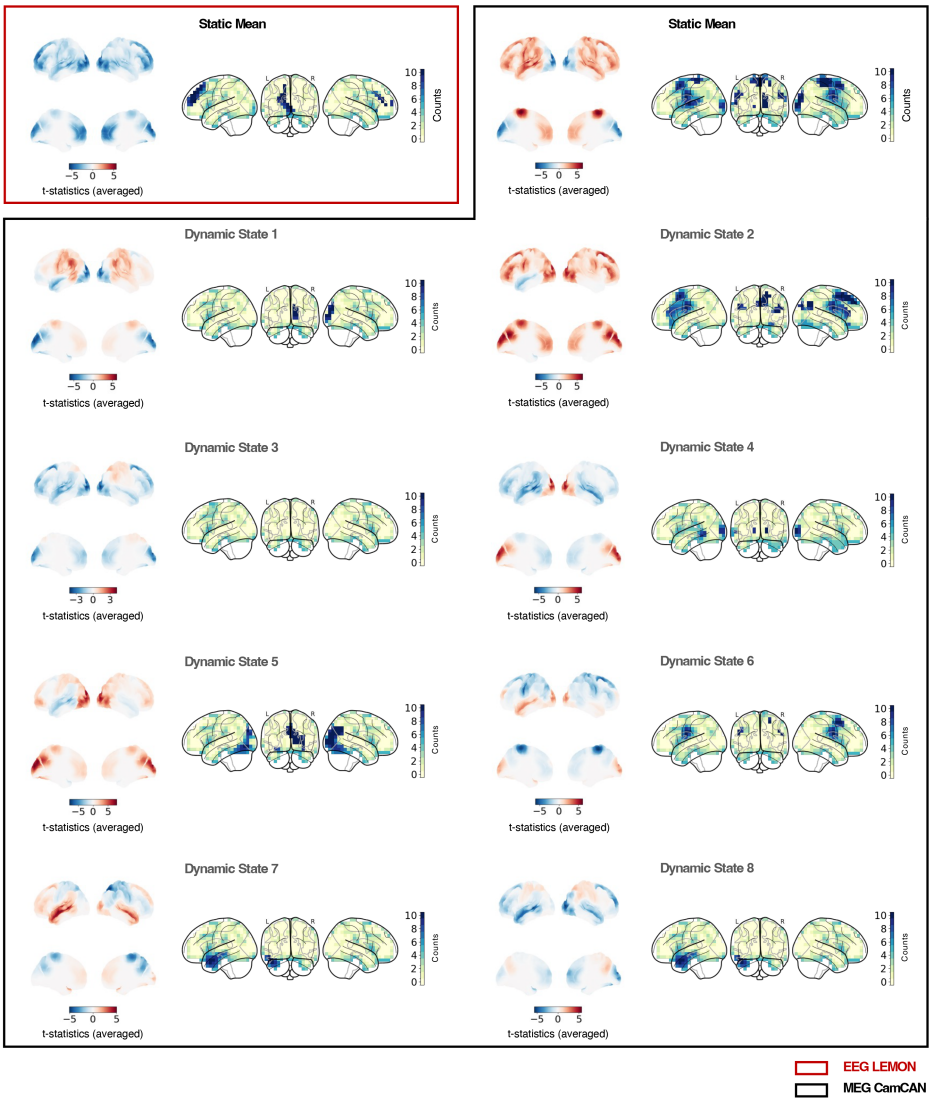

Figure A.16: Run-to-run variability of between-group differences in HMM power maps. The reproducibility of age effects in the static mean and dynamic mean-subtracted state power maps was examined for EEG (red box) and MEG (black box). Only the power maps that exhibited significant between-group differences in at least one parcel over the best 10 runs are depicted for each modality. For each state, the averaged spatial distribution of t-statistics is presented on the left, encompassing both lateral (top) and medial (bottom) surfaces. Higher power in old and young participants are represented in red and blue, respectively. On the right, the brain surface highlights the voxel-weighted number of model runs that demonstrate significant between-group differences in each parcel.

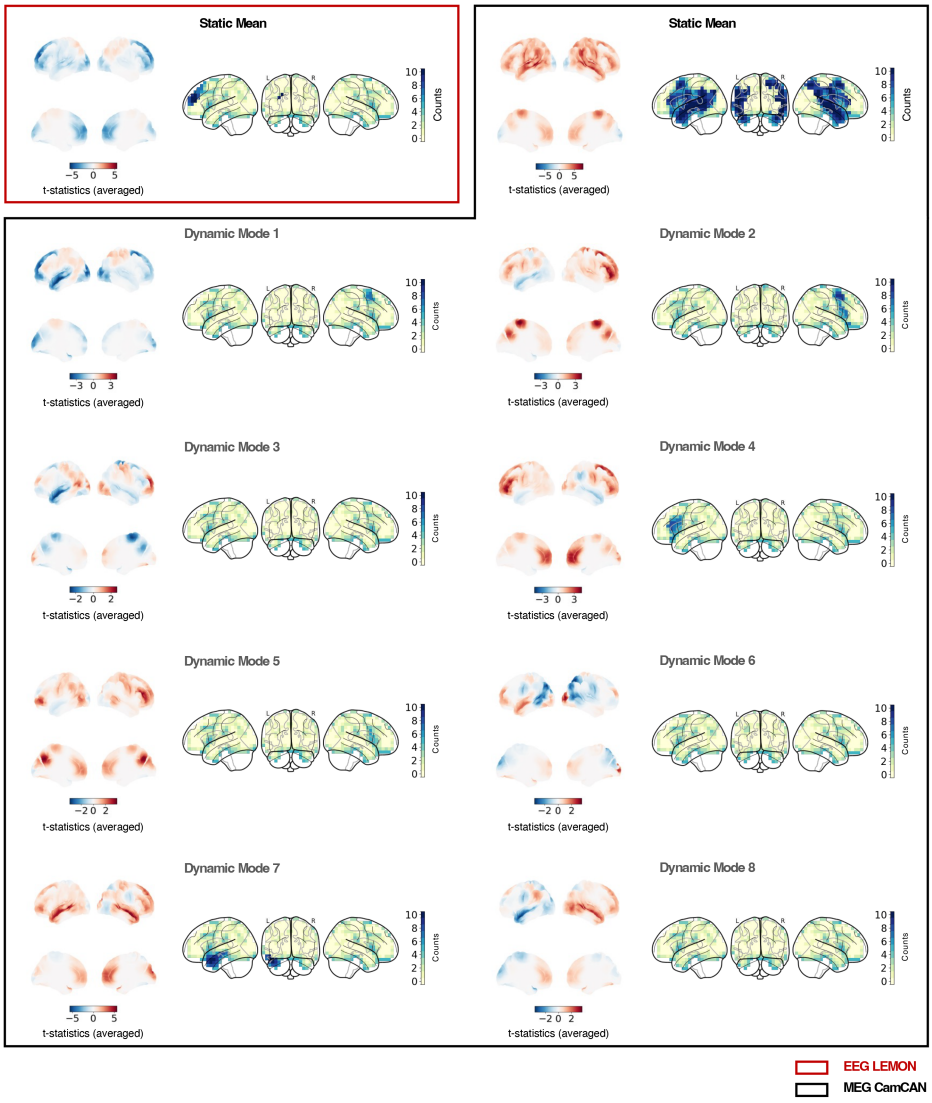

Figure A.17: Run-to-run variability of between-group differences in DyNeMo power maps. The reproducibility of age effects in the static mean and dynamic mean-subtracted mode power maps was examined for EEG (red box) and MEG (black box). Only the power maps that exhibited significant between-group differences in at least one parcel over the best 10 runs are depicted for each modality. For each mode, the averaged spatial distribution of t-statistics is presented on the left, encompassing both lateral (top) and medial (bottom) surfaces. Higher power in old and young participants are represented in red and blue, respectively. On the right, the brain surface highlights the voxel-weighted number of model runs that demonstrate significant between-group differences in each parcel.

A.5.3 Reproducibility of Age Effects in FC Maps

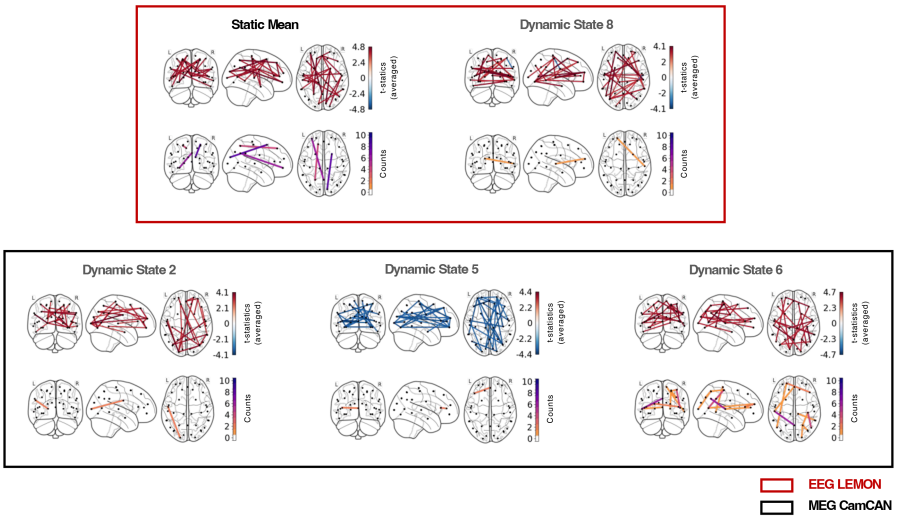

Figure A.18: Run-to-run variability of between-group differences in HMM functional connectivity networks. The reproducibility of age effects in the static mean and dynamic mean-subtracted FC maps, derived from state-specific coherences, was evaluated for EEG (red box) and MEG (black box). Only the FC maps that demonstrated statistically significant between-group differences in at least one pairwise connection over the best 10 runs are selected for visualization. For each state, the spatial networks of t-statistics are averaged across runs, and the edges with t-values over the 97-th percentile are presented on the top. Higher FC in old and young participants are represented in red and blue, respectively. On the bottom, the number of model runs showing significant between-group differences is highlighted for each connection edge.

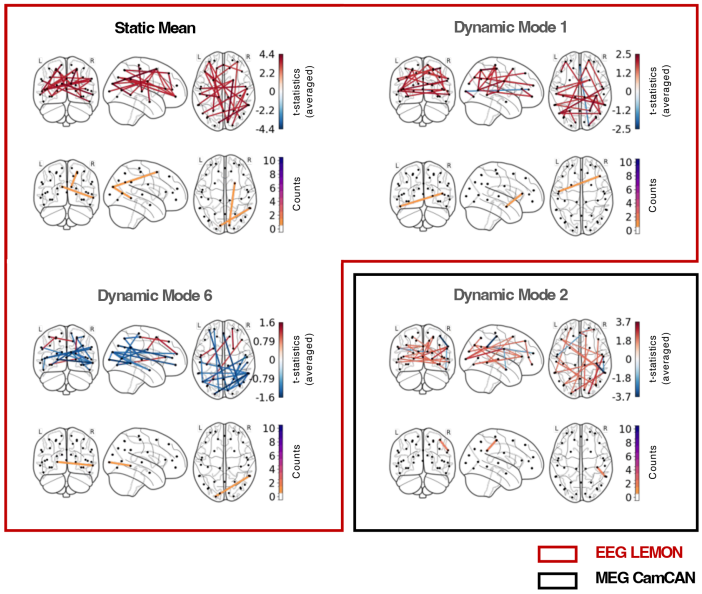

Figure A.19: Run-to-run variability of between-group differences in DyNeMo functional connectivity networks. The reproducibility of age effects in the static mean and dynamic mean-subtracted FC maps, derived from mode-specific coherences, was evaluated for EEG (red box) and MEG (black box). Only the FC maps that demonstrated statistically significant between-group differences in at least one pairwise connection over the best 10 runs are selected for visualization. For each mode, the spatial networks of t-statistics are averaged across runs, and the edges with t-values over the 97-th percentile are presented on the top. Higher FC in old and young participants are represented in red and blue, respectively. On the bottom, the number of model runs showing significant between-group differences is highlighted for each connection edge.

B

Supplementary Materials for Chapter 3

B.1 Data & Methods

B.1.1 Group Demographics

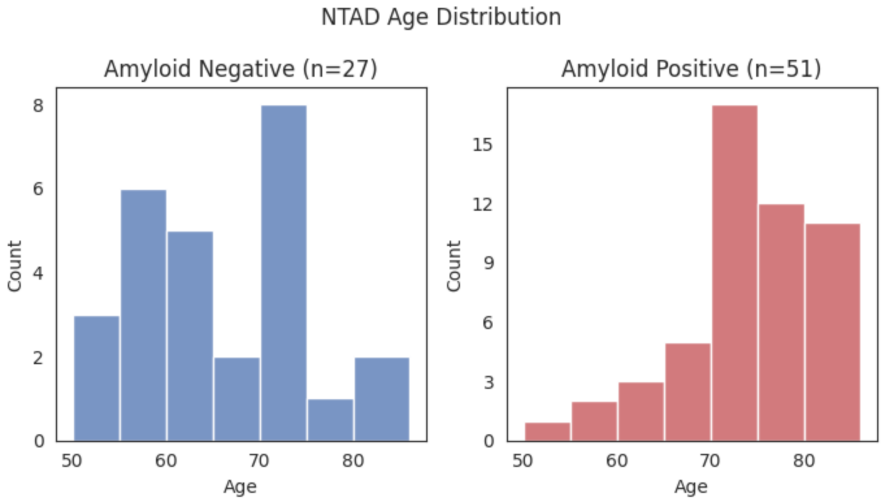

Figure B.1: Age distributions of participants in the AN and AP group. Histograms depict the distribution of ages for the AN (blue) and AP (red) group in the NTAD dataset. The dataset has a sample size of 27 AN and 51 AP participants.

	Group		Test Results		# Missing Values	
	AN	AP (+ MCI/AD)	Statistics*	p-value	AN	AP (+ MCI/AD)
N	27	51	-	-	-	-
Sex (M/F)	14/13	21/30	-	-	-	-
Age (years)	65.8 (8.73)	74.2 (6.69)	t=4.69	**1.20E-5**	0	0
MMSE (/30)	29.2 (0.786)	24.8 (3.76)	t'=-5.94	**0**	0	6
Education (years)	16.2 (3.95)	14.2 (4.36)	t=-1.87	0.0658	2	11
Volume: Hippocampus	0.557 (0.0613)	0.428 (0.0806)	t=-7.07	**8.60E-10**	0	5
Volume: Grey Matter	40.7 (1.74)	38.4 (1.61)	t=-4.58	**1.87E-5**	0	3
Volume: White Matter	38.2 (1.92)	36.0 (2.30)	t=-5.19	**1.82E-6**	0	3
Volume: Brain	1.40E6 (1.49E5)	1.35E6 (1.27E5)	t=-1.59	0.116	0	3

Table B.1: Group-level comparison of participant characteristics. The descriptive statistics of participant demographics and their group-level comparison are shown for the AN and AP group. The independent t-test, denoted by t, and the max-t nonparametric permutation test, denoted by t', were used to conduct the group-level statistical tests. Metrics of demographics showing significant between-group differences are marked with bold font. Missing values were excluded from their respective statistical tests. AN: amyloid-negative, AP: amyloid-positive, MCI: mild cognitive impairment, M: male, F: female, MMSE: Mini-Mental State Examination.

B.1.2 Design Matrix for GLM

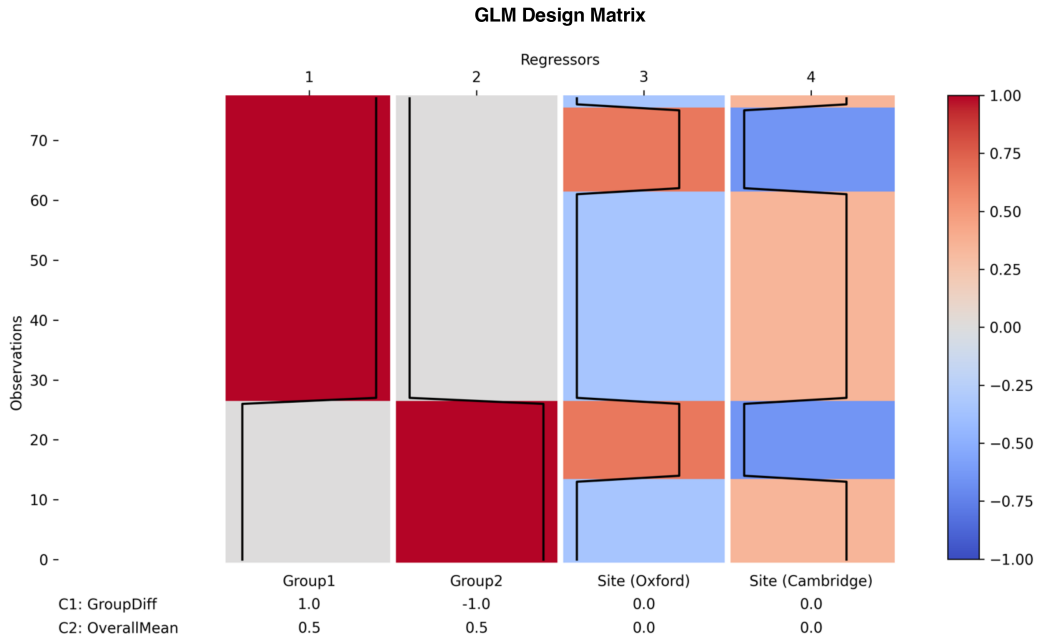

Figure B.2: Design matrix and contrasts for a group-level GLM. A GLM design matrix consisted of two group regressors and two site regressors. For each regressor, its values across 78 subjects are plotted on the top in columns. The table on the bottom lists the contrasts that were used to compute the COPEs and their variance, with corresponding weights for each regressor.

B.1.3 Matching State and Mode Orders

After the states and modes of the HMM and DyNeMo evaluated or trained on the NTAD M/EEG data were matched into the same order, the quality of their alignment was assessed based on the correlations between their state and mode time courses as in Appendix A.1.4. The maximum correlation values of the NTAD data were higher than those of the LEMON and Cam-CAN datasets in general. This ensures that the order of RSNs has been sufficiently matched with respect to the previous chapter.

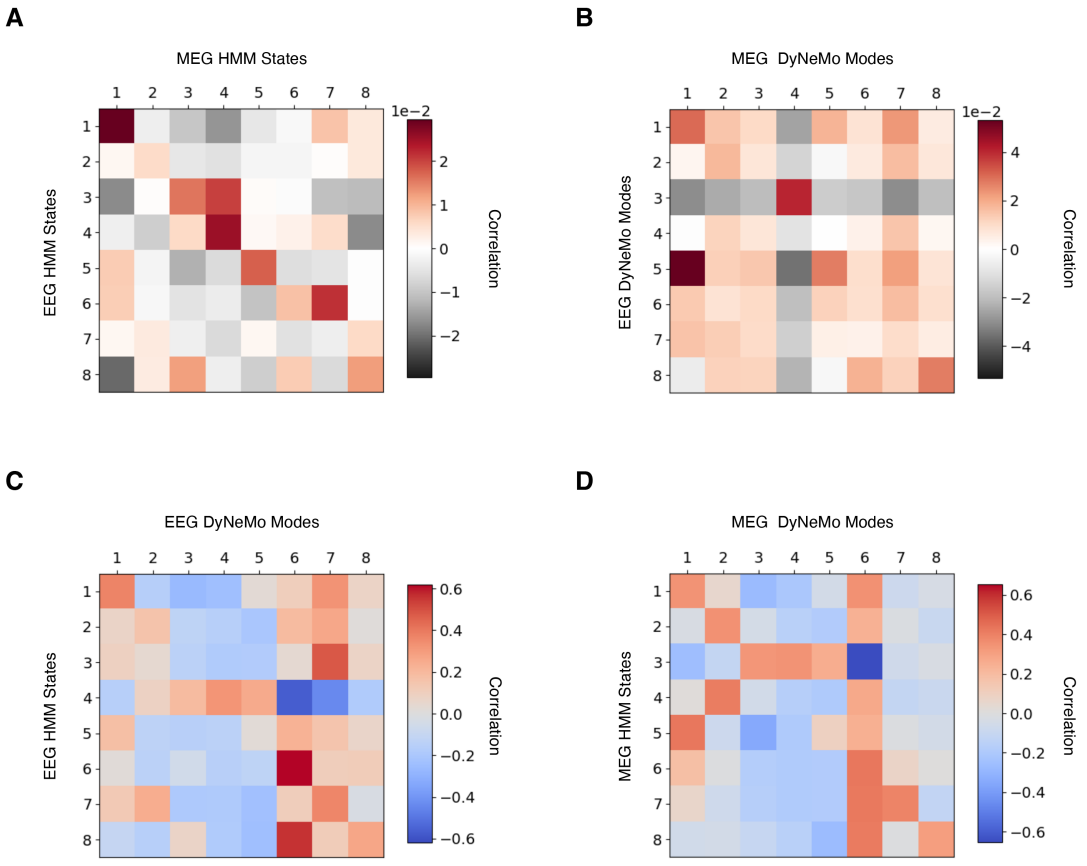

Figure B.3: Correlations of inferred state and mode time courses following state/mode matching. **(A)** Heatmap displaying the correlations between the HMM state time courses of the NTAD EEG and MEG data, after the state orders are aligned. **(B)** The same analysis as in (A) is conducted on the DyNeMo mode mixing coefficients. **(C)** Heatmap illustrating the correlations between the HMM state time courses and DyNeMo mode mixing coefficients for the EEG data, after the states and modes are aligned in the same order. **(D)** Similar to (C), the correlations between pre-aligned HMM state time courses and DyNeMo mode mixing coefficients are shown for the MEG data.

B.2 Static Analysis

B.2.1 Group-Averaged Static Power and FC Maps

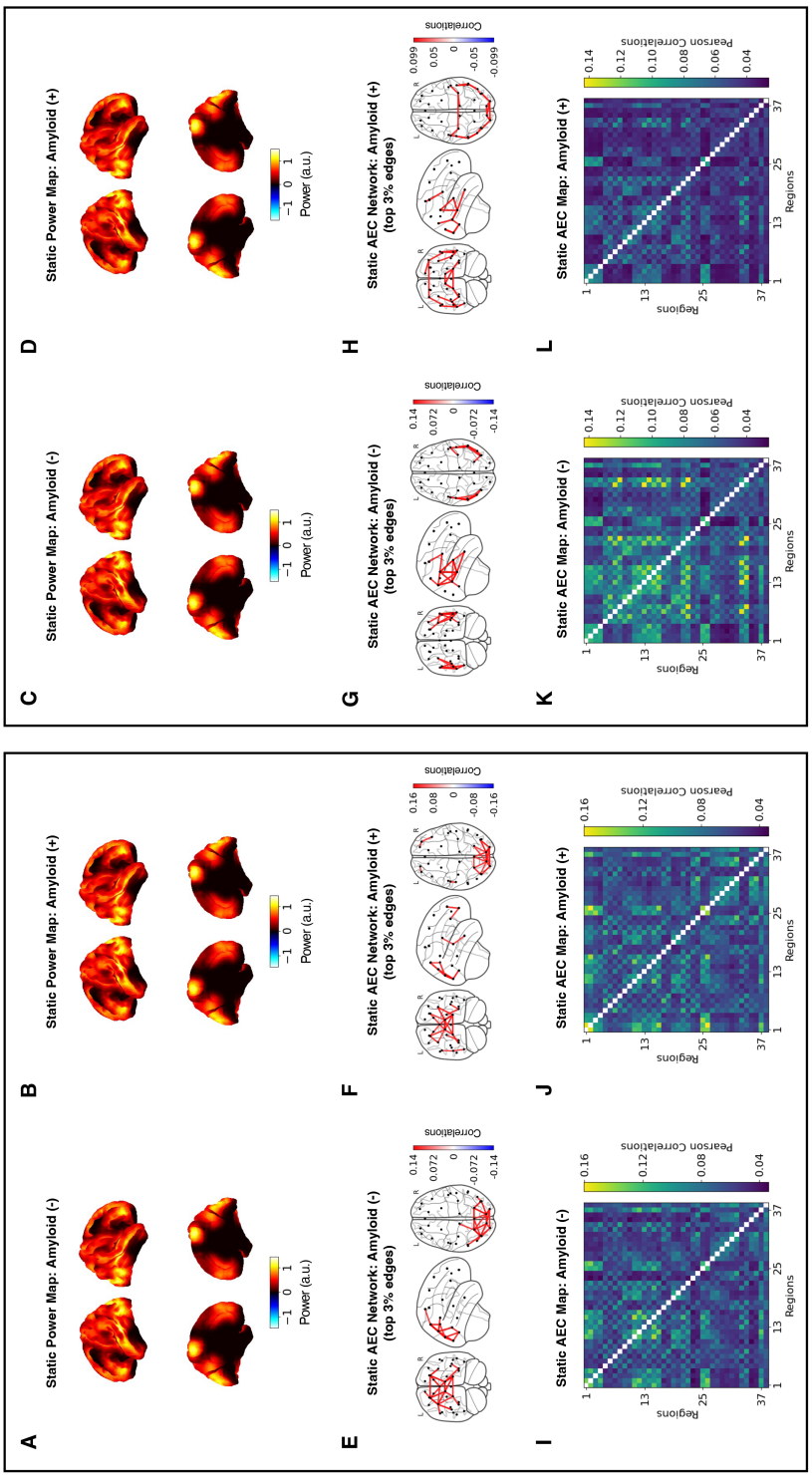

Figure B.4: Static wide-band (1-45 Hz) power and connectivity maps of AN and AP participants in source-space M/EEG. (A) The distribution of power is computed by taking the regression estimates of a group-level GLM fitted to wide-band (1-45 Hz) power maps of the AP participants and represented as a brain surface map. Power values are standardized at the subject-level. **(B)** Similar to (A), the power map of AP participants is obtained. **(C)-(D)** The power maps are computed as in (A) and (B), respectively, but using the MEG data. **(E)** Pair-wise amplitude envelope correlations of AN participants are calculated from the source-reconstructed brain activities and depicted as a brain network. The top 3% of correlation strengths (above the 97-th percentile) are displayed for visualization. **(F)** The same analysis as in (E) is performed on the AP participants. **(G)-(H)** The functional connectivity networks are computed as in (E) and (F), respectively, using the MEG data. **(I)-(L)** Heatmaps of the entire correlation values between different regions of the brain are presented for the AN and AP participants in the EEG and MEG data. For details of the parcellated brain regions, refer to Table A.1.

One thing to note from the group-averaged FC maps above is how similar the

structure of static AEC maps of AN participants (Fig. B4I, K) look to those of the healthy old participants in the EEG LEMON and MEG Cam-CAN datasets (Fig. A6J, L). This validates the quality of the NTAD data for cognitively healthy subjects and highlights how consistently healthy aging effects in FC are represented across different datasets.

B.2.2 Effects of MCI & Early-stage AD in Wide- and Narrow-Band Static FC Maps

In addition to static power maps, we examined the effect of MCI and early-stage AD on the wide- and narrow-band static FC maps. In the wide band, the group-averaged AEC maps revealed modality-dependent spatial patterns, where EEG showed a global increase in FC with MCI and early-stage AD, while MEG showed a global decrease (Fig. B5A, C). Statistical analysis of AN and AP group differences showed significantly lower interhemispheric connectivity between temporal and parietal regions in MEG for AP subjects (Fig. B5D). However, no significant effects of MCI and early-stage AD were observed in EEG as in Section 3.3.2 (Fig. B5B).

In the narrow bands, static FC maps revealed significant effects of MCI and early-stage AD in the alpha band for M/EEG and the beta band for MEG (Fig. B.6). In EEG, AP participants had reduced fronto-temporal alpha connectivity within the left hemisphere. The observed effects were much stronger for MEG, showing a globally reduced connectivity in both the alpha and beta band.

Although observations above do not coincide perfectly with previous findings, general connectivity decrease in the alpha and beta band following the MCI and early-stage AD has been reproduced here.

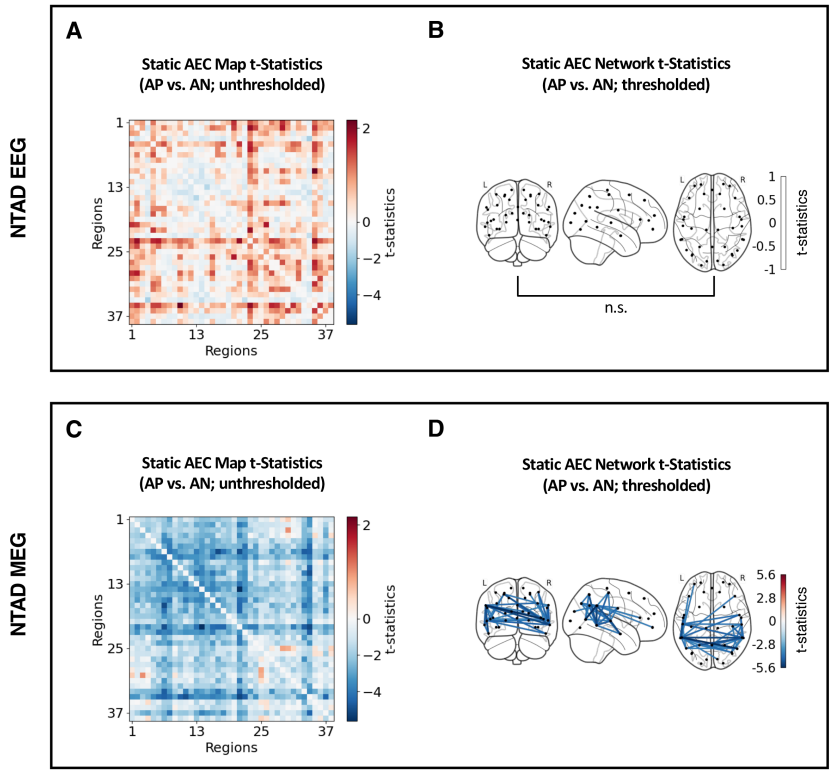

Figure B.5: Static source-space MEG reveals reduced wide-band (1-45 Hz) FC in the parieto-temporal regions for AP subjects. (A) Heatmap summarizing t-statistics of pair-wise AECs computed from the AN and AP group data. Table A.1 outlines the brain regions corresponding to the numerical indices. **(B)** From the heatmap, the significant t-values above the threshold ($p < 0.05$) defined from the max-t permutation test are presented as a brain network. **(C)** The same analysis as in (A) is performed on the MEG data, reporting t-statistics of AEC values for all inter-regional connections. **(D)** The significant t-statistics identified by the max-t permutation test are depicted as a graph network, following the format of (B). Higher connectivity in AP and AN participants are represented by red and blue, respectively. Non-significant results are labeled as n.s.

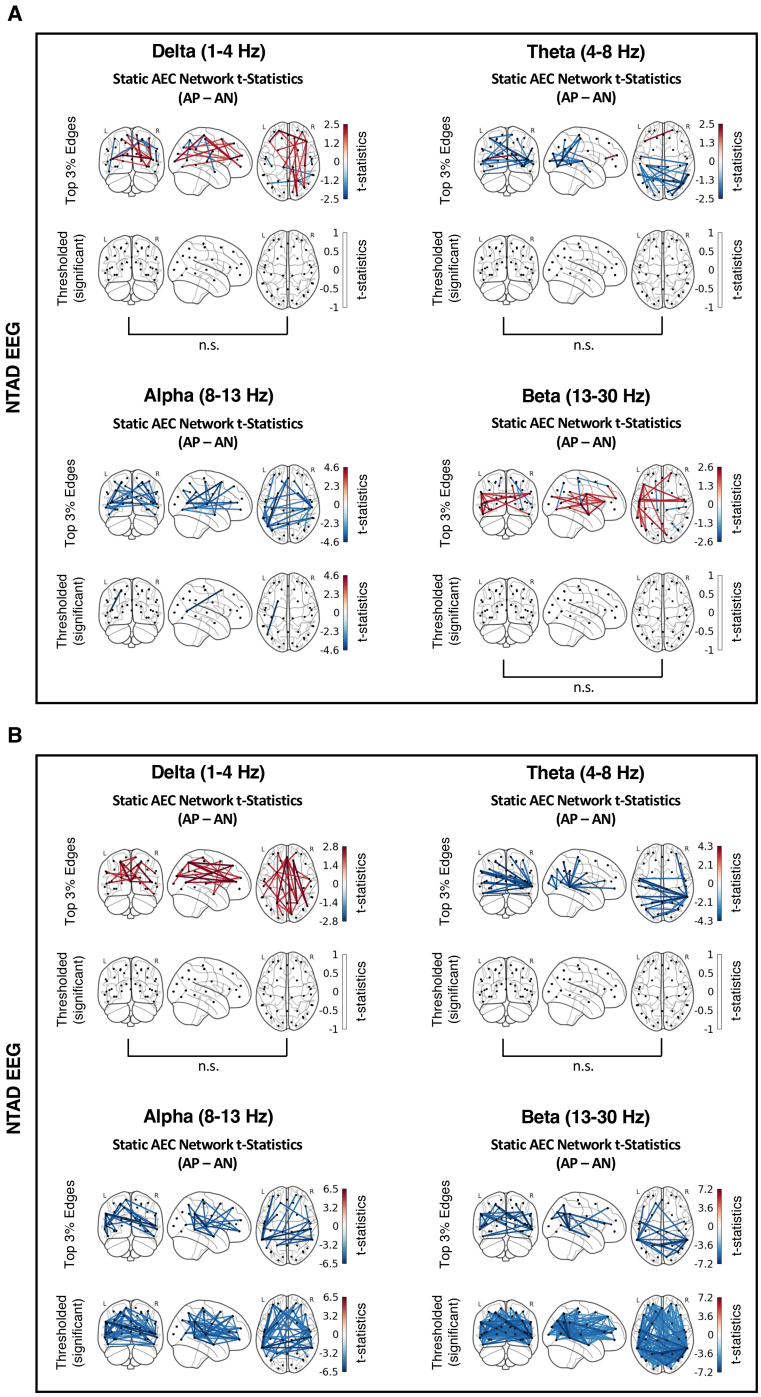

Figure B.6: Narrow-band static FC maps illustrate the effects of MCI and early-stage AD in the alpha and beta bands. (A) The functional connectivity difference between the AP and AN group is quantified as t-statistics and plotted as a brain network graph for each frequency band. The FC difference networks illustrate connections with the top 3% t-statistics values. The max-t permutation tests ($p < 0.05$; Bonferroni-corrected, n=4) were applied to narrow-band static FC maps of the EEG data to highlight the difference between AP and AN participants. The connection edges with significant t-statistics are highlighted. Higher AEC in AP and AN participants are represented by red and blue, respectively. Non-significant results are labeled as n.s. **(B)** The same analysis as in (A) is conducted for the MEG data.

B.3 Dynamic Analysis

B.3.1 Mode Power and FC Maps of the Entire Dataset

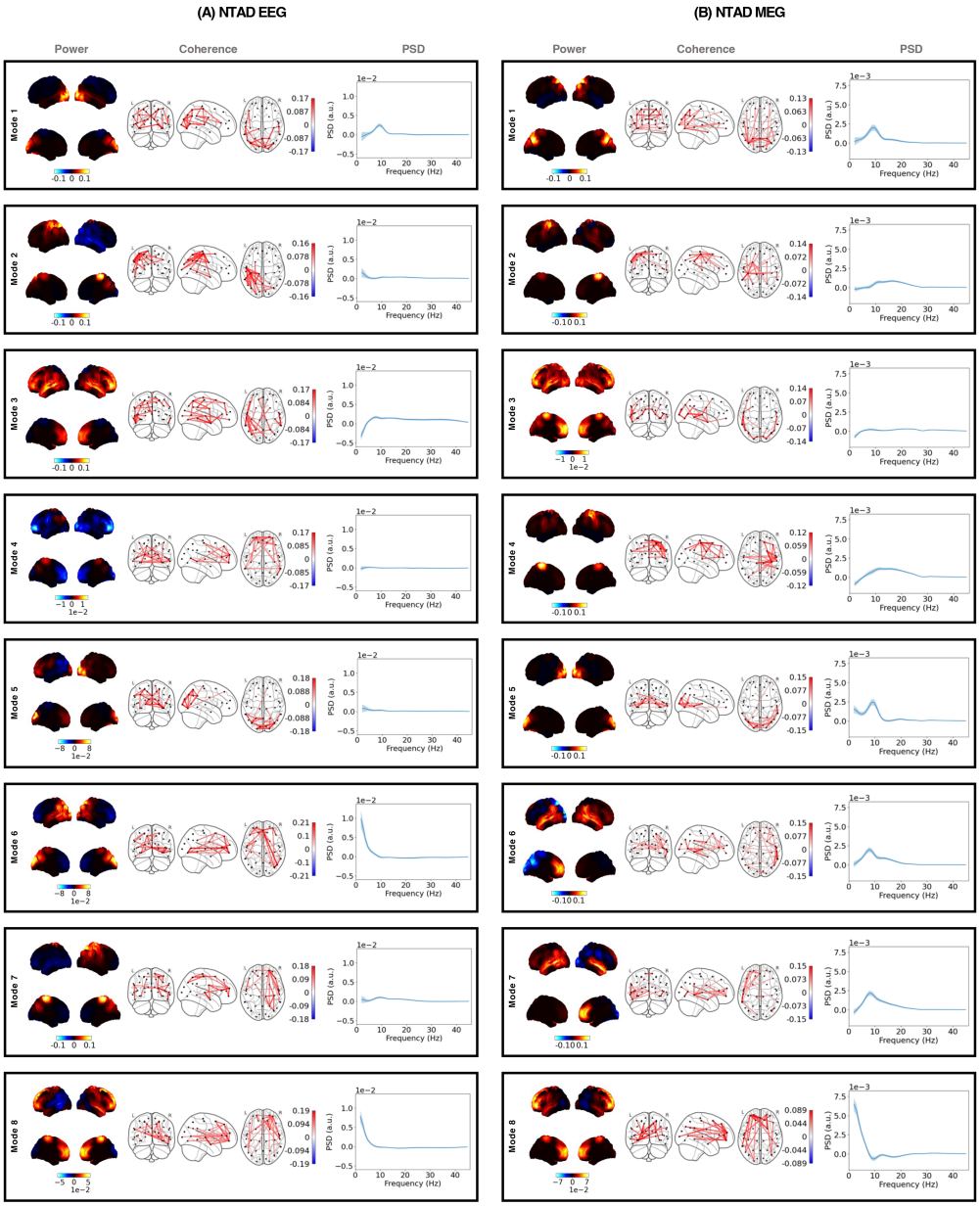

Figure B.7: DyNeMo resting-state network modes inferred from the EEG and MEG datasets. (A) Each box shows the power map (left), FC network (middle), and parcel-averaged PSDs (right) of each DyNeMo mode derived from EEG for 78 subjects in the NTAD dataset. The power maps show lateral surfaces at the top and medial surfaces at the bottom. The FC networks illustrate connections with the top 3% coherence values. The shaded areas of the PSDs represent the standard error of the mean. The power maps, FC networks, and PSDs are visualized relative to their average across all modes. **(B)** The plots follow the same format as (A), showing the RSNs derived from MEG for 78 subjects in the NTAD dataset.

B.3.2 Summary Statistics of DyNeMo Modes

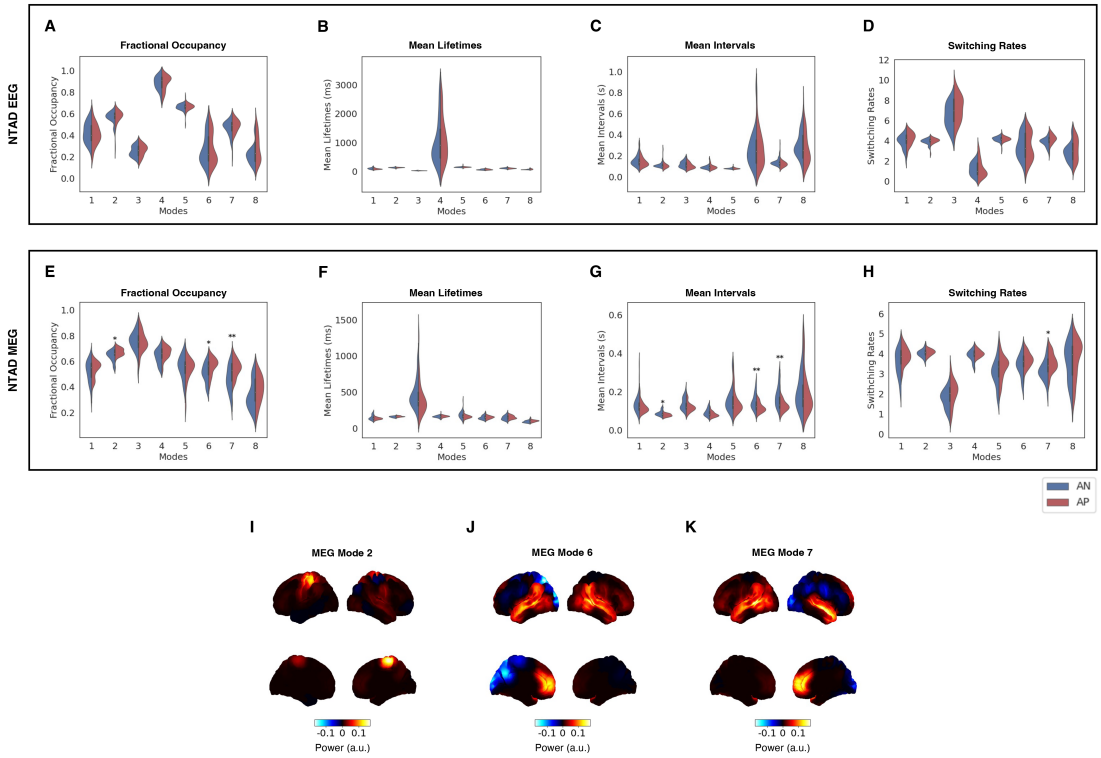

Figure B.8: Dynamic effects of MCI & early-stage AD in DyNeMo summary statistics are associated with sensorimotor and fronto-temporal networks in MEG. Summary statistics of the mode time courses inferred from the MEG data – **(A)** fractional occupancies, **(B)** mean mode activation lifetimes, **(C)** mean mode activation intervals, and **(D)** mode switching rates – are plotted as distributions over the grouped subjects. **(E)-(H)** Same plots for the MEG data are presented. The modes showing significant between-group differences are marked by asterisks. Statistical significance was determined using max-t permutation tests for each dataset, Bonferroni-corrected by the number of metrics (n=4). (***: $p < 0.001$, **: $p < 0.01$, *: $p < 0.05$, n.s.: non-significant) **(I)-(K)** Wide-band (1-45 Hz) power maps of three MEG modes, which show significant between-group differences in summary statistics, are illustrated. These power maps are averaged over the entire dataset.

B.3.3 Effects of MCI & Early-stage AD in Mode-Specific PSDs

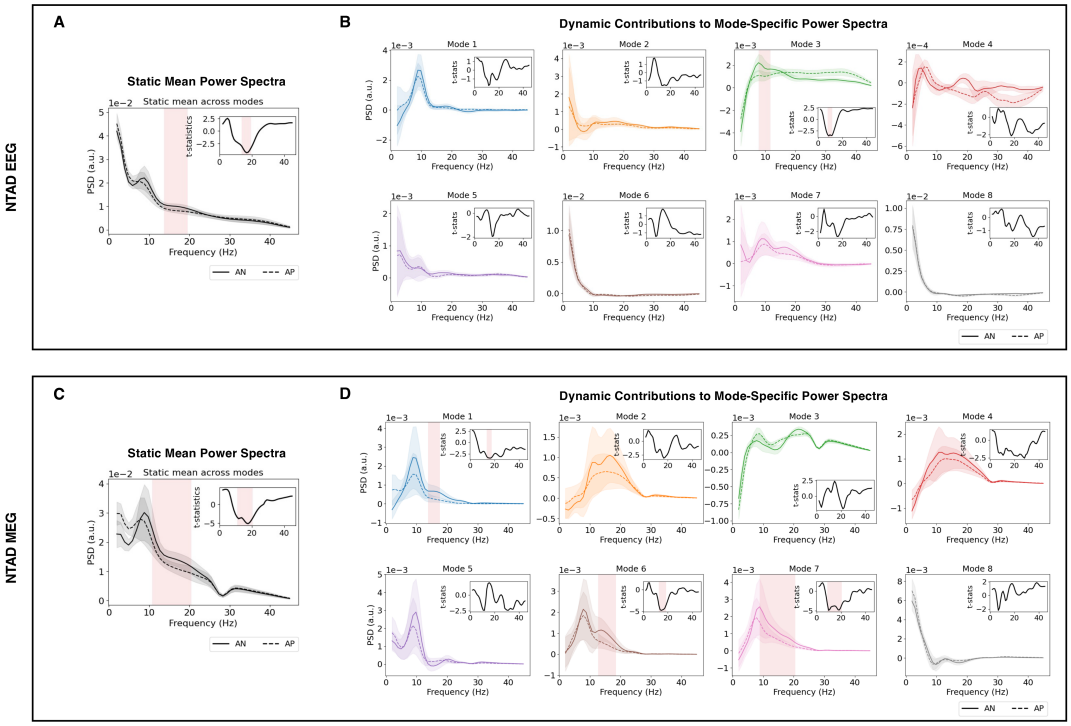

Figure B.9: Effects of MCI and early-stage AD are observed across multiple frequency bands when dynamic information is isolated. (A) The mean PSD across all modes is obtained from the EEG data for AN (solid) and AP (dotted) participants and averaged over the subjects and parcels. A cluster permutation test is conducted on the parcel-averaged static mean PSD to detect static effects of MCI and early-stage AD. Frequencies exhibiting statistical significance ($p < 0.05$; Bonferroni-corrected, n=9) are highlighted in red. **(B)** The mode-specific PSDs of the EEG data are averaged across each group and parcels after the mean across modes is subtracted at the subject level. These group-averaged, mean-subtracted PSDs of AN (solid) and AP (dotted) participants are illustrated for each DyNeMo mode. Cluster permutation tests are conducted on parcel-averaged, mean-subtracted PSDs of each mode to detect dynamic effects of MCI and early-stage AD. Frequencies exhibiting statistical significance ($p < 0.05$; Bonferroni-corrected, n=9) are highlighted in red. **(C)** The same analysis as in (A) is performed on the MEG data. **(D)** The same analysis as in (B) is performed on the MEG data. For all plots, the inset portrays t-statistics contrasting its corresponding PSDs of the AN and AP group.

B.3.4 Effects of MCI & Early-stage AD in State/Mode-Specific Power and FC

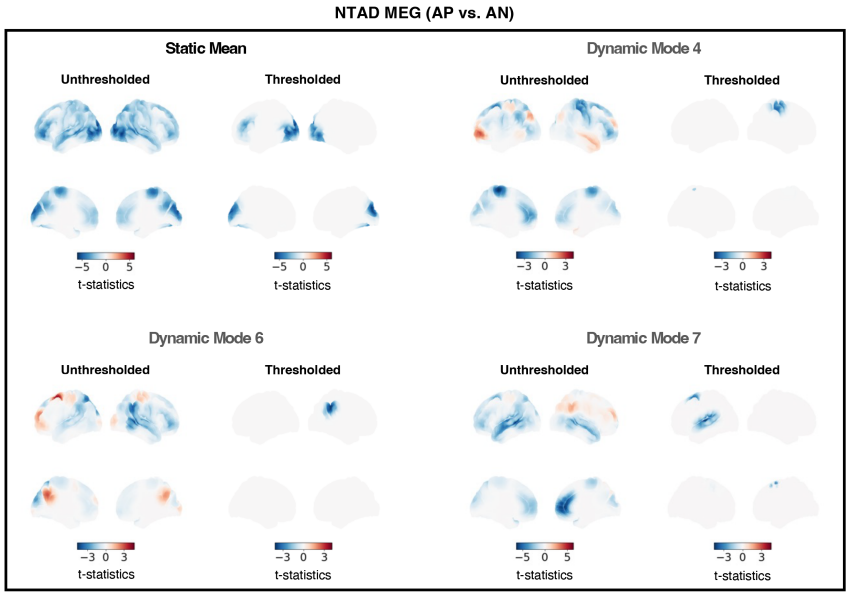

Figure B.10: Dynamic DyNeMo MEG modes reveal reduced wide-band power across multiple cortical regions for AP subjects. The result of statistical analysis conducted on the wide-band (1-45 Hz) static mean and dynamic mode-specific power maps is presented here. Only the power maps with significant effects of MCI and early-stage AD are plotted. Power maps on the left display t-statistics between groups, and the parcels with significant t-values are colored on the right. Max-t permutation tests were used to evaluate statistical significance. Parcels are marked significant if $p < 0.05$ (Bonferroni-corrected, n=9).

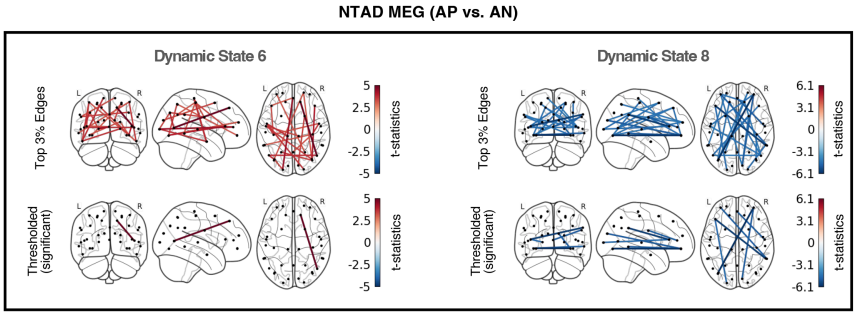

Figure B.11: Dynamic effects of MCI & early-stage AD are observed in HMM MEG wide-band FC maps. The result of max-t permutation tests conducted on FC maps is presented here, once the static mean FC across all states was separated from the wide-band (1-45 Hz) dynamic state-specific FC maps. The static mean or dynamic state-specific FC maps are plotted only if one or more significant connections were present. On the top, t-statistics of the FC maps between the AP and AN group (above the 97-th percentile) are portrayed. Connection edges with significant t-values ($p < 0.05$; Bonferroni-corrected, n=9) are displayed on the bottom.

In addition to state- and mode-specific power maps, we examined dynamic effects of MCI and early-stage AD on functional connectivity. Group-level max-t permutation tests on FC maps showed effects in MEG HMM States 6 and 8, wherein increased fronto-temporal connectivity and decreased fronto-occipital connectivity were reported, respectively (Fig. B.11). However, no significant group differences were found in DyNeMo mode-specific FC maps for both MEG and EEG.

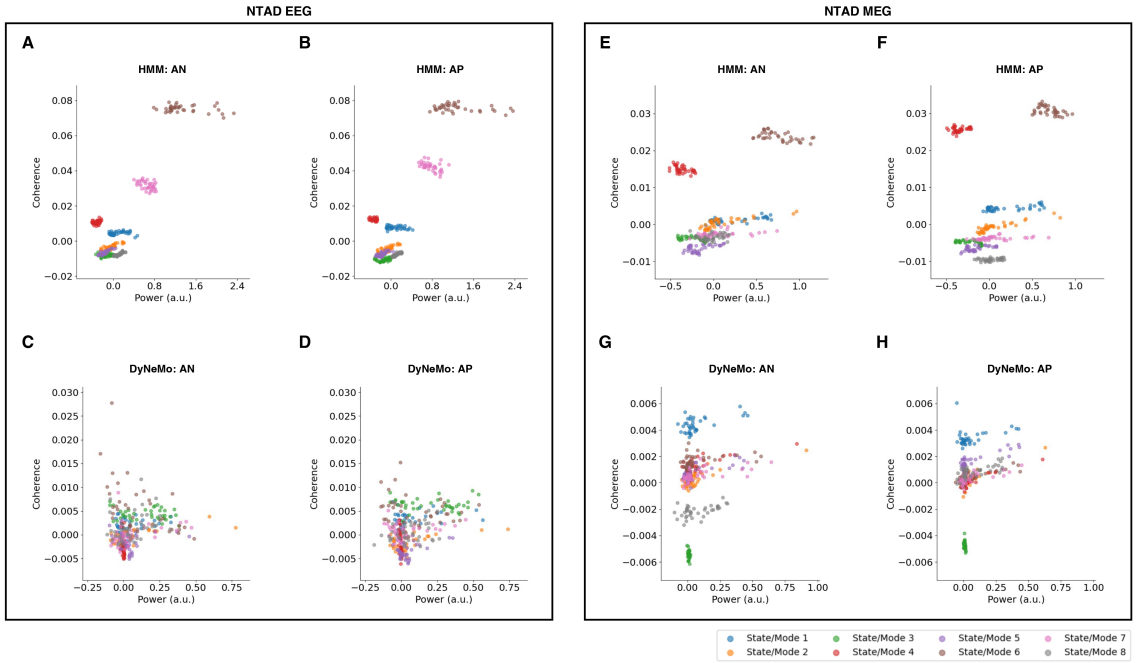

Figure B.12: Distributions of dynamic power and coherence in source-space EEG and MEG. Distributions of power and coherence values, computed from the HMM multi-taper spectra, are plotted for **(A)** AN and **(B)** AP participants relative to their state/mode-wise means. The same analysis is conducted using DyNeMo GLM PSDs for **(C)** AN and **(D)** AP subjects. **(E)-(H)** The identical analysis is repeated on the MEG dataset. Each color represents a state or mode, and each scatter point denotes a specific parcellated region. With DyNeMo, power values were rescaled with the maximum alpha mixing coefficient value of each mode at the subject level for better visualization.

References

1. Carvalho, A. F. *et al.* Evidence-based umbrella review of 162 peripheral biomarkers for major mental disorders. *Translational Psychiatry* **10,** 11. https://doi.org/10.1038%2Fs41398-020-0835-5 (2020).
2. Brückl, T. M. *et al.* The biological classification of mental disorders (BeCOME) study: a protocol for an observational deep-phenotyping study for the identification of biological subtypes. *BMC Psychiatry* **20,** 213. https://doi.org/10.1186%2Fs12888-020-02541-z (2020).
3. Huys, Q. J. M., Maia, T. V. & Frank, M. J. Computational psychiatry as a bridge from neuroscience to clinical applications. *Nature Neuroscience* **19,** 404–413. https://doi.org/10.1038%2Fnn.4238 (2016).
4. Walter, H. The third wave of biological psychiatry. *Frontiers in Psychology* **4,** 582. https://doi.org/10.3389%2Ffpsyg.2013.00582 (2013).
5. Ewen, J. B., Potter, W. Z. & Sweeney, J. A. Biomarkers and neurobehavioral diagnosis. *Biomarkers in Neuropsychiatry* **4,** 100029. https://doi.org/10.1016%2Fj.bionps.2020.100029 (2021).
6. Kapur, S., Phillips, A. G. & Insel, T. R. Why has it taken so long for biological psychiatry to develop clinical tests and what to do about it? *Molecular Psychiatry* **17,** 1174–1179. https://doi.org/10.1038%2Fmp.2012.105 (2012).
7. American Psychiatric Association. *Diagnostic and Statistical Manual of Mental Disorders* https://doi.org/10.1176%2Fappi.books.9780890425596 (American Psychiatric Association, 2013).
8. Bennett, D., Silverstein, S. M. & Niv, Y. The Two Cultures of Computational Psychiatry. *JAMA Psychiatry* **76,** 563. https://doi.org/10.1001%2Fjamapsychiatry.2019.0231 (2019).
9. Fernandes, B. S. *et al.* The new field of 'precision psychiatry'. *BMC Medicine* **15,** 80. https://doi.org/10.1186%2Fs12916-017-0849-x (2017).
10. Zhang, W., Sweeney, J. A., Bishop, J. R., Gong, Q. & Lui, S. Biological subtyping of psychiatric syndromes as a pathway for advances in drug discovery and personalized medicine. *Nature Mental Health* **1,** 88–99. https://doi.org/10.1038%2Fs44220-023-00019-x (2023).
11. Bryant, R. A., Galatzer-Levy, I. & Hadzi-Pavlovic, D. The Heterogeneity of Posttraumatic Stress Disorder in DSM-5. *JAMA Psychiatry* **80,** 189. https://doi.org/10.1001%2Fjamapsychiatry.2022.4092 (2023).
12. Galatzer-Levy, I. R. & Bryant, R. A. 636,120 Ways to Have Posttraumatic Stress Disorder. *Perspectives on Psychological Science* **8,** 651–662. https://doi.org/10.1177%2F1745691613504115 (2013).

13. Devi, G. & Scheltens, P. Heterogeneity of Alzheimer's disease: consequence for drug trials? *Alzheimer's Research & Therapy* **10,** 122. https://doi.org/10.1186%2Fs13195-018-0455-y (2018).

14. Avelar-Pereira, B., Belloy, M. E., O'Hara, R., Hosseini, S. M. H. & Alzheimer's Disease Neuroimaging Initiative. Decoding the heterogeneity of Alzheimer's disease diagnosis and progression using multilayer networks. *Molecular Psychiatry.* https://doi.org/10.1038%2Fs41380-022-01886-z (2022).

15. Browning, M., Paulus, M. & Huys, Q. J. What is Computational Psychiatry Good For? *Biological Psychiatry* **93,** 658–660. https://doi.org/10.1016%2Fj.biopsych.2022.08.030 (2023).

16. Long, J. M. & Holtzman, D. M. Alzheimer Disease: An Update on Pathobiology and Treatment Strategies. *Cell* **179,** 312–339. https://doi.org/10.1016%2Fj.cell.2019.09.001 (2019).

17. Knopman, D. S. *et al.* Alzheimer disease. *Nature Reviews Disease Primers* **7,** 33. https://doi.org/10.1038%2Fs41572-021-00269-y (2021).

18. Hansson, O. Biomarkers for neurodegenerative diseases. *Nature Medicine* **27,** 954–963. https://doi.org/10.1038%2Fs41591-021-01382-x (2021).

19. Teunissen, C. E. *et al.* Blood-based biomarkers for Alzheimer's disease: towards clinical implementation. *The Lancet Neurology* **21,** 66–77. https://www.sciencedirect.com/science/article/pii/S1474442221003616 (2022).

20. Lanskey, J. H. *et al.* New Therapeutics in Alzheimer's Disease Longitudinal Cohort study (NTAD): study protocol. *BMJ Open* **12,** e055135. https://doi.org/10.1136%2Fbmjopen-2021-055135 (2022).

21. Wakeman, D. G. & Henson, R. N. A multi-subject, multi-modal human neuroimaging dataset. *Scientific Data* **2,** 150001. https://doi.org/10.1038%2Fsdata.2015.1 (2015).

22. Murakami, S. & Okada, Y. Contributions of principal neocortical neurons to magnetoencephalography and electroencephalography signals. *The Journal of Physiology* **575,** 925–936. https://doi.org/10.1113%2Fjphysiol.2006.105379 (2006).

23. Hillebrand, A. & Barnes, G. A Quantitative Assessment of the Sensitivity of Whole-Head MEG to Activity in the Adult Human Cortex. *NeuroImage* **16,** 638–650. https://doi.org/10.1006%2Fnimg.2002.1102 (2002).

24. Baillet, S. Magnetoencephalography for brain electrophysiology and imaging. *Nature Neuroscience* **20,** 327–339. https://doi.org/10.1038%2Fnn.4504 (2017).

25. Ahlfors, S. P. in *Magnetoencephalography: From Signals to Dynamic Cortical Networks* (eds Supek, S. & Aine, C. J.) 259–278 (Springer International Publishing, Cham, 2019). https://doi.org/10.1007%2F978-3-030-00087-5_7.

26. Lopes da Silva, F. EEG and MEG: Relevance to Neuroscience. *Neuron* **80,** 1112–1128. https://doi.org/10.1016%2Fj.neuron.2013.10.017 (2013).

27. Cichy, R. M. & Pantazis, D. Multivariate pattern analysis of MEG and EEG: A comparison of representational structure in time and space. *NeuroImage* **158,** 441–454. https://doi.org/10.1016%2Fj.neuroimage.2017.07.023 (2017).

28. Reichert, C., Dürschmid, S., Heinze, H.-J. & Hinrichs, H. A Comparative Study on the Detection of Covert Attention in Event-Related EEG and MEG Signals to Control a BCI. *Frontiers in Neuroscience* **11,** 575. https://doi.org/10.3389%2Ffnins.2017.00575 (2017).

29. Mahmutoglu, M. A., Rupp, A. & Baumgärtner, U. Simultaneous EEG/MEG yields complementary information of nociceptive evoked responses. *Clinical Neurophysiology* **143,** 21–35. https://doi.org/10.1016%2Fj.clinph.2022.08.005 (2022).

30. Muthuraman, M. *et al.* Beamformer Source Analysis and Connectivity on Concurrent EEG and MEG Data during Voluntary Movements. *PLoS ONE* **9,** e91441. https://doi.org/10.1371%2Fjournal.pone.0091441 (2014).

31. Aydin, Ü. *et al.* Combined EEG/MEG Can Outperform Single Modality EEG or MEG Source Reconstruction in Presurgical Epilepsy Diagnosis. *PLOS ONE* **10,** e0118753. https://doi.org/10.1371%2Fjournal.pone.0118753 (2015).

32. McFadyen, J. & Dolan, R. J. Spatiotemporal Precision of Neuroimaging in Psychiatry. *Biological Psychiatry* **93,** 671–680. https://doi.org/10.1016%2Fj.biopsych.2022.08.016 (2023).

33. Biswal, B., Yetkin, F. Z., Haughton, V. M. & Hyde, J. S. Functional connectivity in the motor cortex of resting human brain using echo-planar mri. *Magnetic Resonance in Medicine* **34,** 537–541. https://doi.org/10.1002%2Fmrm.1910340409 (1995).

34. Shulman, G. L. *et al.* Common Blood Flow Changes across Visual Tasks: II. Decreases in Cerebral Cortex. *Journal of Cognitive Neuroscience* **9,** 648–663. https://doi.org/10.1162%2Fjocn.1997.9.5.648 (1997).

35. Raichle, M. E. *et al.* A default mode of brain function. *Proceedings of the National Academy of Sciences* **98,** 676–682. https://doi.org/10.1073%2Fpnas.98.2.676 (2001).

36. Buckner, R. L., Andrews-Hanna, J. R. & Schacter, D. L. The Brain's Default Network. *Annals of the New York Academy of Sciences* **1124,** 1–38. https://dx.doi.org/10.1196/annals.1440.011 (2008).

37. Raichle, M. E. The Brain's Default Mode Network. *Annual Review of Neuroscience* **38,** 433–477. https://doi.org/10.1146/annurev-neuro-071013-014030 (2015).

38. Beckmann, C. F., DeLuca, M., Devlin, J. T. & Smith, S. M. Investigations into resting-state connectivity using independent component analysis. *Philosophical Transactions of the Royal Society B: Biological Sciences* **360,** 1001–1013. https://doi.org/10.1098%2Frstb.2005.1634 (2005).

39. Damoiseaux, J. S. *et al.* Consistent resting-state networks across healthy subjects. *Proceedings of the National Academy of Sciences* **103,** 13848–13853. https://doi.org/10.1073%2Fpnas.0601417103 (2006).

40. Smith, S. M. *et al.* Temporally-independent functional modes of spontaneous brain activity. *Proceedings of the National Academy of Sciences* **109,** 3131–3136. https://doi.org/10.1073%2Fpnas.1121329109 (2012).

41. Luca, M. D., Smith, S., Stefano, N. D., Federico, A. & Matthews, P. M. Blood oxygenation level dependent contrast resting state networks are relevant to functional activity in the neocortical sensorimotor system. *Experimental Brain Research* **167,** 587–594. https://doi.org/10.1007%2Fs00221-005-0059-1 (2005).

42. Chenji, S. *et al.* Investigating Default Mode and Sensorimotor Network Connectivity in Amyotrophic Lateral Sclerosis. *PLOS ONE* **11,** e0157443. https://doi.org/10.1371%2Fjournal.pone.0157443 (2016).

43. Fox, M. D., Corbetta, M., Snyder, A. Z., Vincent, J. L. & Raichle, M. E. Spontaneous neuronal activity distinguishes human dorsal and ventral attention systems. *Proceedings of the National Academy of Sciences* **103,** 10046–10051. https://doi.org/10.1073%2Fpnas.0604187103 (2006).

44. Seeley, W. W. *et al.* Dissociable Intrinsic Connectivity Networks for Salience Processing and Executive Control. *The Journal of Neuroscience* **27,** 2349–2356. https://doi.org/10.1523%2Fjneurosci.5587-06.2007 (2007).

45. Vincent, J. L. *et al.* Coherent Spontaneous Activity Identifies a Hippocampal-Parietal Memory Network. *Journal of Neurophysiology* **96,** 3517–3531. https://doi.org/10.1152%2Fjn.00048.2006 (2006).

46. Laird, A. R. *et al.* Behavioral Interpretations of Intrinsic Connectivity Networks. *Journal of Cognitive Neuroscience* **23,** 4022–4037. https://doi.org/10.1162%2Fjocn_a_00077 (2011).

47. Smith, S. M. *et al.* Correspondence of the brain's functional architecture during activation and rest. *Proceedings of the National Academy of Sciences* **106,** 13040–13045. https://www.pnas.org/doi/abs/10.1073/pnas.0905267106 (2009).

48. Greicius, M. D., Srivastava, G., Reiss, A. L. & Menon, V. Default-mode network activity distinguishes Alzheimer's disease from healthy aging: Evidence from functional MRI. *Proceedings of the National Academy of Sciences* **101,** 4637–4642. https://www.pnas.org/doi/abs/10.1073/pnas.0308627101 (2004).

49. Sitnikova, T. A., Hughes, J. W., Ahlfors, S. P., Woolrich, M. W. & Salat, D. H. Short timescale abnormalities in the states of spontaneous synchrony in the functional neural networks in Alzheimer's disease. *NeuroImage: Clinical* **20,** 128–152. https://www.sciencedirect.com/science/article/pii/S2213158218301748 (2018).

50. Javaheripour, N. *et al.* Altered resting-state functional connectome in major depressive disorder: a mega-analysis from the PsyMRI consortium. *Translational Psychiatry* **11,** 511. https://doi.org/10.1038%2Fs41398-021-01619-w (2021).

51. Leuchter, A. F., Cook, I. A., Hunter, A. M., Cai, C. & Horvath, S. Resting-State Quantitative Electroencephalography Reveals Increased Neurophysiologic Connectivity in Depression. *PLoS ONE* **7,** e32508. https://doi.org/10.1371%2Fjournal.pone.0032508 (2012).

52. Damaraju, E. *et al.* Dynamic functional connectivity analysis reveals transient states of dysconnectivity in schizophrenia. *NeuroImage: Clinical* **5,** 298–308. https://doi.org/10.1016%2Fj.nicl.2014.07.003 (2014).

53. Lottman, K. K. *et al.* Examining resting-state functional connectivity in first-episode schizophrenia with 7T fMRI and MEG. *NeuroImage: Clinical* **24,** 101959. https://doi.org/10.1016%2Fj.nicl.2019.101959 (2019).

54. Brookes, M. J. *et al.* Investigating the electrophysiological basis of resting state networks using magnetoencephalography. *Proceedings of the National Academy of Sciences* **108,** 16783–16788. https://doi.org/10.1073%2Fpnas.1112685108 (2011).

55. Mantini, D., Perrucci, M. G., Gratta, C. D., Romani, G. L. & Corbetta, M. Electrophysiological signatures of resting state networks in the human brain. *Proceedings of the National Academy of Sciences* **104,** 13170–13175. https://doi.org/10.1073%2Fpnas.0700668104 (2007).

56. De Pasquale, F. *et al.* Temporal dynamics of spontaneous MEG activity in brain networks. *Proceedings of the National Academy of Sciences* **107,** 6040–6045. https://doi.org/10.1073%2Fpnas.0913863107 (2010).

57. Baker, A. P. *et al.* Fast transient networks in spontaneous human brain activity. *eLife* **3,** e01867. https://doi.org/10.7554%2Felife.01867 (2014).

58. Gohil, C. *et al.* Mixtures of large-scale dynamic functional brain network modes. *NeuroImage* **263,** 119595. https://doi.org/10.1016%2Fj.neuroimage.2022.119595 (2022).

59. Quinn, A. J. *et al.* Unpacking Transient Event Dynamics in Electrophysiological Power Spectra. *Brain Topography* **32,** 1020–1034. https://doi.org/10.1007%2Fs10548-019-00745-5 (2019).

60. Vidaurre, D. *et al.* Spontaneous cortical activity transiently organises into frequency specific phase-coupling networks. *Nature Communications* **9,** 2987. https://doi.org/10.1038%2Fs41467-018-05316-z (2018).

61. Van Ede, F., Quinn, A. J., Woolrich, M. W. & Nobre, A. C. Neural Oscillations: Sustained Rhythms or Transient Burst-Events? *Trends in Neurosciences* **41,** 415–417. https://doi.org/10.1016%2Fj.tins.2018.04.004 (2018).

62. Tal, I., Neymotin, S., Bickel, S., Lakatos, P. & Schroeder, C. E. Oscillatory Bursting as a Mechanism for Temporal Coupling and Information Coding. *Frontiers in Computational Neuroscience* **14,** 82. https://doi.org/10.3389%2Ffncom.2020.00082 (2020).

63. Cho, S. & Choi, J. H. A guide towards optimal detection of transient oscillatory bursts with unknown parameters. *Journal of Neural Engineering* **20,** 046007. https://doi.org/10.1088%2F1741-2552%2Facdffd (2023).

64. Jones, S. R. When brain rhythms aren't 'rhythmic': implication for their mechanisms and meaning. *Current Opinion in Neurobiology* **40,** 72–80. https://www.sciencedirect.com/science/article/pii/S0959438816300769 (2016).

65. Donoghue, T., Schaworonkow, N. & Voytek, B. Methodological considerations for studying neural oscillations. *European Journal of Neuroscience* **55,** 3502–3527. https://doi.org/10.1111%2Fejn.15361 (2021).

66. Zich, C., Quinn, A. J., Mardell, L. C., Ward, N. S. & Bestmann, S. Dissecting Transient Burst Events. *Trends in Cognitive Sciences* **24,** 784–788. https://doi.org/10.1016%2Fj.tics.2020.07.004 (2020).

67. Higgins, C. *et al.* Replay bursts in humans coincide with activation of the default mode and parietal alpha networks. *Neuron* **109,** 882–893. https://doi.org/10.1016%2Fj.neuron.2020.12.007 (2021).

68. Nour, M. M., Liu, Y., Higgins, C., Woolrich, M. W. & Dolan, R. J. Reduced coupling between offline neural replay events and default mode network activation in schizophrenia. *Brain Communications* **5,** fcad056. https://doi.org/10.1093%2Fbraincomms%2Ffcad056 (2023).

69. Tinkhauser, G. *et al.* Beta burst dynamics in Parkinson's disease OFF and ON dopaminergic medication. *Brain* **140,** 2968–2981. https://doi.org/10.1093%2Fbrain%2Fawx252 (2017).

70. Sporn, S., Hein, T. & Ruiz, M. H. Alterations in the amplitude and burst rate of beta oscillations impair reward-dependent motor learning in anxiety. *eLife* **9,** e50654. https://doi.org/10.7554%2Felife.50654 (2020).

71. Shin, H., Law, R., Tsutsui, S., Moore, C. I. & Jones, S. R. The rate of transient beta frequency events predicts behavior across tasks and species. *eLife* **6,** e29086. https://doi.org/10.7554%2Felife.29086 (2017).

72. Lundqvist, M. *et al.* Gamma and Beta Bursts Underlie Working Memory. *Neuron* **90,** 152–164. https://doi.org/10.1016%2Fj.neuron.2016.02.028 (2016).

73. Wendling, F., Ansari-Asl, K., Bartolomei, F. & Senhadji, L. From EEG signals to brain connectivity: A model-based evaluation of interdependence measures. *Journal of Neuroscience Methods* **183,** 9–18. https://doi.org/10.1016%2Fj.jneumeth.2009.04.021 (2009).

74. de Pasquale, F. *et al.* A Cortical Core for Dynamic Integration of Functional Networks in the Resting Human Brain. *Neuron* **74,** 753–764. https://doi.org/10.1016%2Fj.neuron.2012.03.031 (2012).

75. Allen, E. A. *et al.* Tracking Whole-Brain Connectivity Dynamics in the Resting State. *Cerebral Cortex* **24,** 663–676. https://doi.org/10.1093%2Fcercor%2Fbhs352 (2012).

76. O'Neill, G. C. *et al.* Measurement of dynamic task related functional networks using MEG. *NeuroImage* **146,** 667–678. https://doi.org/10.1016%2Fj.neuroimage.2016.08.061 (2017).

77. Quinn, A. J. *et al.* Task-Evoked Dynamic Network Analysis Through Hidden Markov Modeling. *Frontiers in Neuroscience* **12,** 603. https://doi.org/10.3389%2Ffnins.2018.00603 (2018).

78. Vidaurre, D. *et al.* Spectrally resolved fast transient brain states in electrophysiological data. *NeuroImage* **126,** 81–95. https://doi.org/10.1016%2Fj.neuroimage.2015.11.047 (2016).

79. Liuzzi, L. *et al.* How Sensitive Are Conventional MEG Functional Connectivity Metrics With Sliding Windows to Detect Genuine Fluctuations in Dynamic Functional Connectivity? *Frontiers in Neuroscience* **13,** 797. https://doi.org/10.3389%2Ffnins.2019.00797 (2019).

80. Bishop, C. M. *Pattern Recognition and Machine Learning* (Springer, 2006).

81. Rezek, I. & Roberts, S. in *Advanced Information and Knowledge Processing* (eds Husmeier, D., Dybowski, R. & Roberts, S.) 419–450 (Springer-Verlag, 2005). https://doi.org/10.1007%2F1-84628-119-9_14.

82. Vidaurre, D. *et al.* Discovering dynamic brain networks from big data in rest and task. *NeuroImage* **180,** 646–656. https://doi.org/10.1016%2Fj.neuroimage.2017.06.077 (2018).

83. Pervaiz, U., Vidaurre, D., Gohil, C., Smith, S. M. & Woolrich, M. W. Multi-dynamic modelling reveals strongly time-varying resting fMRI correlations. *Medical Image Analysis* **77,** 102366. https://doi.org/10.1016%2Fj.media.2022.102366 (2022).

84. Hochreiter, S. & Schmidhuber, J. Long Short-Term Memory. *Neural Computation* **9,** 1735–1780. https://doi.org/10.1162%2Fneco.1997.9.8.1735 (1997).

85. Zhang, C., Butepage, J., Kjellstrom, H. & Mandt, S. Advances in Variational Inference. *IEEE Transactions on Pattern Analysis and Machine Intelligence* **41,** 2008–2026. https://doi.org/10.1109%2Ftpami.2018.2889774 (2019).

86. Scally, B., Burke, M. R., Bunce, D. & Delvenne, J.-F. Resting-state EEG power and connectivity are associated with alpha peak frequency slowing in healthy aging. *Neurobiology of Aging* **71,** 149–155. https://doi.org/10.1016%2Fj.neurobiolaging.2018.07.004 (2018).

87. Rossini, P. M., Rossi, S., Babiloni, C. & Polich, J. Clinical neurophysiology of aging brain: From normal aging to neurodegeneration. *Progress in Neurobiology* **83,** 375–400. https://doi.org/10.1016%2Fj.pneurobio.2007.07.010 (2007).

88. Perinelli, A., Assecondi, S., Tagliabue, C. F. & Mazza, V. Power shift and connectivity changes in healthy aging during resting-state EEG. *NeuroImage* **256,** 119247. https://doi.org/10.1016%2Fj.neuroimage.2022.119247 (2022).

89. Aoki, Y. *et al.* Cortical electrical activity changes in healthy aging using EEG-eLORETA analysis. *NeuroImage: Reports* **2,** 100143. https://doi.org/10.1016%2Fj.ynirp.2022.100143 (2022).

90. Babiloni, C. *et al.* Sources of cortical rhythms in adults during physiological aging: A multicentric EEG study. *Human Brain Mapping* **27,** 162–172. https://doi.org/10.1002%2Fhbm.20175 (2006).

91. Jauny, G., Eustache, F. & Hinault, T. Connectivity dynamics and cognitive variability during aging. *Neurobiology of Aging* **118,** 99–105. https://doi.org/10.1016%2Fj.neurobiolaging.2022.07.001 (2022).

92. Coquelet, N. *et al.* The electrophysiological connectome is maintained in healthy elders: a power envelope correlation MEG study. *Scientific Reports* **7,** 13984. https://doi.org/10.1038%2Fs41598-017-13829-8 (2017).

93. Destoky, F. *et al.* Comparing the potential of MEG and EEG to uncover brain tracking of speech temporal envelope. *NeuroImage* **184,** 201–213. https://doi.org/10.1016%2Fj.neuroimage.2018.09.006 (2019).

94. Illman, M. *et al.* Comparing MEG and EEG in detecting the 20-Hz rhythm modulation to tactile and proprioceptive stimulation. *NeuroImage* **215,** 116804. https://doi.org/10.1016%2Fj.neuroimage.2020.116804 (2020).

95. Babayan, A. *et al.* A mind-brain-body dataset of MRI, EEG, cognition, emotion, and peripheral physiology in young and old adults. *Scientific Data* **6,** 180308. https://doi.org/10.1038%2Fsdata.2018.308 (2019).

96. Shafto, M. A. *et al.* The Cambridge Centre for Ageing and Neuroscience (Cam-CAN) study protocol: a cross-sectional, lifespan, multidisciplinary examination of healthy cognitive ageing. *BMC Neurology* **14,** 204. https://doi.org/10.1186%2Fs12883-014-0204-1 (2014).

97. Quinn, A. J. *et al.* The GLM-Spectrum: A multilevel framework for spectrum analysis with covariate and confound modelling. *bioRxiv,* 2022.11.14.516449. https://doi.org/10.1101%2F2022.11.14.516449 (2022).

98. Quinn, A. J., van Es, M. W., Gohil, C. & Woolrich, M. W. OHBA Software Library in Python (OSL) (0.1.1). *Zenodo.* https://doi.org/10.5281/zenodo.6875059 (2023).

99. Rosner, B. Percentage Points for a Generalized ESD Many-Outlier Procedure. *Technometrics* **25,** 165–172. https://doi.org/10.1080%2F00401706.1983.10487848 (1983).

100. Hyvarinen, A. Fast and robust fixed-point algorithms for independent component analysis. *IEEE Transactions on Neural Networks* **10,** 626–634. https://doi.org/10.1109%2F72.761722 (1999).

101. Perrin, F., Pernier, J., Bertrand, O. & Echallier, J. Spherical splines for scalp potential and current density mapping. *Electroencephalography and Clinical Neurophysiology* **72,** 184–187. https://doi.org/10.1016%2F0013-4694%2889%2990180-6 (1989).

102. Hallez, H. *et al.* Review on solving the forward problem in EEG source analysis. *Journal of NeuroEngineering and Rehabilitation* **4,** 46. https://doi.org/10.1186%2F1743-0003-4-46 (2007).

103. Grech, R. *et al.* Review on solving the inverse problem in EEG source analysis. *Journal of NeuroEngineering and Rehabilitation* **5,** 25. https://doi.org/10.1186%2F1743-0003-5-25 (2008).

104. Jenkinson, M., Pechaud, M. & Smith, S. *BET2: MR-based estimation of brain, skull and scalp surfaces* in *Eleventh annual meeting of the organization for human brain mapping* **17** (2005), 167.

105. Veen, B. V. & Buckley, K. Beamforming: a versatile approach to spatial filtering. *IEEE ASSP Magazine* **5,** 4–24. https://doi.org/10.1109%2F53.665 (1988).

106. Colclough, G., Brookes, M., Smith, S. & Woolrich, M. A symmetric multivariate leakage correction for MEG connectomes. *NeuroImage* **117,** 439–448. https://doi.org/10.1016%2Fj.neuroimage.2015.03.071 (2015).

107. Kingma, D. P. & Ba, J. Adam: A method for stochastic optimization. *arXiv,* 1412.6980. https://doi.org/10.48550/arXiv.1412.6980 (2014).

108. Crouse, D. On implementing 2D rectangular assignment algorithms. *IEEE Transactions on Aerospace and Electronic Systems* **52,** 1679–1696. https://doi.org/10.1109/TAES.2016.140952 (2016).

109. Gohil, C. *et al.* osl-dynamics: A toolbox for modelling fast dynamic brain activity. *bioRxiv,* 2023.08.07.549346. https://doi.org/10.1101%2F2023.08.07.549346 (2023).

110. Bijsterbosch, J. *et al.* Challenges and future directions for representations of functional brain organization. *Nature Neuroscience* **23,** 1484–1495. https://doi.org/10.1038%2Fs41593-020-00726-z (2020).

111. Colclough, G. *et al.* How reliable are MEG resting-state connectivity metrics? *NeuroImage* **138,** 284–293. https://doi.org/10.1016%2Fj.neuroimage.2016.05.070 (2016).

112. Holmes, A. P., Blair, R. C., Watson, J. D. G. & Ford, I. Nonparametric Analysis of Statistic Images from Functional Mapping Experiments. *Journal of Cerebral Blood Flow & Metabolism* **16,** 7–22. https://doi.org/10.1097%2F00004647-199601000-00002 (1996).

113. Nichols, T. E. & Holmes, A. P. Nonparametric permutation tests for functional neuroimaging: A primer with examples. *Human Brain Mapping* **15,** 1–25. https://doi.org/10.1002%2Fhbm.1058 (2001).

114. Maris, E. & Oostenveld, R. Nonparametric statistical testing of EEG- and MEG-data. *Journal of Neuroscience Methods* **164,** 177–190. https://doi.org/10.1016%2Fj.jneumeth.2007.03.024 (2007).

115. Sassenhagen, J. & Draschkow, D. Cluster-based permutation tests of MEG/EEG data do not establish significance of effect latency or location. *Psychophysiology* **56,** e13335. https://doi.org/10.1111%2Fpsyp.13335 (2019).

116. Brett, M., Penny, W. & Kiebel, S. in *Human Brain Function (Second Edition)* (eds Frackowiak, R. S. *et al.*) 867–879 (Academic Press, Burlington, 2004). https://doi.org/10.1016/B978-012264841-0/50046-9.

117. Hughes, L. E. *et al.* Biomagnetic biomarkers for dementia: A pilot multicentre study with a recommended methodological framework for magnetoencephalography. *Alzheimer's & Dementia: Diagnosis, Assessment & Disease Monitoring* **11,** 450–462. https://doi.org/10.1016%2Fj.dadm.2019.04.009 (2019).

118. Briels, C. T. *et al.* Reproducibility of EEG functional connectivity in Alzheimer's disease. *Alzheimer's Research & Therapy* **12,** 68. https://doi.org/10.1186%2Fs13195-020-00632-3 (2020).

119. Aoki, Y. *et al.* EEG resting-state networks in Alzheimer's disease associated with clinical symptoms. *Scientific Reports* **13,** 3964. https://doi.org/10.1038%2Fs41598-023-30075-3 (2023).

120. Ikeda, Y. *et al.* Spontaneous MEG activity of the cerebral cortex during eyes closed and open discriminates Alzheimer's disease from cognitively normal older adults. *Scientific Reports* **10,** 9132. https://doi.org/10.1038%2Fs41598-020-66034-5 (2020).

121. Musaeus, C. S. *et al.* EEG Theta Power Is an Early Marker of Cognitive Decline in Dementia due to Alzheimer's Disease. *Journal of Alzheimer's Disease* **64,** 1359–1371. https://doi.org/10.3233%2Fjad-180300 (2018).

122. Koelewijn, L. *et al.* Alzheimer's disease disrupts alpha and beta-band resting-state oscillatory network connectivity. *Clinical Neurophysiology* **128,** 2347–2357. https://www.sciencedirect.com/science/article/pii/S1388245717301645 (2017).

123. Puttaert, D. *et al.* Alterations in resting-state network dynamics along the Alzheimer's disease continuum. *Scientific Reports* **10,** 21990. https://doi.org/10.1038%2Fs41598-020-76201-3 (2020).

124. Sorg, C. *et al.* Selective changes of resting-state networks in individuals at risk for Alzheimer's disease. *Proceedings of the National Academy of Sciences* **104,** 18760–18765. https://www.pnas.org/doi/abs/10.1073/pnas.0708803104 (2007).

125. Ibrahim, B. *et al.* Diagnostic power of resting-state fMRI for detection of network connectivity in Alzheimer's disease and mild cognitive impairment: A systematic review. *Human Brain Mapping* **42,** 2941–2968. https://onlinelibrary.wiley.com/doi/abs/10.1002/hbm.25369 (2021).

126. Schoonhoven, D. N. *et al.* Sensitive and reproducible MEG resting-state metrics of functional connectivity in Alzheimer's disease. *Alzheimer's Research & Therapy* **14,** 38. https://doi.org/10.1186%2Fs13195-022-00970-4 (2022).

127. Xu, X., Yuan, H. & Lei, X. Activation and Connectivity within the Default Mode Network Contribute Independently to Future-Oriented Thought. *Scientific Reports* **6,** 21001. https://doi.org/10.1038%2Fsrep21001 (2016).